

# 1 Piccolino regulates the architecture of the 2 ribbon at cochlear inner hair cell synapses 3

4 Susann Michanski<sup>1,2,3,4\*</sup>, Rohan Kapoor<sup>5,6,7\*</sup>, Anna M. Steyer<sup>8</sup>, Wiebke Möbius<sup>8</sup>, Iris Frühholz<sup>9</sup>, Frauke  
5 Ackermann<sup>10</sup>, Mehmet Gültas<sup>11</sup>, Craig C. Garner<sup>10,12</sup>, F. Kent Hamra<sup>13</sup>, Jakob Neef<sup>3,5,6</sup>, Nicola Strenzke<sup>3,14</sup>,  
6 Tobias Moser<sup>3,4,5,6#</sup>, Carolin Wichmann<sup>1,2,3#</sup>

7 1. Molecular Architecture of Synapses Group, Institute for Auditory Neuroscience and InnerEarLab, University Medical  
8 Center Göttingen, Göttingen, Germany

9 2. Center for Biostructural Imaging of Neurodegeneration, University Medical Center Göttingen, Göttingen, Germany

10 3. Collaborative Research Center 889 “Cellular Mechanisms of Sensory Processing”, 37099 Göttingen, Germany

11 4. Multiscale Bioimaging of Excitable Cells, Cluster of Excellence, 37075 Göttingen, Germany

12 5. Institute for Auditory Neuroscience and InnerEarLab, University Medical Center Göttingen, 37075 Göttingen,  
13 Germany

14 6. Auditory Neuroscience & Synaptic Nanophysiology Group, Max Planck Institute for Multidisciplinary Sciences, City  
15 Campus, 37077 Göttingen, Germany

16 7. IMPRS Molecular Biology, Göttingen Graduate School for Neuroscience and Molecular Biosciences, University of  
17 Göttingen, Göttingen, Germany

18 8. Electron Microscopy Core Unit, Department of Neurogenetics, Max Planck Institute for Multidisciplinary Sciences,  
19 City Campus, 37075 Göttingen, Germany

20 9. Developmental, Neural, and Behavioral Biology Master program, University of Göttingen, Germany

21 10. German Center for Neurodegenerative Diseases, Berlin 10117, Germany

22 11. Faculty of Agriculture, South Westphalia University of Applied Sciences, 59494 Soest, Germany

23 12. NeuroCureCluster of Excellence, Charité – Universitätsmedizin, Berlin 10117, Germany

24 13. Department of Obstetrics and Gynecology, University of Texas Southwestern, Dallas, Texas 75390-9041

25 14. Auditory Systems Physiology Group, Institute for Auditory Neuroscience and InnerEarLab, University Medical  
26 Center Göttingen, Göttingen, Germany

27 \* Equal contribution

28 # shared correspondence  
29  
30  
31

32 **Character count: 78.253 without space**

## 33 Abstract

34 Cochlear inner hair cells (IHCs) form specialized ribbon synapses with spiral ganglion neurons that  
35 tirelessly transmit sound information at high rates over long time periods with extreme temporal  
36 precision. This functional specialization is essential for precise sound encoding and is attributed to a  
37 distinct molecular machinery with unique players or splice variants compared to conventional neuronal  
38 synapses. Among these is the active zone (AZ) scaffold protein piccolo/aczonin, which is represented by  
39 its short splice variant piccolino at cochlear and retinal ribbon synapses. While the function of piccolo at  
40 synapses of the central nervous system has been intensively investigated, the role of piccolino at IHC  
41 synapses remains unclear. In this study, we characterized the structure and function of IHC-synapses in  
42 piccolo gene-trap mutant rats (*Pclo<sup>gt/gt</sup>*). We found a mild hearing deficit with elevated thresholds and  
43 reduced amplitudes of auditory brainstem responses. Ca<sup>2+</sup> channel distribution and ribbon morphology  
44 were altered in apical IHCs, while their presynaptic function seemed unchanged. We conclude that  
45 piccolino contributes to the AZ organization in IHCs and is essential for normal synaptic transmission.

## 46 Keywords

47 Active zone/Ca<sup>2+</sup> channel/cochlea/ hearing /synaptic vesicle

48

## 49 Introduction

50 Ribbon synapses are involved in vertebrate vision, hearing and balance. They are specialized in terms of  
51 function, morphology and molecular composition to enable indefatigable neurotransmission over long  
52 time periods. Depending on the ribbon synapse type, the electron-dense appearing synaptic ribbon can  
53 tether up to several hundreds of synaptic vesicles (SVs) (Matthews and Fuchs, 2010; Moser et al., 2019;  
54 Wichmann and Moser, 2015). In addition to employing the ribbon-specific protein RIBEYE, that

55 constitutes the main component of the synaptic ribbon (Becker et al., 2018; Jean et al., 2018; Maxeiner  
56 et al., 2016; Schmitz et al., 2000), the molecular composition of ribbon-type AZs shows further  
57 differences from conventional neuronal synapses (Chakrabarti and Wichmann, 2019; Moser et al.,  
58 2019). For example, ribbon synapses employ different isoforms of presynaptic proteins such as rab3-  
59 interacting molecule 2 (RIM2) instead of RIM1 (Grabner et al., 2015; Jung et al., 2015a). Moreover, the  
60 presynaptic multi-domain protein piccolo/aczonin, is represented solely by its short splice variant  
61 piccolino as shown for photoreceptor (Regus-Leidig et al., 2013) and cochlear inner hair cell (IHC) ribbon  
62 synapses (Butola et al., 2017; Michanski et al., 2019; Regus-Leidig et al., 2013).

63 The function of piccolo at conventional synapses has been investigated intensely (Cases-Langhoff et al.,  
64 1996; Fenster et al., 2003; Gundelfinger et al., 2015; Leal-Ortiz et al., 2008; Mukherjee et al., 2010).  
65 Piccolo together with bassoon is involved in synapse assembly, SV clustering and maintaining synapse  
66 integrity (Gundelfinger et al., 2015). Piccolo seems especially important for the SV pool organization. At  
67 the calyx of Held, piccolo was found to organize the readily-releasable vesicle pool (RRP) (Parthier et al.,  
68 2018) and at the endbulb of Held, piccolo is required for normal SV replenishment (Butola et al., 2017).  
69 Furthermore, a reduction of SVs, specifically from the total recycling pool was found at hippocampal  
70 neurons lacking piccolo (Ackermann et al., 2019). In contrast, piccolino's role at ribbon synapses remains  
71 poorly understood. Importantly, in comparison to full-length piccolo, piccolino lacks a number of  
72 interaction sites for presynaptic binding partners such as CAST/Munc13 and RIM, L-type  $Ca^{2+}$  channels as  
73 well as the interaction site for its homologue bassoon (Regus-Leidig et al., 2013). Instead, piccolino was  
74 found to interact with the ribbon component RIBEYE (Müller et al., 2019), in line with its localization  
75 exclusively at the synaptic ribbon (Dick et al., 2001; Limbach et al., 2011; Michanski et al., 2019; Regus-  
76 Leidig et al., 2013). While at conventional synapses, the functions of piccolo and bassoon seem partially  
77 redundant (Altrock et al., 2003; Gundelfinger et al., 2015; Leal-Ortiz et al., 2008; Mukherjee et al., 2010;  
78 Waites et al., 2013), piccolino's function at ribbon synapses might be unique and could differ from

79 piccolo's function at conventional synapses. Piccolino's absence or reduction had a striking structural  
80 impact on photoreceptor ribbon synapses: the altered ribbon shape went along with a reduced number  
81 of SVs around the ribbons (Müller et al., 2019; Regus-Leidig et al., 2014). A previous study of the  
82 auditory system reported that piccolo KO mice lack functional deficits on the level of auditory brain-  
83 stem response (ABR) thresholds (Li et al., 2021).

84         Given the visual phenotype and the prominent piccolo expression in IHCs, we performed a  
85 comprehensive structural and functional study on piccolo gene trap mutant rats (*Pclo<sup>gt/gt</sup>*) (Ackermann et  
86 al., 2019; Medrano et al., 2020; Müller et al., 2019) by combining systems and cell physiology with  
87 confocal, stimulated emission depletion (STED) and electron microscopy. We observed an altered Ca<sup>2+</sup>  
88 channel distribution and 3D reconstructions from electron microscopic data uncovered changes in  
89 ribbon morphology for a subset of synapses, resulting in two morphologically distinguishable ribbon  
90 categories in *Pclo<sup>gt/gt</sup>* IHCs. Category 1 ribbons appeared completely normal, while category 2  
91 encompassed small, spherical ribbons that lacked SVs at their upper ribbon part. Recording ABRs, we  
92 discovered a mild hearing phenotype despite our findings of normal IHC Ca<sup>2+</sup> currents and exocytosis.  
93 Our data suggest that piccolo is involved in the proper formation of synaptic ribbons, likely via  
94 organizing RIBEYE, and potentially via the ribbon, normal clustering of Ca<sup>2+</sup> channels. We conclude that  
95 piccolo is essential for normal organization of ribbon type AZs and required for normal hearing.

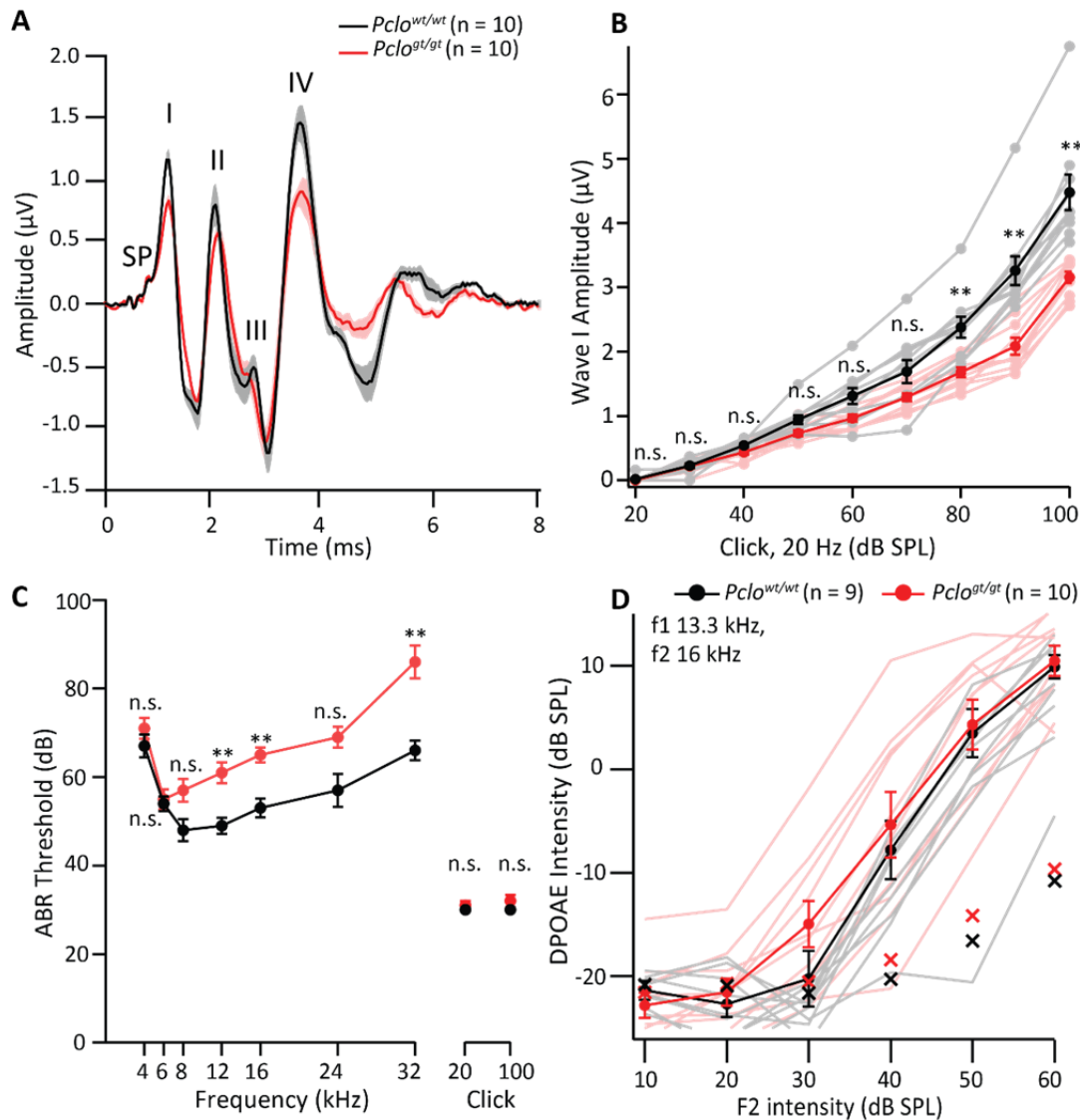
96

## 97 Results

### 98 Reduced ABR wave I amplitudes and elevated ABR thresholds in *Pclo<sup>gt/gt</sup>* rats

99 To investigate the role of piccolo in the auditory system, we commenced our study by recording ABRs  
100 in piccolo-deficient (*Pclo<sup>gt/gt</sup>*) rats at the age of two months. We found a significant amplitude  
101 reduction of ABR wave I, which represents the compound action potential of spiral ganglion neurons

102 (SGNs) to 73% of normal ( $1.68 \pm 0.08 \mu\text{V}$ ,  $N_{\text{animals}} = 10$  for  $Pclo^{gt/gt}$  rats versus  $2.38 \pm 0.16 \mu\text{V}$ ,  $N_{\text{animals}} = 10$   
103 for  $Pclo^{wt/wt}$  rats ( $P < 0.01$ , two-way repeated measures ANOVA with post-hoc Holm-Šidák correction for  
104 multiple comparisons) at 80 dB (peak equivalent, pe, 20 Hz clicks) (Fig 1A, B). The successive ABR waves  
105 were also slightly reduced in amplitude, but the difference was significant only for wave IV ( $P < 0.05$ , t-  
106 test, Fig 1A). ABR thresholds in response to tone bursts showed a mild but significant elevation for  
107 middle and high sound frequencies (approximately 10 - 20 dB;  $P_{12\text{kHz}}$ ,  $P_{16\text{kHz}}$  and  $P_{32\text{kHz}} < 0.01$ , two-way  
108 repeated measures ANOVA followed by Holm-Šidák multi-comparison test), but not for low frequency  
109 tones and broadband click stimuli (Fig 1C). We also measured cochlear amplification mediated by outer  
110 hair cells by recording the distortion product otoacoustic emissions (DPOAEs) which were unaltered (Fig  
111 1D). Overall, we report a mild but significant impairment in synchronous sound onset responses of SGNs  
112 despite intact cochlear amplification, which is consistent with a sound encoding deficit at the first  
113 auditory synapse upon genetic disruption of *piccolino*. This hearing phenotype appears more  
114 pronounced than that seen in *piccolo* mutant mice with maintained *piccolino* expression in IHCs (Butola  
115 et al., 2017) or that of RIBEYE KO mice (Becker et al., 2018; Jean et al., 2018).



116

117 **Figure 1. Reduced wave I amplitudes and elevated thresholds of auditory brainstem response. (A)**  
 118 Average ABR waveforms in response to 80 dB (pe) clicks (20 Hz) in 2 months old rats ( $N_{\text{animals}} = 10$  each  
 119 for  $Pclo^{wt/wt}$  and  $Pclo^{gt/gt}$ ). Lines represent averages, shaded area represents  $\pm$  SEM. SP: summing  
 120 potential (hair cell receptor potential), roman numerals (I – IV): ABR waves generated along the auditory  
 121 pathway. **(B)** ABR wave I amplitudes in response to 20 Hz clicks at different sound pressure levels show a  
 122 significant decrease in  $Pclo^{gt/gt}$  rats at 80dB and above, implying impaired synchronous sound evoked  
 123 firing of their SGNs, ( $P < 0.01$ , two-way repeated measures ANOVA followed by post hoc Holm-Šidák  
 124 multi-comparison correction). Dark lines represent averages, lighter ones represent individual traces. **(C)**  
 125  $Pclo^{gt/gt}$  rats show elevated ABR thresholds for middle and high frequency tone bursts, whereas  
 126 thresholds in response to low frequency tone bursts and click stimuli (applied at 20 and 100 Hz  
 127 stimulation rate) appear comparable;  $P_{12\text{kHz}}$ ,  $P_{16\text{kHz}}$ , and  $P_{32\text{kHz}} < 0.01$ , two-way repeated measures ANOVA  
 128 followed by Holm-Šidák multi-comparison correction. **(D)** DPOAE amplitude in response to pairs of  
 129 simultaneous sine waves ( $f_1 = 13.3$  kHz,  $f_2 = 16$  kHz) at increasing sound pressure levels (intensity of  $f_1$  is  
 130 10 dB above  $f_2$ ) appear comparable in  $Pclo^{wt/wt}$  ( $N_{\text{animals}} = 9$ ) and  $Pclo^{gt/gt}$  rats ( $N_{\text{animals}} = 10$ ), implying  
 131 unaltered cochlear amplification. Dark lines represent mean  $\pm$  SEM, lighter ones represent individual

132 traces, crosses represent noise floor. Asterisks indicate significance levels with \* $P < 0.05$ , \*\* $P < 0.01$ ,  
133 \*\*\* $P < 0.001$ .

134

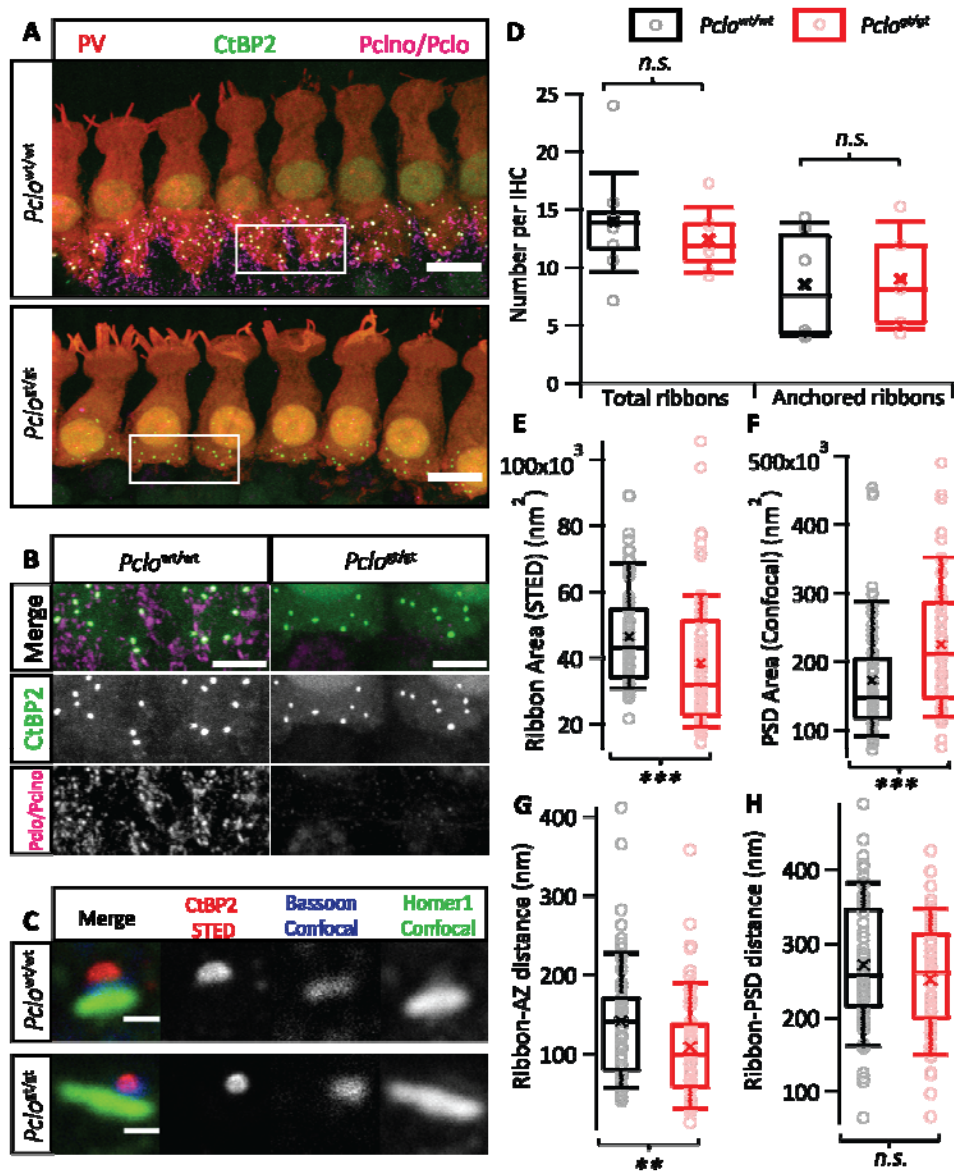
135 [Smaller ribbons but larger PSD areas at \*Pclo\*<sup>gt/gt</sup> active zones](#)

136

137 We next investigated ribbon synapse abundance and morphology by performing immunohistochemistry  
138 on whole-mounted apical portions of the organ of Corti acutely dissected from 2 months old *Pclo*<sup>wt/wt</sup>  
139 and *Pclo*<sup>gt/gt</sup> rats, followed by confocal and super resolution STED microscopy. We first used an antibody  
140 that recognizes a peptide corresponding to amino acid 2012 to 2351 of rat piccolo, designed to bind to  
141 full-length piccolo as well as the shorter splice variant piccolino. In *Pclo*<sup>wt/wt</sup> organs of Corti, we observed  
142 immunofluorescent puncta at every afferent synaptic contact, colocalizing with the synaptic ribbon  
143 (labeled with an antibody against CtBP2/RIBEYE), as well as at efferent synapses (immunofluorescent  
144 spots not colocalized with ribbons). *Pclo*<sup>gt/gt</sup> organs of Corti, on the other hand, showed complete  
145 absence of any piccolo/picolino-specific immunofluorescence (Fig 2A, B). Next, we performed triple-  
146 labeling using antibodies against CtBP2 (labeling the synaptic ribbon), bassoon (the presynaptic active  
147 zone (AZ)) and homer1 (the postsynaptic density). The localization of the synaptic markers seemed  
148 unaltered. We observed that the total number of synaptic ribbons (total count of CtBP2 spots) and the  
149 number of anchored ribbons (number of CtBP2 and bassoon juxtapositions) stays intact upon piccolino  
150 disruption (Fig 2D). CtBP2/piccolo co-labeled sections as shown in Fig 2B were included for estimation of  
151 total ribbon counts.

152 We then acquired images of *Pclo*<sup>wt/wt</sup> and *Pclo*<sup>gt/gt</sup> synapses using 2D-STED (CtBP2) and confocal  
153 (bassoon, homer1) imaging to assess their morphology (Fig 2C). Visually, a large proportion of synaptic  
154 ribbons from *Pclo*<sup>gt/gt</sup> rats appeared smaller and more compact, in contrast to the typical ellipsoid-  
155 shaped ribbons from *Pclo*<sup>wt/wt</sup> rats. A 2D-Gaussian function was fitted to raw images of randomly  
156 selected synapses to estimate the area of the ribbon and the PSD. We found that on average, the size of  
157 the synaptic ribbon appeared to be reduced for *Pclo*<sup>gt/gt</sup> rats ( $38.34 \times 10^3 \pm 2.36 \times 10^3 \text{ nm}^2$ , S.D. =  $19.71 \times 10^3$ ,

158  $n_{\text{ribbons}} = 71$ ,  $N_{\text{animals}} = 3$ ) compared to *Pclo*<sup>wt/wt</sup> ( $46.32 \times 10^3 \pm 1.77 \times 10^3$  nm<sup>2</sup>, S.D. =  $15.12 \times 10^3$ ,  $n_{\text{ribbons}} = 74$ ,  
 159  $N_{\text{animals}} = 3$ ;  $P < 0.001$ , Mann-Whitney-Wilcoxon Test, Fig 2E). Images with more than one ribbon per  
 160 synapse (observed only in *Pclo*<sup>wt/wt</sup> IHCs) were excluded from analysis to avoid overestimation of ribbon  
 161 size in *Pclo*<sup>wt/wt</sup> IHCs. On the other hand, the PSD size appeared to be larger for *Pclo*<sup>gt/gt</sup> rats ( $22.46 \times 10^4 \pm$   
 162  $1.20 \times 10^4$  nm<sup>2</sup>, S.D. =  $9.56 \times 10^4$ ,  $n_{\text{PSD}} = 65$ ,  $N_{\text{animals}} = 3$ ) compared to *Pclo*<sup>wt/wt</sup> rats ( $17.25 \times 10^4 \pm 1.04 \times 10^4$   
 163 nm<sup>2</sup>, S.D. =  $8.61 \times 10^4$ ,  $n_{\text{PSD}} = 70$ ,  $N_{\text{animals}} = 3$ ;  $P < 0.001$ , Mann-Whitney-Wilcoxon Test, Fig 2F).



164

165 **Figure 2. Absence of picolino results in smaller synaptic ribbons and larger PSDs**



166 **(A)** Maximal projections of confocal sections of apical organs of Corti from 2 months old *Pclo<sup>gt/gt</sup>* and  
167 *Pclo<sup>wt/wt</sup>* rats. The whole mounts were co-labeled for IHC cytosol marker parvalbumin (PV, red), synaptic  
168 ribbon marker CtBP2 (green) and piccolo/piccolino (magenta). Scale bars = 10  $\mu$ m. **(B)** Zoom-ins from  
169 insets in (A), (here removing the parvalbumin-channel for clarity) highlight the absence of piccolo-  
170 specific immunofluorescence puncta in and around *Pclo<sup>gt/gt</sup>* IHCs, in contrast to colocalizing CtBP2-  
171 piccolo spots for *Pclo<sup>wt/wt</sup>* IHCs and efferent piccolo immunofluorescence (not colocalising with the  
172 synaptic ribbon). Scale bar = 5  $\mu$ m. **(C)** Triple labeling of homer1 (green), bassoon (blue) and CtBP2 (red),  
173 imaged in 2D-STED (CtBP2) and confocal mode (homer1 and bassoon). The morphology of afferent  
174 synapses of piccolo deficient IHCs appears to be altered with small “compact” ribbons and larger PSDs.  
175 Scale bars = 0.5  $\mu$ m. **(D)** Box plot representing unaltered total number of ribbons (number of CtBP2  
176 puncta;  $n_{\text{IHC}} = 81$ ,  $n_{\text{Corti}} = 8$ ,  $N_{\text{animals}} = 6$  for *Pclo<sup>wt/wt</sup>*; and  $n_{\text{IHC}} = 79$ ,  $n_{\text{Corti}} = 7$ ,  $N_{\text{animals}} = 4$  for *Pclo<sup>gt/gt</sup>*;  $P =$   
177 0.466, t-test) and number of anchored ribbons (number of CtBP2-bassoon juxtapositions;  $n_{\text{IHC}} = 52$ ,  $n_{\text{Corti}}$   
178  $= 6$ ,  $N_{\text{animals}} = 4$  for *Pclo<sup>wt/wt</sup>* and  $n_{\text{IHC}} = 51$ ,  $n_{\text{Corti}} = 5$ ,  $N_{\text{animals}} = 3$  for *Pclo<sup>gt/gt</sup>*;  $P = 0.681$ , t-test). Inlaid points  
179 represent average numbers/IHC drawn from individual organs of Corti. **(E, F)** Box plots of the 2D area of  
180 synaptic ribbons and PSDs respectively, derived by fitting a 2D-Gaussian function to  
181 immunofluorescence data as represented in (C). **(E)**  $n_{\text{ribbons}} = 74$ ,  $N_{\text{animals}} = 3$  for *Pclo<sup>wt/wt</sup>* and  $n_{\text{ribbons}} = 71$ ,  
182  $N_{\text{animals}} = 3$  for *Pclo<sup>gt/gt</sup>*;  $P < 0.001$ , Mann-Whitney-Wilcoxon test. **(F)**  $n_{\text{PSDs}} = 70$ ,  $N_{\text{animals}} = 3$  for *Pclo<sup>wt/wt</sup>* and  
183  $n_{\text{PSDs}} = 65$ ,  $N_{\text{animals}} = 3$  for *Pclo<sup>gt/gt</sup>*;  $P < 0.001$ , Mann-Whitney-Wilcoxon test. **(G, H)** The distance between  
184 the centres of mass of CtBP2 and bassoon spots shows a reduction for piccolo-deficient ribbons ( $P <$   
185 0.01, Mann-Whitney-Wilcoxon test), while the distance between the centres of mass of CtBP2 and  
186 homer1 was comparable ( $P > 0.05$ , Mann-Whitney-Wilcoxon test).  $n_{\text{pairs}} = 75$ ,  $N_{\text{animals}} = 3$  for *Pclo<sup>wt/wt</sup>*;  
187  $n_{\text{pairs}} = 69$ ,  $N_{\text{animals}} = 3$  for *Pclo<sup>gt/gt</sup>*. Throughout, box and whisker plots present median, lower/upper  
188 quartiles and 10–90th percentiles with individual data points overlaid and means shown as crosses.

189

190 Previously, Jing and co-workers have reported ribbon anchorage defects in bassoon gene-trap mutant  
191 mice (Jing et al., 2013). To check for any analogous phenotype upon piccolo disruption, we estimated  
192 the centers of mass of CtBP2, bassoon and homer1 signals and calculated the ribbon-AZ and the ribbon-  
193 PSD center of mass distance. We found a reduction in the ribbon-AZ center of mass distance ( $n_{\text{pairs}} = 69$ ,  
194  $N_{\text{animals}} = 3$  for both groups;  $P < 0.01$ , Mann-Whitney-Wilcoxon Test) in *Pclo<sup>gt/gt</sup>* synapses, whereas the  
195 ribbon-PSD center of mass distance appeared comparable ( $n_{\text{pairs}} = 64$ ,  $N_{\text{animals}} = 3$  for both groups;  $P >$   
196 0.05, t-test) (Fig 2G, H). We speculate that the smaller ribbon size in *Pclo<sup>gt/gt</sup>* IHCs may have resulted in  
197 the smaller ribbon-AZ center of mass distance, while this might not have become obvious for ribbon-PSD  
198 due to their larger and more variable center of mass distance.

199

200 [Large 3D electron microscopic volume reconstructions revealed two distinct ribbon morphologies in](#)  
201 [mutant IHCs](#)

202 In a next step, we performed an ultrastructural analysis in order to determine fine structural changes  
203 beyond those amenable to light microscopy. Focused ion beam-scanning electron microscopy (FIB-SEM)  
204 enabled us to quantify morphological parameters such as ribbon and PSD sizes as well as SV numbers  
205 and their localization within IHCs.

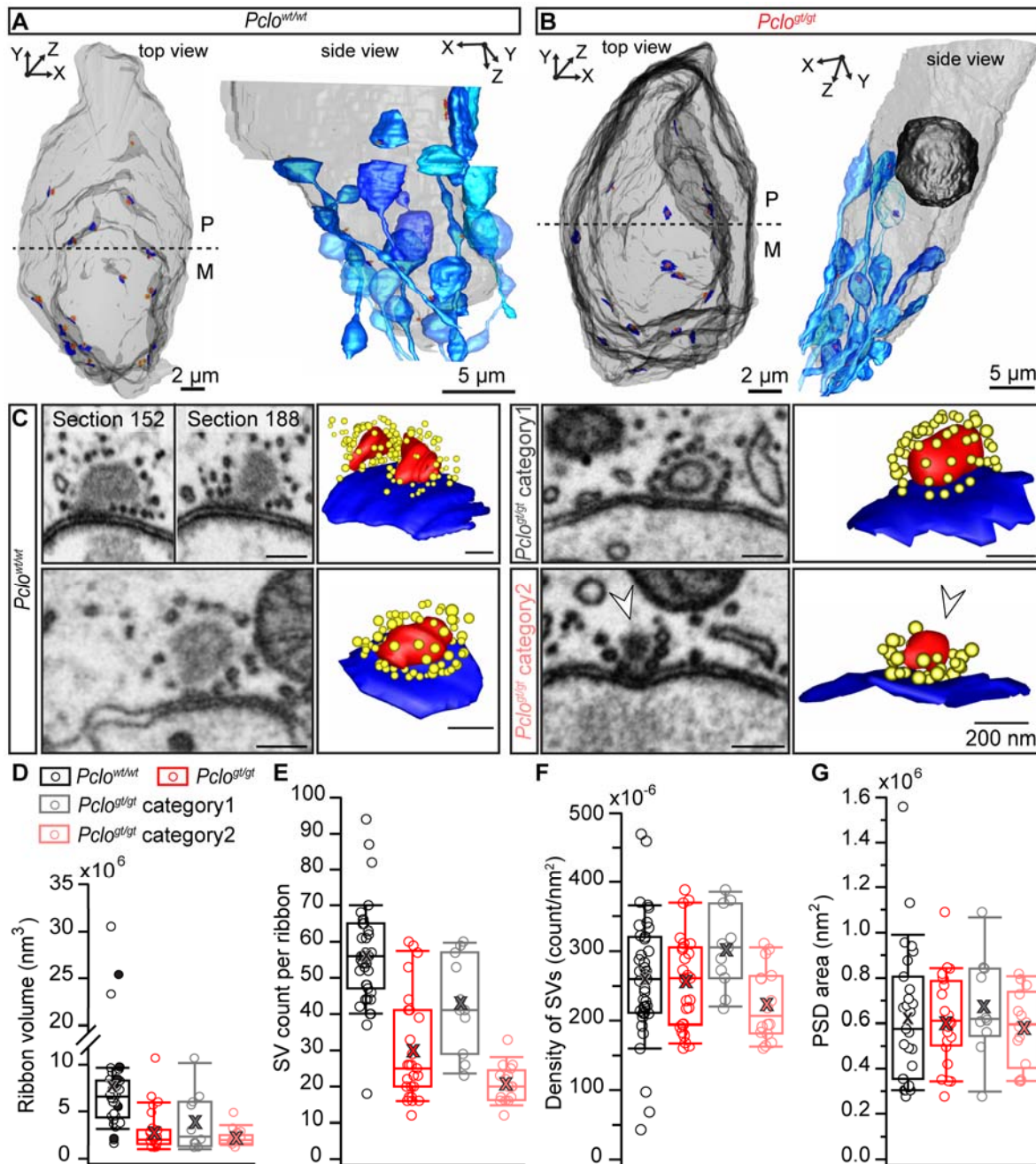
206 We compared the ribbon volume and localization in 2-3 months old adult *Pclo<sup>gt/gt</sup>* and *Pclo<sup>wt/wt</sup>* IHCs (Fig  
207 3A, B; Movie 1,2). While our immunohistochemical data revealed ribbons of *Pclo<sup>gt/gt</sup>* AZs to be smaller on  
208 average, FIB-SEM could distinguish two categories of ribbon-type AZs in *Pclo<sup>gt/gt</sup>* IHCs. They could be  
209 clearly separated by several morphological features: category 1 encompassed ribbons that appeared  
210 comparable to *Pclo<sup>wt/wt</sup>* littermate control ribbons regarding size, shape and SV occupancy. Ribbons  
211 sorted in category 2 appeared smaller, more round in shape and lacked SVs at their membrane-distal  
212 side (Fig 3C). A first guess that these categories might simply reflect the previously described ribbon  
213 number and size difference of modiolar and pillar AZs of IHCs (Hua et al., 2021; Liberman et al., 2011;  
214 Michanski et al., 2019; Ohn et al., 2016; Payne et al., 2021), did not match our data. Category 2 ribbons  
215 seemed to be equally present at the modiolar and the pillar sides of *Pclo<sup>gt/gt</sup>* IHCs. Due to the low IHC  
216 number for the large 3D volume data set we refrained from a statistical analysis. Since the two ribbon  
217 categories robustly differ in size and SV numbers, we analyzed all mutant ribbons together and  
218 additionally analyzed both categories separately. We found that ribbons of category 2 were indeed  
219 smaller with fewer SVs (Fig 3D-F; Appendix Table 1) in contrast to category 1 and *Pclo<sup>wt/wt</sup>* ribbons  
220 ( $2.23 \times 10^6 \text{ nm}^3$  vs.  $3.07 \times 10^6 \text{ nm}^3$  in *Pclo<sup>gt/gt</sup>* category 1 and  $6.74 \times 10^6 \text{ nm}^3$  in *Pclo<sup>wt/wt</sup>*, i.e., category 2  
221 ribbons being 3 times smaller compared to *Pclo<sup>wt/wt</sup>* ribbons). The PSD area appeared unchanged for all  
222 mutant synapses compared to *Pclo<sup>wt/wt</sup>* littermate controls (Fig 3G; Appendix Table 1), which contrasts  
223 our immunofluorescence analysis. Notably, no double ribbons per synaptic contact were observed in

224 *Pclo<sup>gt/gt</sup>* rats, while in both FIB-SEM data sets of *Pclo<sup>wt/wt</sup>* IHCs double ribbons appeared frequently (Fig  
225 3C), in accordance with previous observations for mouse IHCs (Hua et al., 2021; Michanski et al., 2019;  
226 Payne et al., 2021; Sobkowicz et al., 1982; Sobkowicz et al., 1986; Stamataki et al., 2006; Wong et al.,  
227 2014) and our immunofluorescence results.

228         Next to ribbon morphology, the overall distribution of ribbons within an IHC might be changed  
229 in the mutants. Therefore, we quantified the nearest neighbor distance between ribbons in both  
230 genotypes in our FIB-SEM data (Fig EV1E). For *Pclo<sup>wt/wt</sup>* IHCs, we included the distance measurements  
231 between ribbons of the same synaptic contact (indicated as filled points in Fig EV1E). However, no  
232 differences between all *Pclo<sup>gt/gt</sup>* compared to *Pclo<sup>wt/wt</sup>* ribbons could be observed, suggesting that the  
233 distribution of synaptic contacts is normal in *Pclo<sup>gt/gt</sup>* IHCs (Fig EV1E; Appendix Table 1). An analogous  
234 analysis of nearest neighbor distances between ribbons from our immunolabeled confocal sections of  
235 the organs of Corti confirmed these findings since no difference in distances could be found (Fig EV1G,  
236 H). We further noted that mitochondria often appeared in close vicinity to category 2 mutant ribbon  
237 synapses (Fig EV1A-C). Indeed, apposition of mitochondria to category 2 ribbons was closer compared to  
238 *Pclo<sup>wt/wt</sup>* and *Pclo<sup>gt/gt</sup>* category 1 ribbons (Fig EV1D; Appendix Table 1). However, the overall frequency of  
239 mitochondria being in close vicinity to ribbons was comparable between *Pclo<sup>gt/gt</sup>* and *Pclo<sup>wt/wt</sup>* IHCs (Fig  
240 EV1C). Finally, FIB-SEM revealed that larger ribbons frequently harbor a translucent core, regardless of  
241 the genotype (Fig 3C, Fig EV1F), which is in line with previous findings (Lieberman, 1980; Michanski et al.,  
242 2019; Sobkowicz et al., 1982; Stamataki et al., 2006). Interestingly, no translucent core could be found in  
243 the category 2 ribbons of *Pclo<sup>gt/gt</sup>* rats, likely owing to their smaller size.

244         Transmission electron microscopy of ultrathin sections from conventional embeddings further  
245 corroborated these findings: Translucent cores are present in larger ribbons, while smaller ribbons in  
246 *Pclo<sup>gt/gt</sup>* IHCs showed a uniform electron-density and lacked SVs at the upper ribbon part (Fig EV2A,B)  
247 and were thus characterized as category 2. Using an anti-piccolino immunogold labeling with the same

248 antibody as for our immunofluorescence analysis, we found that piccolino was almost equally  
 249 distributed along individual *Pclo*<sup>wt/wt</sup> ribbons of 10-11 months of age, while it seems that ribbons are less  
 250 frequently labeled in *Pclo*<sup>wt/gt</sup> IHCs suggesting a reduction of piccolino molecules in heterozygotes (Fig  
 251 EV2C,D).



252

253 **Figure 3: FIB-SEM revealed two morphological distinct ribbon categories in *Pclo*<sup>gt/gt</sup> inner hair cells.**

254 **(A, B)** 3D visualizations of *Pclo*<sup>wt/wt</sup> and *Pclo*<sup>gt/gt</sup> (2-3 months old) rat IHCs using FIB-SEM displayed in top  
255 view and side view, without or with afferent nerve fiber contacts (different shades of light blue). Based  
256 on the tissue context and the cellular apical-basal axis, the separation of pillar (P) and modiolar (M) sides  
257 was determined. Light gray: IHC membrane, dark gray: nucleus, red: ribbons, dark blue: postsynaptic  
258 density (PSD). **(C)** Representative single sections (left panels) of the reconstructed (right panels) ribbons  
259 (red) with their surrounding synaptic vesicles (SVs, yellow) and opposing PSDs (dark blue). Multi-ribbon  
260 AZs were observed only in *Pclo*<sup>wt/wt</sup> AZs (left upper panel), while *Pclo*<sup>gt/gt</sup> IHCs revealed two  
261 morphological distinct AZ categories (right panel). In contrast to the *Pclo*<sup>wt/wt</sup>-resembling ribbon synapse  
262 architecture in category 1, category 2 ribbon synapses take a roundish shape and lack SVs at the upper  
263 side of the ribbon (white arrowheads). **(D-G)** Box plots with the mean values (cross) and individual data  
264 points display the quantification of ribbon volumes (D), SV counts (E), SV densities (F, SV count values  
265 normalized to the ribbon area) and the PSD area (G), for *Pclo*<sup>wt/wt</sup> and *Pclo*<sup>gt/gt</sup> samples, respectively as  
266 well as an additional separation of the *Pclo*<sup>gt/gt</sup> data into category 1 and category 2 synapses. Black filled  
267 circles in D represent measurements from multi-ribbons AZs.  $N_{\text{animals}} = 2$ ,  $n_{\text{IHCs}} = 2$  respectively for  
268 *Pclo*<sup>wt/wt</sup> and *Pclo*<sup>gt/gt</sup> condition.

269

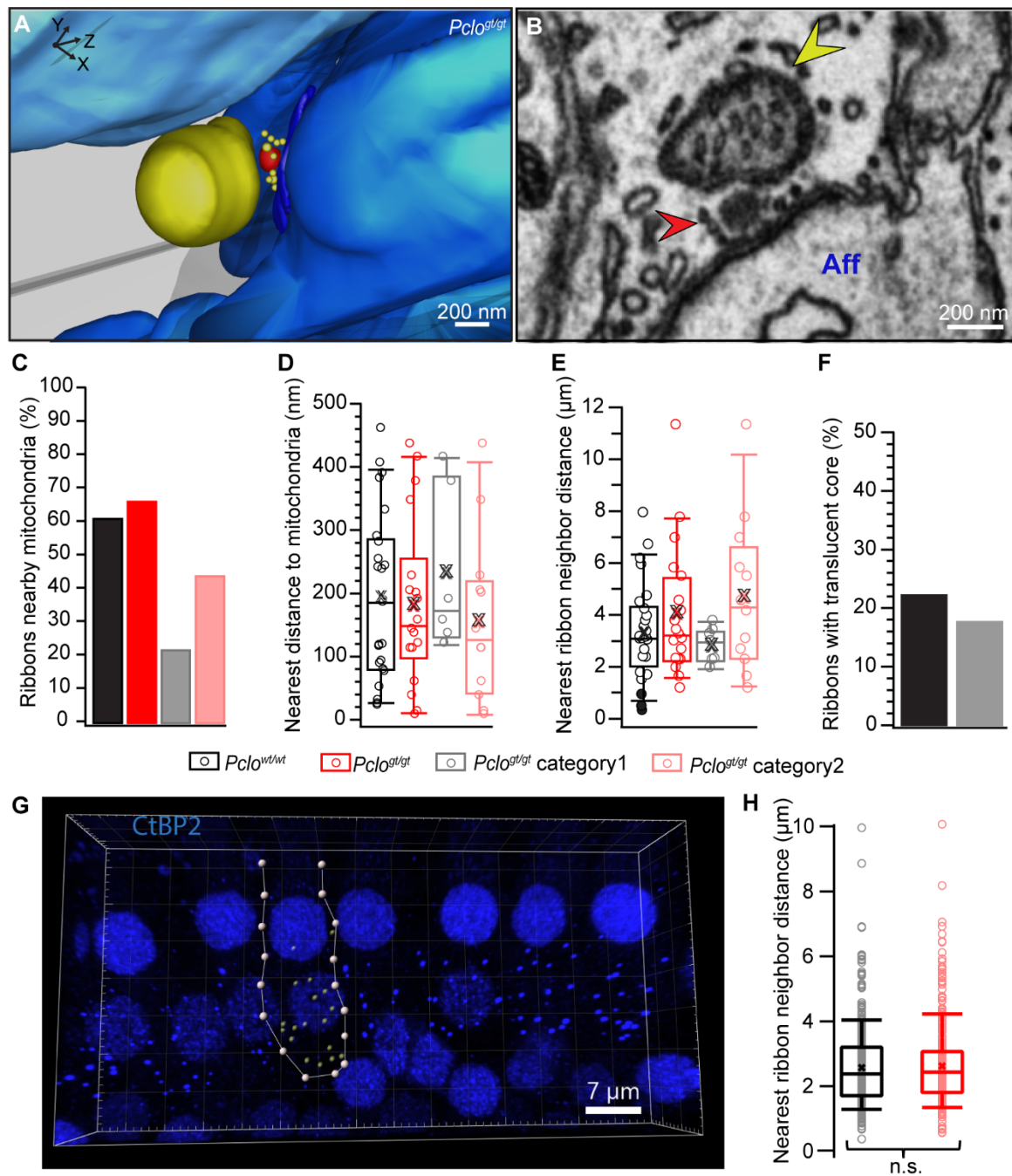
270 **Movie 1 and 2: FIB-SEM visualizations of the nuclear and basal region of *Pclo*<sup>wt/wt</sup> and *Pclo*<sup>gt/gt</sup> cochlear**  
271 **IHCs with corresponding 3D segmentations.**

272 Movies scanning through the FIB-SEM z-stacks of *Pclo*<sup>wt/wt</sup> (Movie 1, 2 months and 4 days old) and  
273 *Pclo*<sup>gt/gt</sup> (Movie 2, 3 months old) IHCs. The displayed 3D models depict IHC contours (transparent gray),  
274 part of the nuclei (dark gray), innervating afferent nerve fibers (blue), ribbon synapses (red), their  
275 corresponding SVs (yellow) and PSDs (dark blue). While multiribbon AZs (highlighted with red arrow) can  
276 be detected in *Pclo*<sup>wt/wt</sup> IHCs, exclusively single ribbons that can be divided into two morphological  
277 distinct categories (highlighted with white arrows) are found in *Pclo*<sup>gt/gt</sup> IHCs.

278 Movie1: <https://owncloud.gwdg.de/index.php/s/ILuJangpAovxArc>

279 Movie2: <https://owncloud.gwdg.de/index.php/s/XFPfoGcwWaMH4H3>

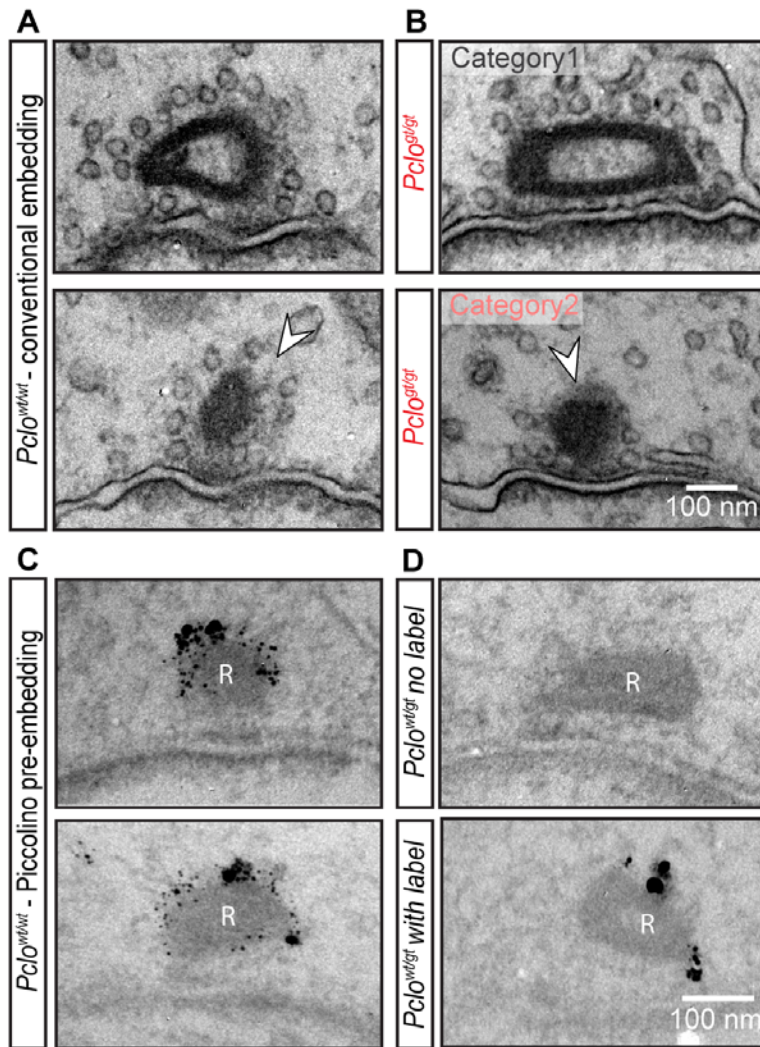
280



281

282 **Fig EV1: Mitochondria tend to be closer to the ribbons of category 2  $Pclo^{gt/gt}$  AZs**  
 283 **(A)** FIB-SEM 3D model and an exemplary section **(B)** of a representative  $Pclo^{gt/gt}$  category 2 ribbon  
 284 (red/arrowhead) with a mitochondrion (dark yellow/arrowhead) nearly touching the upper side of the  
 285 ribbon (devoid of SVs) with an afferent bouton (Aff). **(C)** Analysis of mitochondria-proximal ribbons in a  
 286 range of 500 nm around the ribbon. **(D)** Measurements of the shortest distance between synaptic  
 287 ribbon and mitochondria surfaces. **(E)** Box plot of distance measurements, measured from the surfaces  
 288 of the respective structure, between nearest neighboring synaptic ribbons depicted with individual data  
 289 points and mean values highlighted as a cross. Black filled circles represent the distance measurements  
 290 between the individual ribbons of multi-ribbon AZs. **(F)** Quantification of ribbon counts exhibiting a

291 translucent core reveals this feature only in  $Pclo^{wt/wt}$  ribbons and the larger sized category 1  $Pclo^{gt/gt}$   
292 ribbons (gray) but not in category 2  $Pclo^{gt/gt}$  ribbons.  $N_{animals} = 2$ ,  $n_{IHCs} = 2$  respectively for  $Pclo^{wt/wt}$  and  
293  $Pclo^{gt/gt}$  condition. **(G)** Immunofluorescent spots corresponding to synaptic ribbons (labeled with an  
294 antibody against CtBP2/RIBEYE) were detected using Imaris 9.6 (Oxford Instruments) in confocal 3D  
295 projections of apical organs of Corti from 2 months old  $Pclo^{wt/wt}$  and  $Pclo^{gt/gt}$  rats. Yellow spots in  
296 exemplary image shown here represent detected ribbons within one IHC. **(H)** Nearest ribbon neighbor  
297 distance was measured between spot centers and appears comparable between  $Pclo^{wt/wt}$  and  $Pclo^{gt/gt}$   
298 conditions, ( $P > 0.05$ , Mann-Whitney-Wilcoxon test), in agreement with FIB-SEM data shown in (E).  
299  $n_{ribbons} = 435$ ,  $n_{IHCs} = 33$ ,  $N_{animals} = 3$  for  $Pclo^{wt/wt}$  and  $n_{ribbons} = 396$ ,  $n_{IHCs} = 32$ ,  $N_{animals} = 3$  for  $Pclo^{gt/gt}$ .  
300



301

302 **Fig EV2: 2D Transmission electron microscopy corroborates the notion of 2 ribbon categories in**  
303  **$Pclo^{gt/gt}$  as well as in  $Pclo^{wt/gt}$  inner hair cells – immuno-electron microscopical detection of piccolino**  
304 **(A)**  $Pclo^{wt/wt}$  ribbons with (upper panel) and without a translucent core (lower panel). Ribbons show a SV  
305 distribution along the full ribbon surface (arrowhead). **(B)**  $Pclo^{gt/gt}$  category 1 (upper panel) with a  
306 translucent core and category 2 (lower panel) with a lack of SVs at the upper ribbon side (arrowhead).  
307 **(C, D)** Representative examples of an anti-piccolino pre-embedding immunogold labeling, which can be  
308 found around the synaptic ribbons (R) in  $Pclo^{wt/wt}$  (C) and  $Pclo^{wt/gt}$  (D) IHCs. (D) In  $Pclo^{wt/gt}$  IHCs, most

309 synaptic ribbons lacked anti-piccolino labeling (upper panel). However, for few ribbons the occurrence  
310 of silver enhanced gold particles could be observed (lower panel).  
311

	<i>Pclo</i> <sup>wt/wt</sup>	<i>Pclo</i> <sup>gt/gt</sup>	<i>Pclo</i> <sup>gt/gt</sup> category 1	<i>Pclo</i> <sup>gt/gt</sup> category 2
<b>Ribbon volume (nm<sup>3</sup>) x10<sup>6</sup></b>	7.82 ± 0.95	3.09 ± 0.42	4.00 ± 0.92	2.37 ± 0.21
<b>SV count</b>	56.05 ± 2.22	29.78 ± 2.76	42.91 ± 3.99	20.75 ± 1.31
<b>SV density x10<sup>-6</sup></b>	259.96 ± 14.29	261.05 ± 12.76	305.91 ± 17.18	206.32 ± 13.03
<b>PSD area (nm<sup>2</sup>) x10<sup>6</sup></b>	0.63 ± 0.06	0.60 ± 0.04	0.68 ± 0.07	0.58 ± 0.04
<b>NND mitochondria (nm)</b>	198.04 ± 27.13	185.16 ± 31.27	234.79 ± 52.74	160.34 ± 38.29
<b>NND ribbons (μm)</b>	3.40 ± 0.38	4.08 ± 0.58	2.89 ± 0.26	4.77 ± 0.85

312 **Appendix Table 1: FIB-SEM data on count, size and distance measurements of AZ parameters.**

313 Data are presented as mean ± SEM. Abbreviations: SV = synaptic vesicles, PSD = postsynaptic density,  
314 NND = nearest neighbor distance.

315

316

317 [Electron tomography reveals fewer ribbon-associated SVs at category 2 mutant AZs but a normal fraction  
318 of ribbon-SV filaments](#)

319 Next, we analyzed the morphologically distinct SV pools of ribbon synapses and SV tethering as piccolino  
320 was shown to interact with RIBEYE and proposed to support the SV trafficking via interacting with other  
321 presynaptic proteins. We studied ribbon-associated (RA) and membrane-proximal (MP) SV pools, as well  
322 as their tethering using electron tomography combined with high-pressure freezing and freeze  
323 substitution (HPF/FS) which enables high resolution with a close-to-native structural preservation of  
324 ribbons, SVs and filaments (Chakrabarti et al., 2018).

325 We could verify the two ribbon categories in *Pclo*<sup>gt/gt</sup> IHCs, with normal *Pclo*<sup>wt/wt</sup> resembling ribbons  
326 (category 1) and altered, small and spherical ribbons, void of membrane-distal SVs (category 2) (Fig 4A-  
327 C). Consequently, as for the FIB-SEM data, we determined all morphometric parameters (shown in Fig  
328 4D) for all *Pclo*<sup>gt/gt</sup> AZs combined and separated into category 1 and 2. For the grouping of the  
329 reconstructed ribbons of *Pclo*<sup>gt/gt</sup> rats, we performed the K-means clustering analysis, which confirmed  
330 our blinded and manual annotation of AZs into category 1 and 2, including all *Pclo*<sup>gt/gt</sup> and *Pclo*<sup>wt/wt</sup>  
331 tomograms. Notably, in the manual analysis, none of the *Pclo*<sup>wt/wt</sup> AZs were sorted in category 2,  
332 confirming that this is a morphological category only found in the mutants. Considering all mutant



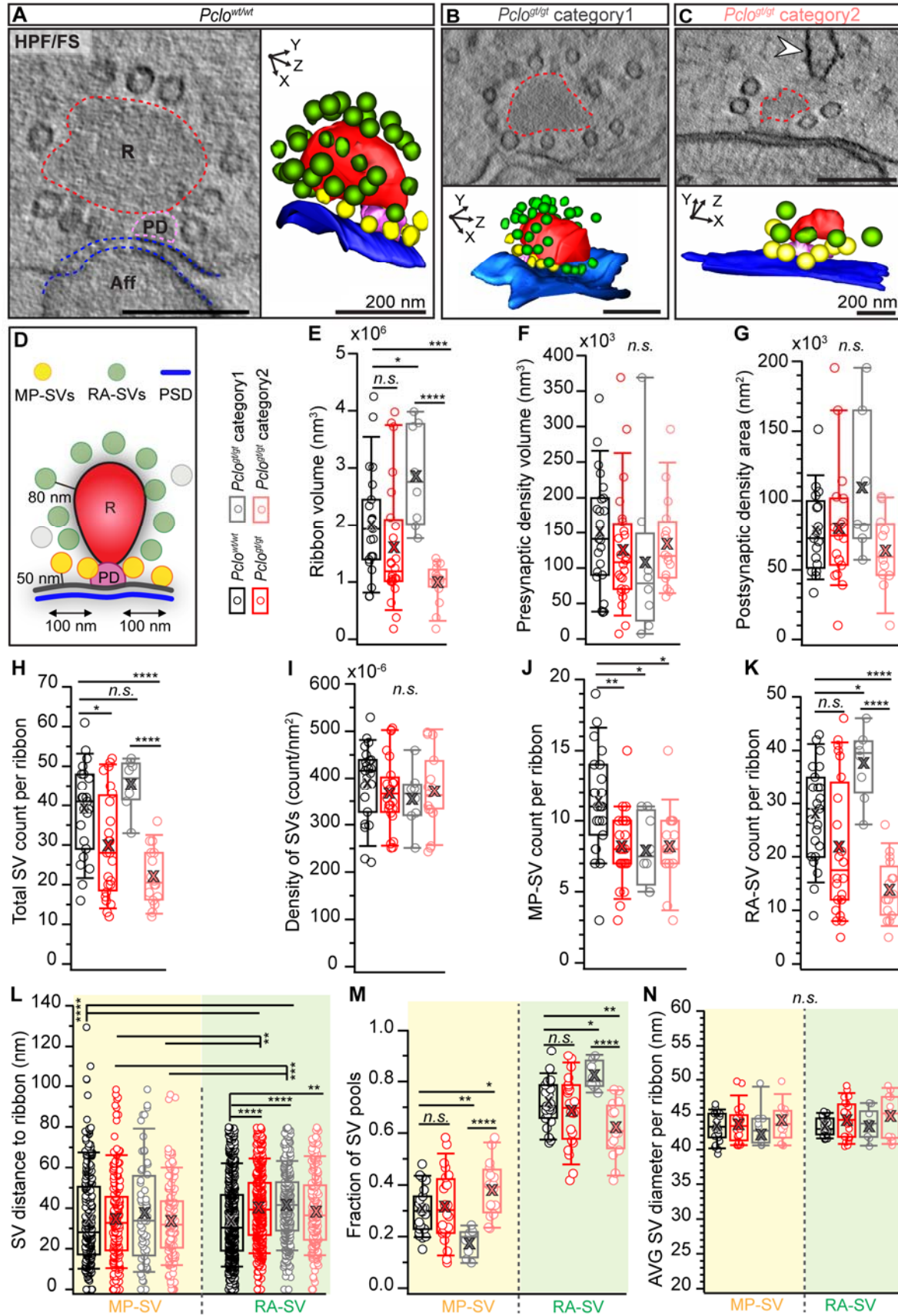
333 ribbons ( $Pclo^{gt/gt}$ ), most of the parameters were comparable to  $Pclo^{wt/wt}$  (Fig 4E-G; Appendix Table 2), but  
334 significantly fewer SVs were observed at  $Pclo^{gt/gt}$  AZs (Fig 4H), while the differences in SV density did not  
335 reach significance (Fig 4I). Furthermore, we observed a consistent difference in all our morphometric  
336 parameters between category 1 and 2  $Pclo^{gt/gt}$  AZs. Interestingly, the ribbon volume, the PSD area, the  
337 total SV count per ribbon as well as the RA-SV count were even increased in category 1 AZs in  
338 comparison to  $Pclo^{wt/wt}$  AZs (Fig 4E,G,H,K; Appendix Table 2). However, the PSD area difference did not  
339 reach significance in contrast to our immunofluorescence data. This discrepancy might arise from the  
340 limited section thickness of 250 nm for electron tomography, which does not allow for a full  
341 reconstruction of the PSD extent.

342 Ultrastructural quantification of the two morphological SV pools (described in (Chakrabarti et  
343 al., 2018)) revealed a reduction in the number of MP-SVs in category 1 and 2 AZs separately as well as in  
344 the combined mutant dataset (Fig 4J; Appendix Table 3). Consistent with our FIB-SEM data, ribbons of  
345 category 2 AZs lacked SVs at their membrane-distal side (Fig 4K). However, this did not affect the SV  
346 density per ribbon surface area (Fig 4I). Moreover, RA-SV seemed to be further away from the synaptic  
347 ribbon in both mutant AZ categories (Fig 4L; Appendix Table 3). Next, we investigated the fractions of  
348 the SV-pools following our previously published approach (Chakrabarti et al., 2018). The MP- and the  
349 RA-SV pool fractions were comparable between the combined mutant ribbon synapses and the  
350 littermate controls (Fig 4M; Appendix Table 3). As expected from the above results, category 1 and  
351 category 2 AZs showed opposing effects: while in category 1, the fraction of MP-SVs was significantly  
352 reduced, it was strikingly increased in  $Pclo^{gt/gt}$  category 2 AZs, which was significant when compared to  
353  $Pclo^{gt/gt}$  category 1 and  $Pclo^{wt/wt}$  AZs. Such an opposite effect was also found for the RA-SVs that were  
354 fewer in category 2 but increased in category 1 compared to  $Pclo^{wt/wt}$  AZs, explaining why we did not  
355 observe overall changes when combining all mutant AZs (Fig 4M; Appendix Table 3). The analysis of SV

356 sizes from the different pools resulted in uniformly sized diameters for all groups (Fig 4N; Appendix  
357 Table 3).

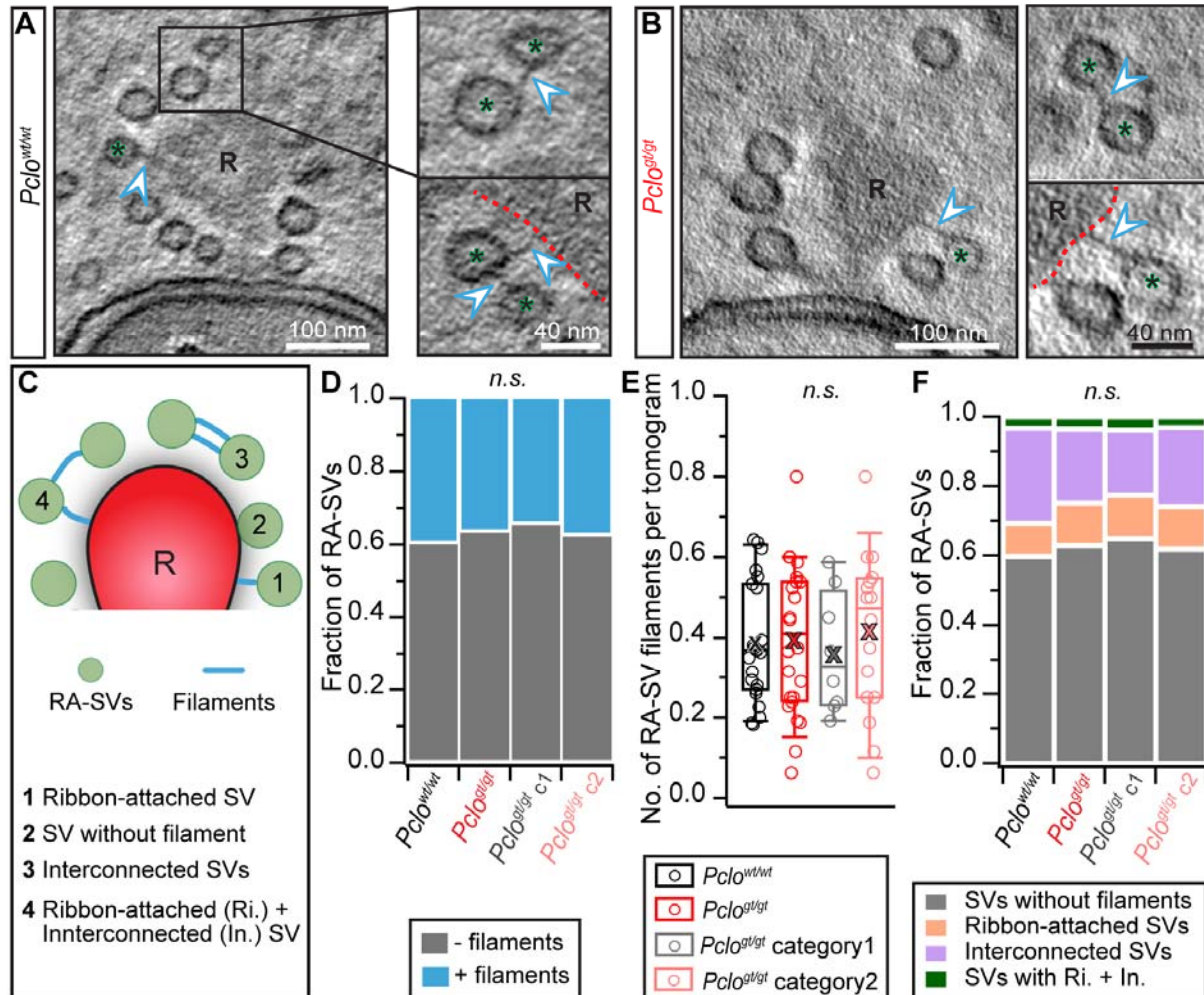
358 As tethering of SVs to the ribbon might involve ribbon-standing piccolo, we investigated the tethering  
359 of the RA-SVs analyzing the filament number and to which structures the SVs connect to. These different  
360 tethering states were previously stated as morphological SV subpools, which are present at the ribbon  
361 as well as at the membrane (Chakrabarti et al., 2018). In this study, we focused on the RA-SVs since  
362 piccolo was shown to localize exclusively to the ribbon (Dick et al., 2001, 20; Limbach et al., 2011;  
363 Michanski et al., 2019). Filaments could be observed at both, *Pclo<sup>wt/wt</sup>* and *Pclo<sup>gt/gt</sup>* ribbon synapses (Fig  
364 5A,B). When counting the number of filaments per ribbon (Fig 5D) or alternatively the numbers of all  
365 filaments per tomogram (Fig 5E), we did not observe any significant differences (Appendix Table 4).  
366 Subsequently, we quantified the different RA-SV-subpools as done in (Chakrabarti et al., 2018) but no  
367 changes could be detected (Fig 5F; Appendix Table 4). Therefore, we conclude that tethering of the  
368 remaining ribbon-associated SVs of piccolo-deficient IHC synapses is unchanged.

369 Finally, we found cisternal structures in close ribbon proximity at *Pclo<sup>gt/gt</sup>* ribbon synapses (Fig. 4C, Fig  
370 EV3; Appendix Table 4). In category 2 *Pclo<sup>gt/gt</sup>* IHCs, these cisternal structures could frequently be  
371 observed close to the SV lacking upper ribbon part (Fig EV3B). Similar observations were made in IHCs  
372 upon disruption of bassoon (Khimich et al., 2005) and the endocytic proteins AP2 and endophilins (Jung  
373 et al., 2015b; Kroll et al., 2019). Moreover, similar cisternal structures have been reported in  
374 hippocampal synapses of *Pclo<sup>gt/gt</sup>* rats. The precise identity of these structures, which have been referred  
375 to as endosome-like vacuoles remains to be determined.



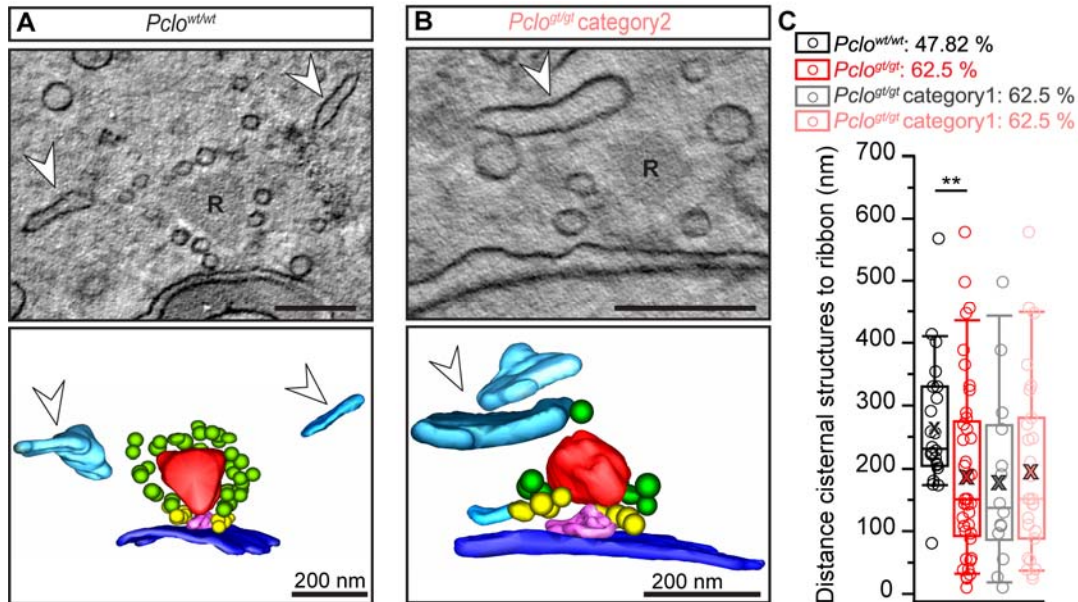
377 **Figure 4: Electron tomography reveals smaller ribbons and fewer RA-SVs in *Pclo*<sup>gt/gt</sup> category 2 AZs**

378 **(A-C)** Representative virtual electron tomographic sections with their corresponding 3D models of  
379 *Pclo*<sup>wt/wt</sup> (A,) and *Pclo*<sup>gt/gt</sup> IHCs (B, C) obtained after HPF/FS from 1-2 months old rats. Reconstructions  
380 (right panels) show the ribbon (R in left panels) in red, the presynaptic density (PD) in magenta,  
381 membrane-proximal synaptic vesicles (MP-SVs) in yellow, ribbon-associated synaptic vesicles (RA-SVs) in  
382 green, the postsynaptic density (PSD) of the afferent bouton terminal (Aff) in blue. Based on an  
383 unsupervised K-means clustering, *Pclo*<sup>gt/gt</sup> ribbon synapses were also divided into category 1 and  
384 category 2 AZs. Compared to *Pclo*<sup>wt/wt</sup> and category 1 AZs, the upper (membrane-distal) ribbon side of  
385 category 2 AZs was devoid of RA-SVs but frequently faced cisternal structures (arrowhead). **(D)**  
386 Schematic illustration of tomogram analysis. **(E-N)** Box plots with individual data points and mean values  
387 highlighted as crosses show the quantification of the specific parameters. While smaller ribbons were  
388 observed for *Pclo*<sup>gt/gt</sup> category 2 AZs and larger sized ribbons for *Pclo*<sup>gt/gt</sup> category 1 (E), no significant  
389 differences were detected for PD (F) and PSD (G) sizes. Significantly less SVs per ribbon were observed in  
390 *Pclo*<sup>gt/gt</sup> deriving mainly from the category 2 (H). The SV density (SV counts normalized to the ribbon  
391 area) was unaltered in *Pclo*<sup>gt/gt</sup> AZs (pooled or per category). Analysis of the two different SV pools  
392 showed equally reduced MP-SV counts for all *Pclo*<sup>gt/gt</sup> analysis groups (J). Significantly fewer RA-SVs were  
393 found in the *Pclo*<sup>gt/gt</sup> category 2, while more were present in *Pclo*<sup>gt/gt</sup> category 1 (K). Nearest distance  
394 measurements from the SV to the ribbon demonstrated increased distances for the RA-SV pool in all  
395 three *Pclo*<sup>gt/gt</sup> analysis groups (L). Opposing results regarding the SV pool fraction between category 1  
396 and category 2 *Pclo*<sup>gt/gt</sup> AZs were detected (M). While a greater fraction of MP-SVs was found in the  
397 category 2 than in category 1, the RA-SV fraction was significantly decreased in category 2 in comparison  
398 to category 1. **(N)** No differences between *Pclo*<sup>wt/wt</sup> and *Pclo*<sup>gt/gt</sup> in the SV diameter were observed for  
399 either SV pool. *Pclo*<sup>wt/wt</sup>:  $N_{\text{animals}} = 3$ ,  $n_{\text{ribbons}} = 23$ ,  $n_{\text{PSDs}} = 17$ ; *Pclo*<sup>gt/gt</sup>:  $N_{\text{animals}} = 4$ ,  $n_{\text{ribbons}} = 24$ ,  $n_{\text{PSDs}} = 19$ ;  
400 Category 1:  $n_{\text{ribbons}} = 8$ ,  $n_{\text{PSDs}} = 7$ ; Category 2:  $n_{\text{ribbons}} = 16$ ,  $n_{\text{PSDs}} = 12$ . Significant differences between two  
401 groups were analysed with the t-test or the Mann–Whitney Wilcoxon test (E-K, M). For multiple  
402 comparisons, ANOVA followed by the post-hoc Tukey (E-K, M, N) or KW test followed by NPMC test (L)  
403 was performed. For more detailed information see also Appendix Table 2,3.



404

405 **Figure 5: Normal tethering of synaptic vesicles at *Pclo<sup>gt/gt</sup>* ribbons**  
 406 **(A,B)** Exemplary virtual electron tomographic sections of *Pclo<sup>wt/wt</sup>* and *Pclo<sup>gt/gt</sup>* ribbon synapses (ribbon  
 407 highlighted with “R” and/or red dotted line). Proteinaceous filaments of different types (Ri: ribbon-  
 408 attached, In: interconnected, and both Ri and In; filaments are marked with arrowheads) were detected  
 409 at RA-SVs (asterisks) in both *Pclo<sup>wt/wt</sup>* and *Pclo<sup>gt/gt</sup>* IHCs. **(C)** Illustration of the various tethering states of  
 410 RA-SVs. **(D,E)** The fraction of RA-SVs with and without filaments (D) as well as the total number of RA-SV  
 411 filaments per tomogram (E) in *Pclo<sup>gt/gt</sup>* was comparable to *Pclo<sup>wt/wt</sup>* (t-test and ANOVA with post-hoc  
 412 Tukey test). **(F)** The graph represents the fraction of RA-SVs around the ribbon regarding the filament  
 413 type. No changes in the occurrence of individual filament types could be found. Multiple comparison  
 414 tests of the filament types were performed using ANOVA with the post-hoc Tukey test (without  
 415 filaments, Ri., In.) or KW test followed by NPMC test (Ri. + In.). *Pclo<sup>wt/wt</sup>*:  $N_{\text{animals}} = 3$ ,  $n_{\text{ribbons}} = 23$ ; *Pclo<sup>gt/gt</sup>*:  
 416  $N_{\text{animals}} = 4$ ,  $n_{\text{ribbons}} = 24$ ; Category 1:  $n_{\text{ribbons}} = 8$ ; Category 2:  $n_{\text{ribbons}} = 16$ . For more detailed information  
 417 see Appendix Table 4.



418  
419  
420  
421  
422  
423  
424  
425  
426  
427  
428  
429

**Fig EV3: Cisternal structures close to ribbon synapses frequently occur in *Pclo*<sup>gt/gt</sup> IHCs**

(A,B) Individual virtual electron tomographic sections of HPF/FS IHCs depicting a *Pclo*<sup>wt/wt</sup> (A) and a *Pclo*<sup>gt/gt</sup> (B) ribbon synapse (upper panel) with their corresponding 3D models (lower panel). Ribbons (R) are represented in red, presynaptic densities in magenta, MP-SVs in yellow, RA-SVs in green, postsynaptic densities in dark blue and cisternal structures in cyan, which are additionally highlighted with arrowheads. (C) Cisternal structures within a 1  $\mu$ m range are closer to ribbons at *Pclo*<sup>gt/gt</sup> AZs ( $P = 0.009$ , Mann–Whitney Wilcoxon test, for multiple comparison KW followed by NPMC test). *Pclo*<sup>wt/wt</sup>:  $N_{\text{animals}} = 3$ ,  $n_{\text{ribbons}} = 23$ ; *Pclo*<sup>gt/gt</sup>:  $N_{\text{animals}} = 4$ ,  $n_{\text{ribbons}} = 24$ ; Category 1:  $n_{\text{ribbons}} = 8$ ; Category 2:  $n_{\text{ribbons}} = 16$ . For more detailed information see Appendix Table 4.

	Ribbon volume (nm <sup>3</sup> ) $\times 10^6$	PD volume (nm <sup>3</sup> ) $\times 10^3$	PSD area (nm) $\times 10^3$	Total SV count	SV density $\times 10^{-6}$
<i>Pclo</i> <sup>wt/wt</sup>	2.00 $\pm$ 0.19	151.75 $\pm$ 16.79	77.55 $\pm$ 7.28	38.91 $\pm$ 2.41	391.91 $\pm$ 16.68
<i>Pclo</i> <sup>gt/gt</sup>	1.61 $\pm$ 0.22	125.56 $\pm$ 17.06	80.15 $\pm$ 9.92	29.92 $\pm$ 2.68	368.75 $\pm$ 15.39
<i>Pclo</i> <sup>gt/gt</sup> category1 (c1)	2.86 $\pm$ 0.31	107.75 $\pm$ 41.28	109.62 $\pm$ 19.56	45.50 $\pm$ 2.27	356.94 $\pm$ 21.56
<i>Pclo</i> <sup>gt/gt</sup> category2 (c2)	0.99 $\pm$ 0.84	134.46 $\pm$ 15.99	62.96 $\pm$ 7.78	22.13 $\pm$ 1.78	374.67 $\pm$ 20.71
<b>P-values</b>	**** <i>P</i> c1 vs. c2  *** <i>P</i> =0.0005 <i>Pclo</i> <sup>wt/wt</sup> vs. c2  * <i>P</i> =0.031 <i>Pclo</i> <sup>wt/wt</sup> vs. c1  <i>n.s.</i> <i>Pclo</i> <sup>wt/wt</sup> vs. <i>Pclo</i> <sup>gt/gt</sup>	<i>n.s.</i>	<i>n.s.</i>	**** <i>P</i> <i>Pclo</i> <sup>wt/wt</sup> vs. c2  **** <i>P</i> c1 vs. c2  * <i>P</i> =0.016 <i>Pclo</i> <sup>wt/wt</sup> vs. <i>Pclo</i> <sup>gt/gt</sup>  <i>n.s.</i> <i>Pclo</i> <sup>wt/wt</sup> vs. c1	<i>n.s.</i>

430 **Appendix Table 2: Counts and size measurements of AZ structures observed by HPF/FS electron**  
 431 **tomography.**

432 Data are presented as mean  $\pm$  SEM. *P*-values between two groups were calculated using the t-test or the  
 433 Mann–Whitney Wilcoxon test. For multiple comparisons, the ANOVA test with post-hoc Tukey test or  
 434 KW followed by NPMC test was performed. Non-significant differences are indicated as *n.s.*, significant  
 435 differences as  $*P < 0.05$ ,  $**P < 0.01$ ,  $***P < 0.001$ ,  $****P < 0.0001$ . Abbreviations: PD = presynaptic  
 436 density, PSD = postsynaptic density, SV = synaptic vesicle.

437

	Count		SV distance (nm)		SV fraction		SV diameter (nm)	
	MP-SV	RA-SV	MP-SV	RA-SV	MP-SV	RA-SV	MP-SV	RA-SV
<i>Pclo</i> <sup>wt/wt</sup>	11.30 $\pm$ 0.75	28.04 $\pm$ 1.90	34.72 $\pm$ 1.42	33.52 $\pm$ 0.76	0.30 $\pm$ 0.02	0.72 $\pm$ 0.02	43.17 $\pm$ 0.43	43.35 $\pm$ 0.27
<i>Pclo</i> <sup>gt/gt</sup>	8.17 $\pm$ 0.53	21.75 $\pm$ 2.60	35.07 $\pm$ 1.53	40.28 $\pm$ 0.77	0.32 $\pm$ 0.03	0.69 $\pm$ 0.03	43.54 $\pm$ 0.52	44.27 $\pm$ 0.53
<i>Pclo</i> <sup>gt/gt</sup> category1 (c1)	8.00 $\pm$ 0.87	37.50 $\pm$ 2.29	37.76 $\pm$ 3.18	41.50 $\pm$ 0.98	0.18 $\pm$ 0.02	0.82 $\pm$ 0.02	42.21 $\pm$ 0.51	43.26 $\pm$ 0.70
<i>Pclo</i> <sup>gt/gt</sup> category2 (c2)	8.25 $\pm$ 0.68	13.88 $\pm$ 1.40	33.76 $\pm$ 1.68	38.62 $\pm$ 1.21	0.38 $\pm$ 0.03	0.62 $\pm$ 0.03	44.21 $\pm$ 0.69	44.78 $\pm$ 0.70
<b><i>P</i>-values</b>	$**P=0.001$ <i>Pclo</i> <sup>wt/wt</sup> vs. <i>Pclo</i> <sup>gt/gt</sup>  $*P=0.037$ <i>Pclo</i> <sup>wt/wt</sup> vs. c1  $*P=0.013$ <i>Pclo</i> <sup>wt/wt</sup> vs. c2	$****P$ c2 vs. <i>Pclo</i> <sup>wt/wt</sup>  $****P$ c1 vs. c2  $*P=0.012$ <i>Pclo</i> <sup>wt/wt</sup> vs. c1  <i>n.s.</i> <i>Pclo</i> <sup>wt/wt</sup> vs. <i>Pclo</i> <sup>gt/gt</sup>	$****P$ <i>Pclo</i> <sup>wt/wt</sup> vs. <i>Pclo</i> <sup>gt/gt</sup> & c1  $***P=0.0007$ c2 MP- SV vs. c1 RA-SV  $***P=0.0003$ <i>Pclo</i> <sup>gt/gt</sup> MP-SV vs. c1 RA-SV  $**P=0.003$ <i>Pclo</i> <sup>gt/gt</sup> MP-SV vs. <i>Pclo</i> <sup>gt/gt</sup> RA- SV  $**P=0.004$ c2 MP-SV vs. <i>Pclo</i> <sup>gt/gt</sup> RA-SV  RA-SV: $****P$ <i>Pclo</i> <sup>wt/wt</sup> vs. <i>Pclo</i> <sup>gt/gt</sup> & c1  $**P=0.016$ <i>Pclo</i> <sup>wt/wt</sup> vs. c2	MP-SV: $****P$ c1 vs. c2  $**P=0.006$ <i>Pclo</i> <sup>wt/wt</sup> vs. c1  $*P=0.019$ <i>Pclo</i> <sup>wt/wt</sup> vs. c2  <i>n.s.</i> <i>Pclo</i> <sup>wt/wt</sup> vs. <i>Pclo</i> <sup>gt/gt</sup>  RA-SV: $****P$ c1 vs. c2  $*P=0.022$ <i>Pclo</i> <sup>wt/wt</sup> vs. c1  $**P=0.004$ <i>Pclo</i> <sup>wt/wt</sup> vs. c2  <i>n.s.</i> <i>Pclo</i> <sup>wt/wt</sup> vs. <i>Pclo</i> <sup>gt/gt</sup>	<i>n.s.</i>			

438 **Appendix Table 3: Counts, size and distance measurements of MP and RA-SV pools from HPF/FS**  
 439 **electron tomography.**

440 Data are presented as mean  $\pm$  SEM. Depending on the normality and equality of variances, significant  
 441 differences between two groups were analyzed with the t-test or the Mann–Whitney Wilcoxon test. For  
 442 multiple comparisons, the ANOVA test with post-hoc Tukey test or KW followed by NPMC test was  
 443 performed. Non-significant differences are indicated as *n.s.*, significant differences as  $*P < 0.05$ ,  
 444  $**P < 0.01$ ,  $***P < 0.001$ ,  $****P < 0.0001$ . Abbreviations: MP-SV = membrane-proximal synaptic vesicle,  
 445 RA-SV = ribbon-associated synaptic vesicle.

446

	Fraction of tethers		No. of tethers per tomogram	Fraction of filament types			Distance cisternal structures	
	-	+		Ri.	In.	Ri.+In.		
<i>Pclo</i> <sup>wt/wt</sup>	0.60	0.40	0.39 ± 0.03	0.60	0.10	0.27	0.03	266.54 ± 22.25
<i>Pclo</i> <sup>gt/gt</sup>	0.63	0.37	0.40 ± 0.04	0.63	0.12	0.21	0.03	191.82 ± 22.15
<i>Pclo</i> <sup>gt/gt</sup> category1 (c1)	0.65	0.35	0.36 ± 0.05	0.65	0.12	0.19	0.04	179.70 ± 37.24
<i>Pclo</i> <sup>gt/gt</sup> category2 (c2)	0.62	0.38	0.41 ± 0.05	0.62	0.12	0.23	0.03	198.10 ± 27.96
<b>P-values</b>	<i>n.s.</i>		<i>n.s.</i>	<i>n.s.</i>				** <i>P</i> =0.009 <i>Pclo</i> <sup>wt/wt</sup> vs. <i>Pclo</i> <sup>gt/gt</sup>

447 **Appendix Table 4: Electron tomographical tether analysis for RA-SVs.**

448 Data are presented as mean ± SEM. Depending on the normality and equality of variances tests,  
 449 significant differences between two groups were analyzed with the t-test or the Mann–Whitney  
 450 Wilcoxon test. For multiple comparisons, the ANOVA test followed by post-hoc Tukey test or the KW  
 451 followed by NPMC test was performed. Non-significant differences are indicated as *n.s.*, significant  
 452 differences as \**P* < 0.05, \*\**P* < 0.01, \*\*\**P* < 0.001, \*\*\*\**P* < 0.0001. The abbreviation - stands for without,  
 453 + for with, Ri. for ribbon attached, In. for interconnected.

454

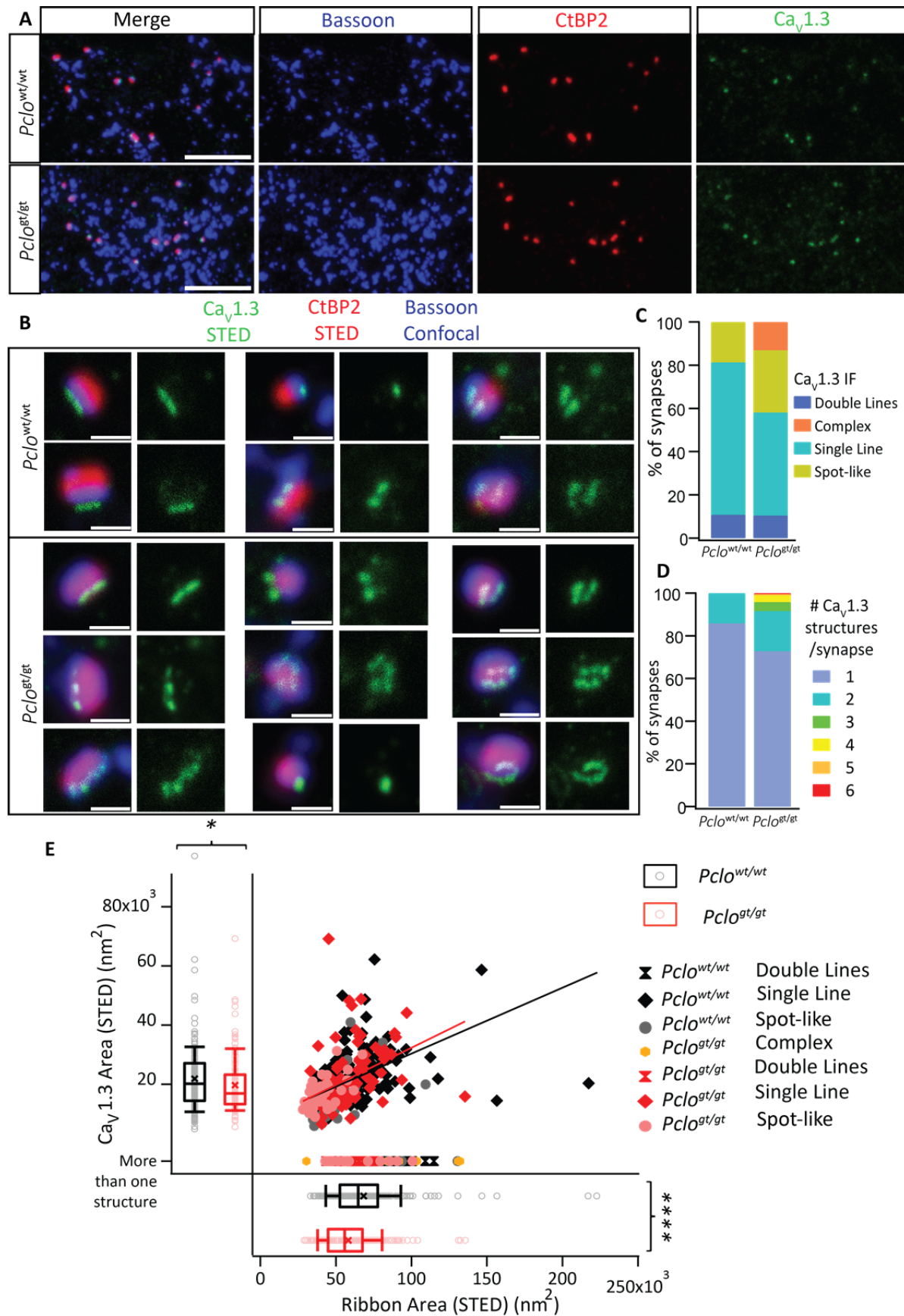
455 [Impaired Ca<sup>2+</sup> channel clustering in mutant animals](#)

457 Previous studies often reported altered Ca<sup>2+</sup> channel clustering upon the disruption of presynaptic  
 458 scaffold proteins at ribbon-type AZs (reviews in Moser et al., 2019; Pangrsic et al., 2018). For instance,  
 459 disruption of bassoon, RIM, RIM-BP2 as well as RIBEYE impairs Ca<sup>2+</sup> channel clustering at IHC AZs (Frank  
 460 et al., 2010; Jean et al., 2018; Jung et al., 2015a; Krinner et al., 2017; Neef et al., 2018). To investigate  
 461 the impact of piccolino disruption on Ca<sup>2+</sup> channel clustering, we stained acutely dissected organs of  
 462 Corti from 2-3 weeks old rats, as employed for IHC physiology (see below), using antibodies against  
 463 Ca<sub>v</sub>1.3 channels, bassoon and CtBP2 and performed 2D-STED imaging (Fig 6A,B). We randomly selected  
 464 and imaged 176 synapses from *Pclo*<sup>wt/wt</sup> (N<sub>animals</sub> = 3) and 191 synapses from *Pclo*<sup>gt/gt</sup> (N<sub>animals</sub> = 3) and  
 465 categorized them based on the morphology of Ca<sup>2+</sup> channel clusters into single-line, double-line, spot-  
 466 like, and complex clusters (Fig 6B), as has been previously described (Jean et al., 2018; Krinner et al.,  
 467 2017; Neef et al., 2018). The subjective categorization generated comparable outcomes when



468 performed by different observers. In control littermates, up to 70.5% of Ca<sub>v</sub>1.3 clusters appeared as a  
469 single line, while smaller fractions appeared as double lines (10.8%) and spot-like (round) clusters  
470 (18.7%). Of the *Pclo<sup>gt/gt</sup>* Ca<sub>v</sub>1.3 clusters, on the contrary, only about 47.7% appeared as single lines and  
471 10.5% as double lines, while 28.8% of them showed a spot-like shape. Additionally, several Ca<sub>v</sub>1.3  
472 clusters in *Pclo<sup>gt/gt</sup>* synapses appeared as fragmented lines and rings seemingly composed of multiple  
473 smaller substructures, which we categorized as complex clusters (remaining 13.1%; Fig 6C). Likely as a  
474 corollary, we noted more Ca<sub>v</sub>1.3 structures at *Pclo<sup>gt/gt</sup>* AZs than in wild-type (Fig 6D). We cannot rule out  
475 that an artificial aggregation of untethered Ca<sup>2+</sup> channels by the fixative or antibodies contributes to the  
476 Ca<sub>v</sub>1.3 clusters remaining as fragments and single spot-like Ca<sub>v</sub>1.3 clusters (Neef et al., 2018).

477 Similar to our observations in 2 months old rats, we saw a clear reduction in the size of the synaptic  
478 ribbon in younger *Pclo<sup>gt/gt</sup>* rats;  $57.65 \times 10^3 \pm 1.36 \times 10^3 \text{ nm}^2$ , S.D. =  $18.75 \times 10^3$ ,  $n_{\text{ribbons}} = 191$ ,  $N_{\text{animals}} = 3$  for  
479 *Pclo<sup>gt/gt</sup>* vs.  $67.81 \times 10^3 \pm 1.98 \times 10^3 \text{ nm}^2$ , S.D. =  $26.26 \times 10^3$ ,  $n_{\text{ribbons}} = 176$ ,  $N_{\text{animals}} = 3$  for *Pclo<sup>wt/wt</sup>*;  $P < 0.0001$ ,  
480 Mann-Whitney-Wilcoxon test. This difference remains significant ( $P < 0.0001$ , Mann-Whitney-Wilcoxon  
481 test) when removing the two outliers from the control data set. The area of single-line and single spot-  
482 like Ca<sub>v</sub>1.3 clusters was also estimated by fitting a 2D-Gaussian function and was found to be smaller in  
483 *Pclo<sup>gt/gt</sup>* IHCs ( $P = 0.026$  for single-line clusters,  $P = 0.028$  for single spot-like clusters and  $P = 0.027$  for all  
484 single structures; Mann-Whitney-Wilcoxon test; lines and spots pooled, represented in box plot in Fig  
485 6E). This remained significant when removing the outlier from the control group ( $P = 0.03$ , Mann-  
486 Whitney-Wilcoxon test). The areas of ribbons and Ca<sub>v</sub>1.3 clusters showed a positive correlation for both  
487 *Pclo<sup>wt/wt</sup>* and *Pclo<sup>gt/gt</sup>* ( $P_r = 0.53$ ,  $P < 0.0001$  for *Pclo<sup>wt/wt</sup>* and  $P_r = 0.44$ ,  $P < 0.0001$  for *Pclo<sup>gt/gt</sup>*, considering  
488 only synapses with single Ca<sub>v</sub>1.3 structures, Fig. 6E).



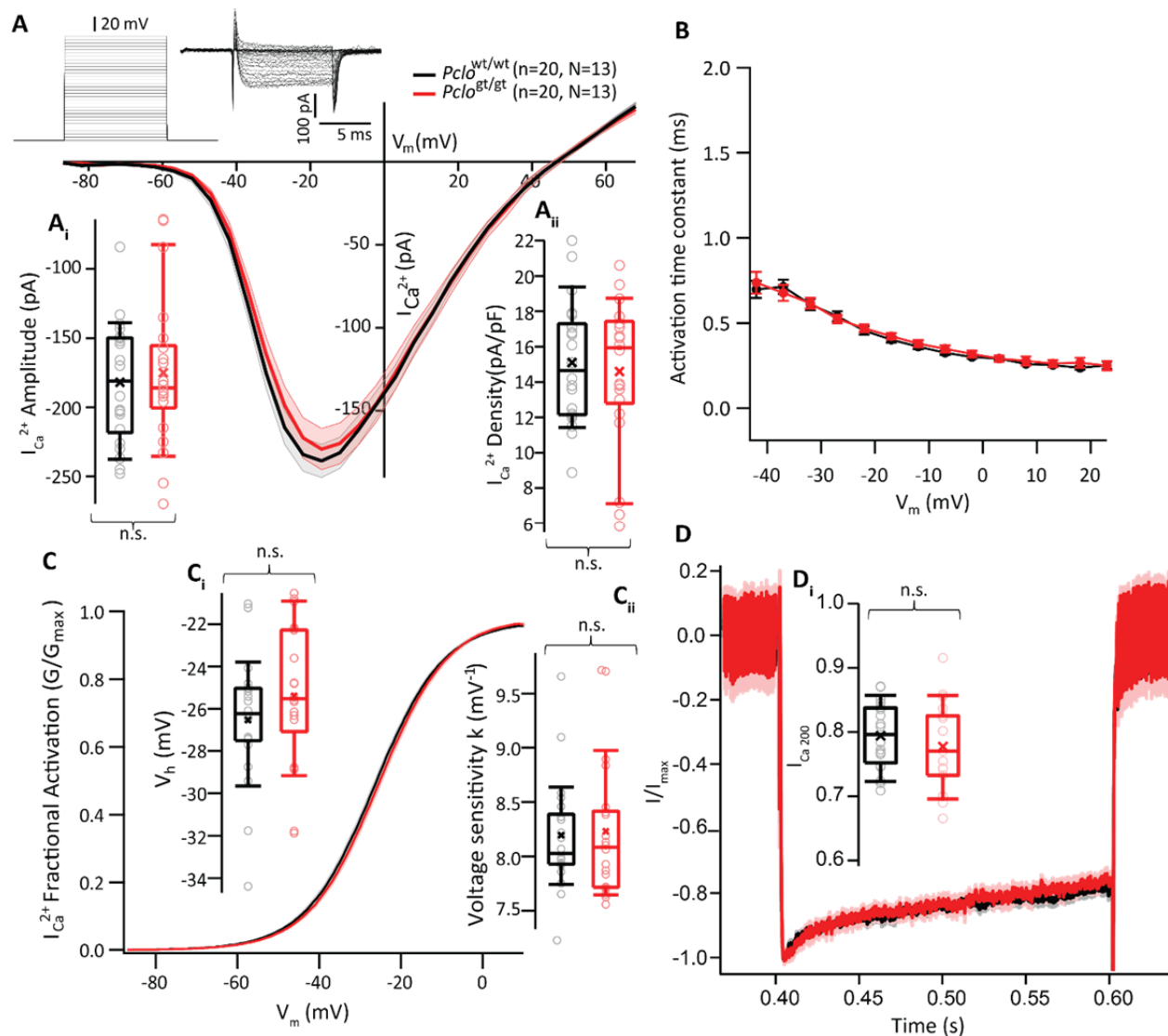
490 **Figure 6. STED imaging reveals altered morphology of Ca<sub>v</sub>1.3 channel clusters upon piccolino**  
491 **disruption**

492 **(A)** Maximum projections of confocal sections of organ of Corti from 2-3 weeks old rats, stained for the  
493 presynaptic scaffold protein bassoon (blue), CtBP2 labeling the synaptic ribbon (red) and Ca<sub>v</sub>1.3 channel  
494 clusters (green). Juxtaposition of the three proteins appears comparable. Scale bars = 5 μm. **(B)**  
495 Randomly selected synapses from the triple-labeling represented in (A) were further imaged using 2D-  
496 STED (Ca<sub>v</sub>1.3 and CtBP2) and confocal (bassoon) modes. Scale bars = 0.5 μm. Most synapses in *Pclo*<sup>wt/wt</sup>  
497 IHCs showed a single line-shaped Ca<sub>v</sub>1.3 channel cluster, while some showed spot-like clusters and  
498 double lines (top panel). On the contrary, *Pclo*<sup>gt/gt</sup> synapses additionally showed Ca<sub>v</sub>1.3 clusters in  
499 complex arrangements, with some clusters seemingly broken into several smaller spots (lower panel).  
500 **(C, D)** 176 *Pclo*<sup>wt/wt</sup> (N<sub>animals</sub> = 3) and 191 *Pclo*<sup>gt/gt</sup> (N<sub>animals</sub> = 3) were categorized based on the apparent  
501 morphology of their Ca<sub>v</sub>1.3 channel clusters into line-, double line-, spot-like and complex-clusters.  
502 *Pclo*<sup>gt/gt</sup> IHCs evidently show a higher percentage of synapses with spot-like morphology and complex  
503 clusters with multiple substructures. **(E)** The 2D areas of the synaptic ribbon and of corresponding  
504 Ca<sub>v</sub>1.3 clusters (only ones with a single structure) were estimated by fitting a 2D-Gaussian function to  
505 the STED data obtained. The ribbons in IHCs of 2-3 weeks old *Pclo*<sup>gt/gt</sup> rats appear significantly smaller (*P*  
506 < 0.0001, Mann-Whitney-Wilcoxon test), even after excluding the outliers in the *Pclo*<sup>wt/wt</sup> dataset. The  
507 area of Ca<sub>v</sub>1.3 clusters with single structures (single line/spot; 151 *Pclo*<sup>wt/wt</sup> synapses, 129 *Pclo*<sup>gt/gt</sup>  
508 synapses) also appears smaller (*P* < 0.05, Mann-Whitney-Wilcoxon test). Note the positive correlation  
509 between ribbon and size of Ca<sub>v</sub>1.3 clusters (*P*<sub>r</sub> = 0.53, *P* < 0.0001 for *Pclo*<sup>wt/wt</sup> and *P*<sub>r</sub> = 0.44, *P* < 0.0001 for  
510 *Pclo*<sup>gt/gt</sup>). Ribbon areas corresponding to clusters with multiple structures have also been plotted. Box  
511 plots depict individual data points overlaid with mean values shown as crosses.

512  
513 **Ca<sup>2+</sup> current amplitude, voltage-dependence and kinetics remain unchanged upon piccolino disruption**

514 We next investigated if piccolino disruption, in addition to altering the morphology of Ca<sup>2+</sup> channel  
515 clusters, also affects Ca<sub>v</sub>1.3 Ca<sup>2+</sup> channel physiology. We performed whole-cell perforated patch-clamp  
516 recordings of Ca<sup>2+</sup> currents from IHCs of 2-4 weeks old rats in the presence of 5 mM [Ca]<sub>e</sub> for enhanced  
517 signal to noise ratio. Step depolarizations of 20 ms from -87 to 68 mV in 5 mV step increments were  
518 applied to obtain current-voltage (IV) relations (Fig 7A). Ca<sup>2+</sup> current amplitudes in *Pclo*<sup>gt/gt</sup> IHCs (-175.48  
519 ± 12.87 pA, n<sub>IHC</sub> = 20, N<sub>animals</sub> = 13) appeared comparable to those in *Pclo*<sup>wt/wt</sup> IHCs (-182.23 ± 10.21 pA,  
520 n<sub>IHC</sub> = 20, N<sub>animals</sub> = 13; *P* = 0.67, t-test, Fig 7A, Appendix Table 5). We did not find any statistically  
521 significant changes in the voltage-dependence of Ca<sup>2+</sup> channel activation in piccolino deficient IHCs in  
522 contrast to what was observed in IHCs lacking synaptic ribbons (Jean et al., 2018) (Fig 7C). Activation and  
523 inactivation kinetics of Ca<sup>2+</sup> channels also appeared unaltered (Fig 7B, D; see figure legend for  
524 description).

525



526

527

### Figure 7. *Pclo*<sup>gt/gt</sup> IHCs show normal Ca<sup>2+</sup> currents

528 (A) Current-voltage (IV) relations from whole-cell perforated patch clamp recordings of IHCs, [Ca]<sub>e</sub> = 5  
 529 mM. Line represents mean current traces, shaded area represents ± SEM. (A<sub>i</sub>) A comparable whole-cell  
 530 Ca<sup>2+</sup> current amplitude ( $P = 0.67$ , t-test), and (A<sub>ii</sub>) current density ( $P = 0.68$ , t-test) was observed in IHCs  
 531 of 2-4 weeks old *Pclo*<sup>wt/wt</sup> ( $n_{\text{IHC}} = 13$ ,  $N_{\text{animals}} = 20$ ) *Pclo*<sup>gt/gt</sup> ( $n_{\text{IHC}} = 13$ ,  $N_{\text{animals}} = 20$ ) rats. (B) A power  
 532 exponential function was fitted on the first 5 ms of the current traces to obtain the activation time  
 533 constant (mean ± SEM) of Ca<sup>2+</sup> current at different voltages, which was unaltered. Estimation becomes  
 534 less certain below -42 mV and above 23 mV, and hence these extremes were excluded from analysis. (C)  
 535 A Boltzmann function was fitted to the current traces from (A) to derive the fractional activation of the  
 536 whole-cell Ca<sup>2+</sup> current. (C<sub>i</sub>) Voltage of half-maximal activation ( $V_h$ ) and (C<sub>ii</sub>) slope ( $k$ ) of the Boltzmann fit  
 537 do not show any statistically significant differences ( $P = 0.28$  and  $P = 0.71$  respectively, t-test). (D)  
 538 Average peak amplitude-normalised Ca<sup>2+</sup> currents in response to 200 ms depolarisations from -87 mV to  
 539 -17 mV (shaded area represents ± SEM). Residual Ca<sup>2+</sup> current (D<sub>i</sub>) show comparable inactivation in

540 piccolino deficient IHCs;  $P = 0.22$ , Mann-Whitney-Wilcoxon test ( $n_{\text{IHC}} = 18$ ,  $N_{\text{animals}} = 12$  for  $Pclo^{wt/wt}$  and  
 541  $n_{\text{IHC}} = 17$ ,  $N_{\text{animals}} = 11$  for  $Pclo^{gt/gt}$ ). Box plots show individual data points overlaid; mean values are  
 542 shown as crosses.

543

Parameter	$Pclo^{gt/gt}$			$Pclo^{wt/wt}$			P-value
	Mean $\pm$ SEM	S.D.	Sample size	Mean $\pm$ SEM	S.D.	Sample size	
$I_{Ca}^{2+}$	-175.48 $\pm$ 12.87 pA	56.08 pA	$n_{\text{IHC}} = 20$ , $N_{\text{animals}} = 13$	-182.23 $\pm$ 10.21 pA	44.51 pA	$n_{\text{IHC}} = 20$ , $N_{\text{animals}} = 13$	$P > 0.05$ (T)
$I_{Ca}^{2+}$ density	14.57 $\pm$ 0.97 pA/pF	4.22 pA/pF		15.08 $\pm$ 0.80 pA/pF	3.50 pA/pF		$P > 0.05$ (T)
$V_h$	-25.39 $\pm$ 0.78 mV	3.40 mV		-26.53 $\pm$ 0.71 mV	3.09 mV		$P > 0.05$ (T)
k	8.23 $\pm$ 0.15 $mV^{-1}$	0.66 $mV^{-1}$		8.19 $\pm$ 0.12 $mV^{-1}$	0.51 $mV^{-1}$		$P > 0.05$ (W)
$I_{Ca, 200}$	0.77 $\pm$ 0.02	0.09	$n_{\text{IHC}} = 17$ , $N_{\text{animals}} = 11$	0.79 $\pm$ 0.01	0.05	$n_{\text{IHC}} = 18$ , $N_{\text{animals}} = 12$	$P > 0.05$ (W)
$\Delta C_m$ , 20 ms	12.06 $\pm$ 2.48 fF	8.23 fF	$n_{\text{IHC}} = 12$ , $N_{\text{animals}} = 6$	12.48 $\pm$ 1.94 fF	6.13 fF	$n_{\text{IHC}} = 11$ , $N_{\text{animals}} = 8$	$P > 0.05$ (W)
$Q_{Ca}$ , 20 ms	3.21 $\pm$ 0.38 pC	1.27 pC		3.65 $\pm$ 0.27 pC	0.85 pC		$P > 0.05$ (W)
$\Delta C_m$ , 100 ms	35.38 $\pm$ 6.15 fF	20.41 fF		36.82 $\pm$ 7.07 fF	22.36 fF		$P > 0.05$ (W)
$Q_{Ca}$ , 100 ms	15.15 $\pm$ 1.80 pC	5.97 pC		17.52 $\pm$ 1.35 pC	4.27 pC		$P > 0.05$ (W)

544 **Appendix Table 5. IHC physiology**

545 Data is represented as mean  $\pm$  SEM;  $n_{\text{IHC}}$  denotes number of IHCs,  $N_{\text{animals}}$  is number of rats used.  
 546 Statistical analysis was performed using an unpaired two-sample  $t$  test (T), or using Mann-Whitney-  
 547 Wilcoxon test (W).  $I_{Ca}^{2+}$  = whole cell  $Ca^{2+}$  current,  $V_h$  = voltage of half maximal activation, k = voltage  
 548 sensitivity of activation,  $I_{Ca, 200}$  = residual  $Ca^{2+}$  current at 200 ms depolarization,  $\Delta C_m$  = change in exocytic  
 549 membrane capacitance,  $Q_{Ca}$  =  $Ca^{2+}$  current integral.

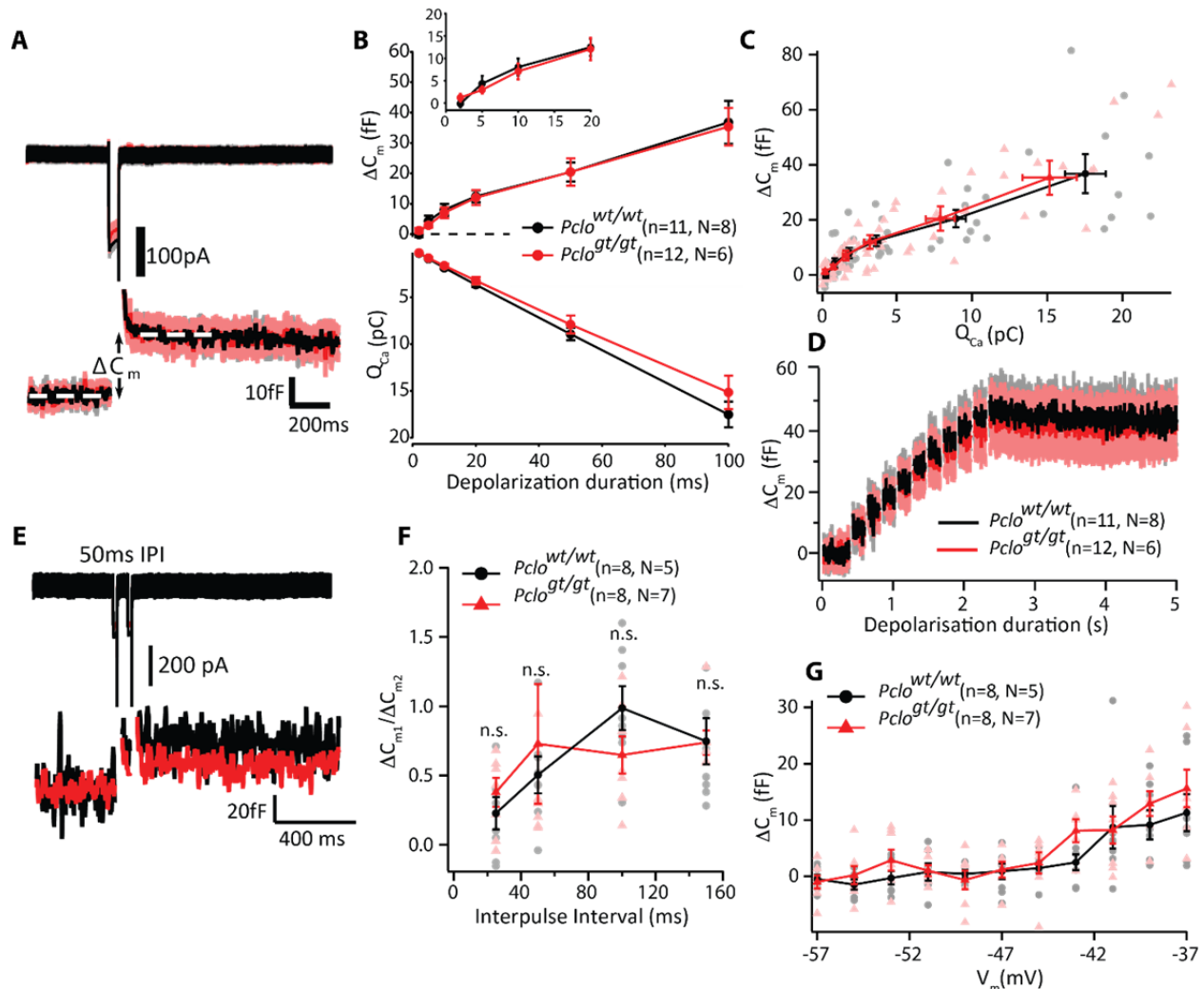
550

551

552 [SV exocytosis and replenishment are unaltered in  \$Pclo^{gt/gt}\$  IHCs](#)

553 The synaptic ribbon plays a critical role in the exocytosis of the readily releasable pool of SVs (RRP) in  
 554 retinal bipolar cells (Hull et al., 2006; Maxeiner et al., 2016; Snellman et al., 2011) and in rod  
 555 photoreceptors (Grabner and Moser, 2021). The situation is more complex for cochlear IHCs lacking

556 synaptic ribbons (ribbon-less): while the RRP was reduced in bassoon deficient IHCs (Buran et al., 2010;  
557 Khimich et al., 2005) it was normal in RIBEYE deficient IHCs (Becker et al., 2018; Jean et al., 2018). Some  
558 of this discrepancy can be attributed to additional effects of bassoon disruption e.g. on  $\text{Ca}^{2+}$  channel  
559 abundance and topography (Frank et al., 2010; Khimich et al., 2005; Neef et al., 2018) and  
560 compensatory synaptic transformations in the case of RIBEYE-deficiency (Jean et al., 2018). Here, we  
561 investigated if piccolo disruption impairs SV exocytosis and replenishment. We recorded exocytic  
562 membrane capacitance ( $\Delta C_m$ ) in response to step depolarizations (to near the potential of maximal  $\text{Ca}^{2+}$   
563 currents) using perforated patch clamp recordings in IHCs of 2-4 week old rats with 5 mM  $[\text{Ca}]_e$ .  $\Delta C_m$  in  
564 response to short and long depolarizations (recruiting the fast and sustained components of exocytosis  
565 respectively, Moser and Beutner, 2000) did not show any significant differences (Fig 8B, Appendix Table  
566 5). To estimate the SV replenishment, we applied ten consecutive trains of 10 ms depolarization pulses  
567 (Fig 8D) and also performed paired pulse recordings (Fig 8E,F) as have been described before (Jean et al.,  
568 2018; Krinner et al., 2017). Again, we did not observe alterations in *Pclo<sup>gt/gt</sup>* IHCs which seems  
569 reminiscent of what was observed in ribbon-less IHCs of RIBEYE KO mice (Becker et al., 2018; Jean et al.,  
570 2018). Next, we analyzed the voltage-dependence of  $\Delta C_m$  by stimulating IHCs with weak physiological  
571 depolarization pulses as RIBEYE KO IHCs showed a mild depolarized shift of exocytosis (Jean et al., 2018).  
572 In contrast, we do not observe any such alterations in exocytosis upon piccolo disruption (Fig 8G).  
573



574

575 **Figure 8. SV exocytosis and replenishment appear unaltered at the synapses of piccolino-deficient**  
 576 **IHCs.**

577 **(A)** Average  $\text{Ca}^{2+}$  currents (upper panel) and corresponding changes in membrane capacitance ( $\Delta C_m$ ,  
 578 lower panel) in response to 50 ms depolarisations from -87 mV to -17 mV (shaded area represents  $\pm$   
 579 SEM) from *Pclo*<sup>wt/wt</sup> IHCs ( $n_{\text{IHC}} = 11$ ,  $N_{\text{animals}} = 8$ ) and *Pclo*<sup>gt/gt</sup> IHCs ( $n_{\text{IHC}} = 12$ ,  $N_{\text{animals}} = 6$ ). **(B)** Mean  $\pm$  SEM  
 580  $\Delta C_m$  and the corresponding  $\text{Ca}^{2+}$  current integral ( $Q_{\text{Ca}}$ ) obtained in response to depolarisations of variable  
 581 durations (2 to 100 ms) to -17 mV: normal phasic ( $\leq 20$  ms) and sustained exocytosis in *Pclo*<sup>gt/gt</sup> IHCs ( $n_{\text{IHC}}$   
 582 = 12,  $N_{\text{animals}} = 6$ ) in comparison to *Pclo*<sup>wt/wt</sup> IHCs ( $n_{\text{IHC}} = 11$ ,  $N_{\text{animals}} = 8$ ). Inset shows zoom-in for the first  
 583 20 ms. **(C)**  $\Delta C_m$  vs. the corresponding  $Q_{\text{Ca}}$ : normal apparent  $\text{Ca}^{2+}$  dependence of exocytosis (Mean  $\pm$  SEM  
 584 for each pulse duration are represented as darkened points, lightly shaded points represent individual  
 585 IHCs). **(D)** Mean  $\Delta C_m$  traces (shaded area represents  $\pm$  SEM) in response to trains (10 stimuli) of 10 ms  
 586 depolarisations from -87 to -17 mV: similar responses indicate intact SV replenishment for *Pclo*<sup>gt/gt</sup> IHCs  
 587 ( $n_{\text{IHC}} = 12$ ,  $N_{\text{animals}} = 6$ ) and *Pclo*<sup>wt/wt</sup> ( $n_{\text{IHC}} = 11$ ,  $N_{\text{animals}} = 8$ ) IHCs. **(E)** Representative  $\Delta C_m$  traces in response  
 588 to pairs of 20 ms pulses separated by an inter-pulse interval (IPI) of 50 ms. **(F)** Paired-pulse ratios  
 589 ( $\Delta C_{m2}/\Delta C_{m1}$ ) at varying IPIs (25, 50, 100, and 150 ms) also indicate comparable rates of SV replenishment  
 590 for *Pclo*<sup>gt/gt</sup> ( $n_{\text{IHC}} = 8$ ,  $N_{\text{animals}} = 7$ ) and *Pclo*<sup>wt/wt</sup> ( $n_{\text{IHC}} = 8$ ,  $N_{\text{animals}} = 5$ ) IHCs. **(G)**  $\Delta C_m$  in response to 100 ms

591 depolarisations of different potentials (Mean  $\pm$  SEM and individual (lightly shaded points): no statistically  
592 significant difference, ( $n_{\text{IHC}} = 8$ ,  $N_{\text{animals}} = 5$  for  $PcLo^{wt/wt}$ ;  $n_{\text{IHC}} = 8$ ,  $N_{\text{animals}} = 7$  for  $PcLo^{gt/gt}$ ).

593

## 594 Discussion

595 In the present study we analyzed the impact of genetic disruption of piccolo, the short isoform of the  
596 multidomain protein piccolo/aczonin on the structure and function of IHC ribbon synapses. Using a  
597 multidisciplinary approach, we identified a mild synaptic hearing impairment and roles of piccolo for  
598 ribbon morphology, SV complement and  $\text{Ca}^{2+}$  organization at the IHC AZ. Intriguingly the observed  
599 subtle structural alterations seemed to affect only a subset of AZs that, however, distributed throughout  
600 the synaptic IHC pole regardless of position along the modiolar-pillar axis. Moreover, we failed to detect  
601 alterations of presynaptic function at least on the whole IHC level which contrasts with a mild sound  
602 encoding deficit observed on the systems level. Together our results indicate that piccolo is required  
603 for normal structure and function of IHC synapses.

### 604 Mild functional and structural impairment upon piccolo disruption

605 Genetic disruption of piccolo in rats (10-weeks-old  $PcLo^{gt/gt}$ ) resulted in a mild hearing deficit with  
606 elevated ABR thresholds for middle and high frequency tone bursts and a significant reduction of the  
607 amplitude of the first ABR wave reflecting an impairment in synchronous firing of SGNs. Previous studies  
608 in piccolo KO mice (Mukherjee et al., 2010) reported normal sound thresholds and a reduced wave II  
609 amplitude (Butola et al., 2017). In these mutants, the piccolo splice variant was not affected (Butola et  
610 al., 2017), thus normal sound encoding on the level of ribbon synapses was expected, given that  
611 piccolo is the only isoform present at ribbon synapses (Regus-Leidig et al., 2013). Recently, Li and co-  
612 workers reported findings in mice with complete loss of piccolo and piccolo demonstrating functional  
613 impairments of the retina while hearing seemed unaffected with normal ARBs up to 8 months of age (Li



614 et al., 2021). Our findings on piccolino gene-trap rats contrast the normal hearing in KO mice for which  
615 we currently do not have an explanation.

616 Moreover, using STED and electron microscopy, we observed several alterations of ribbon synapse  
617 morphology in cochlear IHCs of *Pclo<sup>gt/gt</sup>* rats. A fraction of the Ca<sub>v</sub>1.3 Ca<sup>2+</sup> channel clusters appeared  
618 fragmented into smaller patches. Furthermore, focusing on single spot-like and single line-shaped Ca<sub>v</sub>1.3  
619 Ca<sup>2+</sup> channel clusters we found them to be smaller, as were synaptic ribbons, while PSDs were enlarged.  
620 Electron microscopy uncovered two morphologically distinct AZ categories at mutant synapses: category  
621 1 closely resembled control AZ, while ribbons of category 2 AZs were strikingly smaller and completely  
622 lacked SVs at the membrane-distal part of the ribbon. To our surprise, these structural alterations were  
623 not accompanied by functional changes on the whole IHC level: Ca<sup>2+</sup> currents and exocytosis of *Pclo<sup>gt/gt</sup>*  
624 IHCs were comparable to the controls. It will be interesting in future studies to study synaptic function  
625 at the level of single synapses in order to test the hypothesis that postulated functional deficits of  
626 category 2 AZs were masked by category 1 AZs. Indeed, category 1 AZs were found to be even larger  
627 compared to littermate controls with an elevated number of SVs. Together, the presence of both,  
628 enlarged category 1 AZs and the small category 2 AZs, yielded normal Ca<sup>2+</sup> currents and exocytic  
629 function at the whole IHC level. Further, the enlarged PSDs, which we observed in the *Pclo<sup>gt/gt</sup>* rats might  
630 contribute to compensate for presynaptic structural deficits. Such enlarged PSDs were previously  
631 observed in piccolo and bassoon mutants in conventional synapses (Mukherjee et al., 2010). *Ex vivo*  
632 patch-clamp recordings from IHCs of higher frequency places of the cochlea as well as *in vivo* recordings  
633 of single SGNs in future studies might help to further elucidate the relationship of exocytosis, which  
634 could differ in its dependence on piccolino along the tonotopic axis, and neural sound encoding.

### 635 [A role of piccolino as a structural determinant for ribbon synapses](#)

636 Previously, it was shown for several species that morphological and functional attributes of IHC ribbon  
637 synapses display a spatial gradient along the modiolar (or neural) – pillar (or abneural) axis. IHC AZs vary

638 in ribbon size (Kantardzhieva et al., 2013; Liberman, 1980; Meyer et al., 2009; Michanski et al., 2019;  
639 Ohn et al., 2016; Payne et al., 2021), number, voltage-dependence of activation and coupling of SVs to  
640  $\text{Ca}^{2+}$  channels (Frank et al., 2009; Ohn et al., 2016; Özçete and Moser, 2021). Such synaptic diversity  
641 offers an exciting candidate mechanism for how IHCs might decompose the full range of sound intensity  
642 information into complementary neural codes in SGNs that have long been known to differ in  
643 spontaneous and sound-evoked firing (Moser et al., 2019; Rutherford and Moser, 2016). Classically SGNs  
644 have been categorized into three functional subtypes: low, medium, and high spontaneous rate (SR)  
645 SGNs (Kiang et al., 1965; Liberman, 1978; Sachs and Abbas, 1974; Taberner and Liberman, 2005; Winter  
646 et al., 1990). Recently, analysis of molecular SGN profiles has led to the identification of three molecular  
647 SGN subtypes type 1a-c which were suggested to relate to the functional SGN subtypes (Li et al., 2020;  
648 Petitpré et al., 2018; Shrestha et al., 2018; Sun et al., 2018) and might also instruct properties of the  
649 corresponding presynaptic IHC AZ (Sherrill et al., 2019). Last but not least, differences in efferent  
650 innervation of the peripheral SGNs neurites (e.g. Hua et al., 2021; Liberman et al., 1990) might  
651 contribute to the synaptic and neurophysiological differences of SGNs (Ruel et al., 2001; Yin et al., 2014).  
652 How the various mechanisms interplay to the collective sound encoding of SGNs has yet to be  
653 elucidated. Specifically, how IHCs diversify their AZs remains an exciting research question. Specifically,  
654 identifying molecular pathways and determinants setting the specific structure and function is a key  
655 task.

656 The present finding of two categories of presynaptic AZs in *Pclo<sup>gt/gt</sup>* IHCs despite the given  
657 overall AZ variance provides an interesting insight into how individual AZ proteins can determine  
658 structure. A structural role of piccolino at ribbon synapses was previously demonstrated in the retina  
659 (Regus-Leidig et al., 2014). It is conceivable that its interaction with RIBEYE plays an important role in  
660 maintaining synapse architecture (Müller et al., 2019). Already the reduction of piccolino resulted in  
661 structural changes of plate-like photoreceptor ribbons to smaller, more oval shaped ones (Regus-Leidig

662 et al., 2014). Müller et al. discussed the option that RIBEYE together with piccolo organizes the plate-  
663 like structure of the synaptic ribbon in the retina, specifically for rod photoreceptors and rod bipolar  
664 cells. Since IHC ribbon synapses are more oval in their shape, the authors suggested that probably a  
665 different RIBEYE-piccolino ratio might exist at IHC ribbon synapses, which would result in their oval  
666 structure (Müller et al., 2019). Grading piccolo abundance across the AZs of individual IHCs might  
667 likewise contribute to different morphologies of their ribbons. However, whether different ratios of  
668 piccolo/RIBEYE prevail at the AZs of individual IHCs remains to be investigated in future experiments.  
669 The present findings on piccolo deficient IHCs did not point to preferred position along the modiolar-  
670 pillar axis of the AZ categories, which would not seem to support a major role of piccolo in shaping  
671 synaptic heterogeneity in IHCs. We speculate that the ribbon of category 2 AZ found upon disrupting  
672 piccolo might represent a sort of basic IHC ribbon version, which is then modulated by the amount of  
673 piccolo, while category 1 might reflect a compensatory potential specific to a subset of synapses.  
674 Addressing functional differences between the AZ categories in *Pclo<sup>gt/gt</sup>* IHCs will require future single  
675 synapse analysis (Goutman and Glowatzki, 2007; Özçete and Moser, 2021).

#### 676 [Normal synaptic vesicle tethering at piccolo-deficient AZs](#)

677 Piccolino was shown to bind to RIBEYE, while its N-terminus faces the cytoplasm and was suggested to  
678 regulate steps in the SV cycle by binding to other presynaptic proteins (Müller et al., 2019). In line with  
679 previous studies for photoreceptor ribbon synapses (Limbach et al., 2011; Müller et al., 2019), our  
680 immunogold labelings of rodent ribbon synapses confirmed that piccolo localizes to synaptic ribbons  
681 of IHCs (the present study, (Michanski et al., 2019)). Moreover, ribbons of *Pclo<sup>gt/gt</sup>* category 2 AZs were  
682 void of membrane distal SVs, which could point either to a role of piccolo in SV tethering or in enabling  
683 a tethering-relevant ribbon part. Importantly, normal ribbon-tether number of those remaining RA-SVs  
684 at category 2 AZs argue against an essential role of piccolo in tethering SVs to the ribbon. Nonetheless,  
685 the increased distance of SVs to the ribbon surface of AZs could indicate a contribution of piccolo in

686 attracting SVs. Moreover, a previous study has shown that a 110 kDa piccolino fragment is still  
687 detectable in *Pclo<sup>gt/gt</sup>* rat retina (Müller et al., 2019), which could exert some residual function. For  
688 example, the interaction site for the actin/dynamin-binding protein Abp1 is likely still present in the  
689 *Pclo<sup>gt/gt</sup>* mutant rats, while the RIBEYE interaction site, which is located in the C-term region of piccolino,  
690 is eliminated (Müller et al., 2019). Fenster et al. showed the interaction between piccolo and Abp1,  
691 which also binds to both F-actin and the GTPase dynamin. This led to the hypothesis that piccolo  
692 localizes Abp1 to AZs to create a functional connection between the dynamic actin cytoskeleton and SV  
693 recycling at conventional synapses (Fenster et al., 2003), the relevance of which for ribbon synapses  
694 remains to be tested.

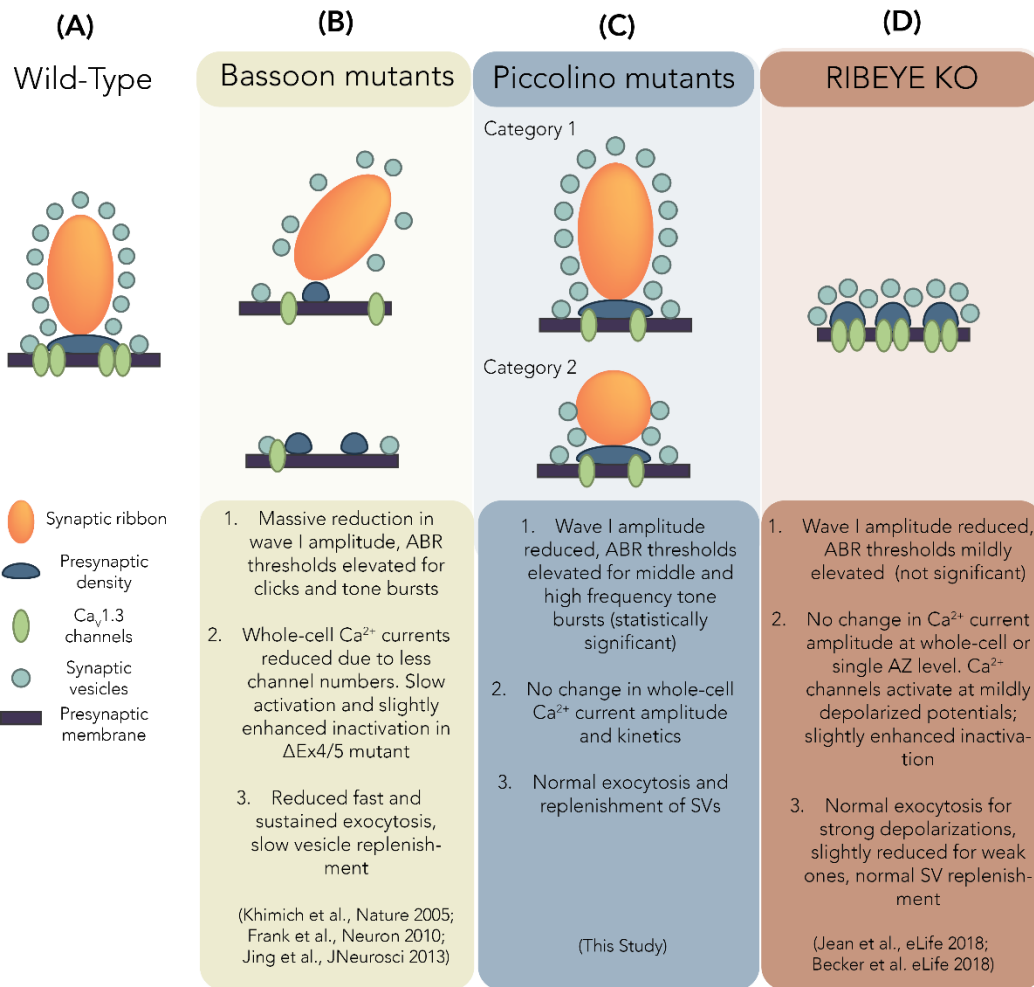
#### 695 [Key molecular organizers of the ribbon-type AZs in IHCs](#)

696 Bassoon and piccolo are important scaffold proteins at AZs with partially overlapping functions (review  
697 in Gundelfinger et al., 2015). Disruption of piccolo resulted in normal sized AZs but fewer SVs in AZs of  
698 endbulb of Held synapses (Butola et al., 2017). In AZs of rat IHCs, the disruption of piccolino had several  
699 structural consequences (Fig 9). Mutant AZs showed only single ribbons and generally fewer MP-SVs.  
700 Moreover, a subset of AZs with smaller ribbons was found, which lack SVs at their membrane distal side.  
701 The Ca<sup>2+</sup> channel clusters appeared fragmented, resembling what has been shown for IHC AZs in RIBEYE  
702 mutants (Jean et al., 2018). Altered localization and reduced number of Ca<sup>2+</sup> channels were previously  
703 reported for RIM2 (Jung et al., 2015a) and RIM-BP2 (Krunner et al., 2017) deficient IHC AZs. RIM2 and  
704 RIM-BP2 positively regulate the number of synaptic Ca<sub>v</sub>1.3 channels at IHC AZs and promote fast SV  
705 recruitment to the RRP. Loss of the ribbon due to disruption of RIBEYE resulted in subtle functional  
706 impairments in IHCs and hearing (Fig 9) (Becker et al., 2018; Jean et al., 2018), while in rod  
707 photoreceptors RIBEYE disruption dwarfed the RRP to a third (Grabner and Moser, 2021). Maintained  
708 presynaptic IHC function in ribbonless IHCs was attributed to partial compensation that encompasses  
709 several small bassoon-positive presynaptic densities at ribbon-less AZs tethering a large number of SVs

710 (Jean et al., 2018). This raised the question if ribbons are dispensable for the function of IHC AZs as long  
711 as bassoon remains present. Piccolino lacks the interactions site to bassoon (Regus-Leidig et al., 2013),  
712 and different from conventional synapses, piccolino and bassoon segregate at ribbon-type AZs (Dick et  
713 al., 2001; Khimich et al., 2005; Limbach et al., 2011; Michanski et al., 2019; tom Dieck et al., 1998; Wong  
714 et al., 2014). In contrast to the mild sensory coding phenotypes of piccolino mutants (the present study,  
715 (Li et al., 2021; Müller et al., 2019)), disruption of bassoon strongly alters transmission at afferent  
716 synapses of retina and cochlea (Fig 9). The deletion of exon 4 and 5 ( $Bsn^{\Delta Ex4/5}$ ) resulted in detached  
717 synaptic ribbons in photoreceptors and IHCs and impaired sensory coding assayed at the systems and  
718 synaptic levels (Dick et al., 2003; Khimich et al., 2005). In addition, to the reduced RRP,  $Bsn^{\Delta Ex4/5}$  IHC AZs  
719 showed fewer and mislocalized  $Ca^{2+}$  channels (Frank et al., 2010; Khimich et al., 2005; Neef et al., 2018).  
720 It has remained challenging to disentangle effects of ribbon-loss and overall AZ alterations upon bassoon  
721 disruption (Frank et al., 2010; Jing et al., 2013), in particular given the mild functional deficits in ribbon-  
722 less IHCs of RIBEYE KOs (Becker et al., 2018; Jean et al., 2018). We suggest that bassoon - as the major  
723 component of the presynaptic density (Wong et al., 2014) - is the main organizer at IHC ribbon synapse  
724 AZs and might even be able to tether SVs to the presynaptic density. Piccolino and RIBEYE likely jointly  
725 determine ribbon shape and size and might thus finetune exocytosis at IHC ribbon synapses.

726

727



728

729 **Figure 9: Summary of key structural and functional observations at IHC AZs upon genetic perturbation**  
 730 **of bassoon, piccolo and RIBEYE. (A)** Wild-type IHC synaptic ribbons drawn for reference; these are  
 731 typically ellipsoid shaped and anchored to the presynaptic membrane via the presynaptic density. **(B)**  
 732 Disruption of bassoon causes ribbon anchorage defects, resulting in ribbon-less AZs (lower panel,  
 733 representing partial deletion ΔEx4/5 mutants) or loosely anchored ribbons (top panel, representing the  
 734 predominant form in bassoon gene-trap mutants). **(C)** Disruption of piccolo results in two categories of  
 735 AZs: category 1 wild-type-like ribbons and roundish, small ribbons for category 2 AZs that lack SVs at  
 736 their membrane-distal apex. **(D)** RIBEYE deficient IHCs show ribbon-less AZs with multiple smaller  
 737 presynaptic densities and SV assemblies feeding into the same postsynapse. Ca<sup>2+</sup> channel clusters  
 738 appear smaller and fragmented in IHCs of bassoon, piccolo and RIBEYE mutants.

739

## 740 Material and Methods

### 741 Animals

742 We used a piccolo gene trap (*Pclo<sup>gt/gt</sup>*) rat strain, which is described in detail in (Medrano et al., 2020).  
743 Briefly, transposon mutagenesis resulted in the integration of a transposon element into exon 3 of the  
744 *PCLO* gene, leading to a stop in the reading frame. *Pclo<sup>gt/gt</sup>* rats and wild-type littermate controls  
745 (*Pclo<sup>wt/wt</sup>*), from heterozygous breeding of either sex between 2 weeks and 11 months, were deeply  
746 anesthetized with CO<sub>2</sub> and sacrificed by decapitation for immediate dissection of the cochleae. All  
747 experiments complied with national animal care guidelines and were approved by the University of  
748 Göttingen Board for Animal Welfare and the Animal Welfare Office of the State of Lower Saxony.

749

### 750 Systems physiology

751 ABR and DPOAE were performed for 2-months old rats as described before (Jing et al., 2013; Strenzke et  
752 al., 2016). Animals were anesthetized intraperitoneally with a combination of ketamine (125 mg/kg) and  
753 xylazine (2.5 mg/kg), and the heart rate was constantly monitored to control the depth of anesthesia.  
754 The core temperature was maintained constant at 37°C using a rectal temperature-controlled heat  
755 blanket (Hugo Sachs Elektronik–Harvard Apparatus). For stimulus generation, presentation, and data  
756 acquisition, we used the TDT III Systems (Tucker Davis Technologies) run by BioSig32 software (Tucker  
757 Davis Technologies). Sound pressure levels (SPL) are provided in decibels SPL root mean square (RMS)  
758 (tonal stimuli) or decibels SPL peak equivalent (clicks) and were calibrated using a ¼ inch Brüel and Kjær  
759 microphone (model 4939). Tone bursts (4/8/12/16/24/32 kHz, 10 ms plateau, 1 ms cos<sup>2</sup> rise/fall) or  
760 clicks of 0.03 ms were presented at 20 Hz in the free field ipsilaterally using a JBL 2402 speaker. The  
761 difference potential between vertex and mastoid subdermal needles was amplified (50,000 times),  
762 filtered (low pass, 4 kHz; high pass, 100 Hz) and sampled at a rate of 50 kHz for 20 ms, 2 × 2000 times to

763 obtain two mean ABRs for each sound intensity. Hearing threshold was determined with 10 dB precision  
764 as the lowest stimulus intensity that evoked a reproducible response waveform in both traces by visual  
765 inspection. For DPOAEs, a 24-bit sound card and the MF1 speaker system (Tucker David Technologies)  
766 were used to generate two primary tones ( $f_2/f_1$  ratio: 1.2). Primary tones were coupled into the ear  
767 canal by a custom-made probe containing an MKE-2 microphone (Sennheiser) and adjusted to an  
768 intensity of 60 dB sound pressure level at the position of the ear drum as mimicked in a mouse ear  
769 coupler. The microphone signal was amplified (DMX6Fire; Terratec) and analyzed by fast Fourier  
770 transformation using custom software (Matlab, mathworks).

771

## 772 [Immunohistochemistry and Imaging](#)

773 Cochleae from 2-3 weeks old (postnatal day P14 - P27) and 2 months old rats were dissected in ice-cold  
774 HEPES Hank's solution containing (in mM): 5.26 KCl, 141.7 NaCl, 0.5  $MgSO_4 \cdot 7H_2O$ , 10 HEPES, 1  $MgCl_2$ ,  
775 11.1 D-glucose and 3.42 L-glutamine, pH adjusted to around 7.2, osmolality  $\sim 300$  mOsm/kg. Fixation was  
776 performed by perfusing the cochleae with 4% formaldehyde (in PBS) for 60 min on ice, while for staining  
777  $Ca^{2+}$  channel clusters, a shorter fixation of 5-10 min was performed. For cochleae from 2 months old  
778 rats, decalcification was additionally performed using Morse's solution (10% sodium citrate, 22.5%  
779 formic acid) for 15-20 min. The organ of Corti was dissected and washed three times in PBS at room  
780 temperature. Blocking and permeabilisation of the tissue was performed with GSDB (goat serum dilution  
781 buffer: 16% normal goat serum, 450 mM NaCl, 0.3% Triton X100, 20 mM phosphate buffer, pH  $\sim 7.4$ ) for  
782 1 h at room temperature. Samples were then incubated with primary antibodies (diluted in GSDB, refer  
783 to table 1) overnight at 4°C and were washed three times for 10 min in wash buffer (450 mM NaCl, 0.3%  
784 Triton X 100, 20 mM phosphate buffer, pH  $\sim 7.4$ ). This was followed by incubation with respective  
785 secondary antibodies (diluted in GSDB, refer to table 1) for 1 h in a light-protected wet chamber. Finally,



786 the samples were washed three times for 10 min in wash buffer and in 5 mM phosphate buffer for 5  
 787 min, before mounting onto glass slides with a drop of fluorescence mounting medium (*Mowiol* 4-88,  
 788 Carl Roth) and covered with thin glass coverslips. Images were acquired in confocal/STED mode using an  
 789 Olympus IX83 inverted microscope combined with an Abberior Instruments Expert Line STED  
 790 microscope (Abberior Instruments GmbH). We employed lasers at 488, 561, and 633 nm for excitation  
 791 and a 775 nm (1.2W) laser for stimulated emission depletion. 1.4 NA 100X or 20X oil immersion  
 792 objectives were used. Confocal stacks were acquired using *Imspector* Software (pixel size = 80 X 80 nm  
 793 along xy, 200 nm along z). For 2D-STED images, a pixel size of 15 X 15 nm (in xy) was used. The acquired  
 794 images were z-projected with NIH ImageJ software and adjusted for brightness and contrast. Organs of  
 795 Corti from both *Pclo<sup>wt/wt</sup>* and *Pclo<sup>gt/gt</sup>* were always processed in parallel using identical staining protocols,  
 796 laser excitation powers and microscope settings.

797 **Table 1:** List of antibodies:

Antibody	Host specie	Company	Dilution	Identifier
Anti-parvalbumin	Guinea pig (polyclonal)	Synaptic Systems	1:200	195 004
Anti-CtBP2	Mouse (monoclonal IgG1)	BD Biosciences	1:200	612044
Anti-piccolo	Rabbit (polyclonal)	Synaptic Systems	1:200	142 113
Anti-bassoon	Chicken (polyclonal)	Synaptic Systems	1:200	141 016
Anti-homer1	Rabbit (polyclonal)	Synaptic Systems	1:200	160 002
Anti-Ca <sub>v</sub> 1.3 (CACNA1D)	Rabbit (polyclonal)	Alomone Labs	1:100	ACC 005
Alexa Fluor 488 conjugated anti-guinea pig	Goat (polyclonal)	Invitrogen	1:200	A11073
Alexa Fluor 568 conjugated anti-rabbit	Goat (polyclonal)	Thermo Fisher	1:200	A11011
STAR635p conjugated anti-mouse	Goat (polyclonal)	Abberior	1:200	2-0002-007-5
Alexa Fluor 488 conjugated anti-rabbit	Goat (polyclonal)	Invitrogen (MoBiTec)	1:200	A11008
Alexa Fluor 568 conjugated anti-chicken	Goat (polyclonal)	Abcam	1:200	Ab175711
Alexa Fluor 488 conjugated anti-chicken	Goat (polyclonal)	Invitrogen	1:200	A11039
STAR580 conjugated anti-	Goat (polyclonal)	Abberior	1:200	2-0002-005-1

mouse				
STAR635p conjugated anti-rabbit	Goat (polyclonal)	Abberior	1:200	2-0012-007-2

798

799 [Focused ion beam-scanning electron microscopy \(FIB-SEM\)](#)

800 Enhanced en bloc staining for FIB-SEM samples of 2 *Pclo*<sup>wt/wt</sup> and 2 *Pclo*<sup>gt/gt</sup> rats was performed according  
801 to Deerinck et al. (Deerinck et al., 2018) and to our previous studies (Jean et al., 2020; Michanski et al.,  
802 2019). Organs of Corti, within the apical turn of the cochlea from 2-3 months old rats, were isolated in  
803 ice-cold HEPES Hank's solution (5.36 mM KCl (746436, Sigma-Aldrich, Germany), 141.7 mM NaCl  
804 (746398, Sigma-Aldrich, Germany), 10 mM HEPES (H3375, 006K5424, Sigma-Aldrich, Germany), 0.5 mM  
805 MgSO<sub>4</sub>-7H<sub>2</sub>O (Sigma-Aldrich, Germany), 1 mM MgCl<sub>2</sub> (M2670, Sigma-Aldrich, Germany), 2 mg/ml D-  
806 glucose (G8270-1KG, Sigma-Aldrich, Germany), 0.5 mg/ml L-glutamine (G3126-100G, #SLBS8600, Sigma-  
807 Aldrich, Germany) and was adjusted to pH 7.2, ~300 mmol/kg). After the dissection, organs were  
808 immediately fixed with 4% paraformaldehyde (0335.1, Carl Roth, Germany) and 0.5% glutaraldehyde  
809 (G7651, Sigma-Aldrich, Germany) in PBS (P4417, Sigma-Aldrich, Germany; pH 7.4) for 1 h on ice followed  
810 by a second fixation step overnight with 2% glutaraldehyde in 0.1 M sodium cacodylate buffer (v/v, pH  
811 7.2) at 4°C. The next day, fixed tissues were treated with a 1.5% potassium ferrocyanide (25154-10,  
812 EMS) and 4% osmium tetroxide solution (75632.5ml, Sigma-Aldrich, Germany; v/v in 0.1 M sodium  
813 cacodylate buffer) for 1 h on ice. Specimens were then briefly washed 5 times in distilled water and  
814 placed in a thiocarbohydrazide (w/v in distilled water) solution for 20 min followed by additional 5 brief  
815 washing steps in distilled water at room temperature (RT). Next, a second incubation into 2% osmium  
816 tetroxide (v/v in 0.1 M sodium cacodylate buffer) for 2 h at RT followed with subsequent 5 brief washing  
817 steps in distilled water before the samples were placed in 2.5% uranyl acetate (v/v in distilled water)  
818 overnight at RT and in darkness. The following day, samples were briefly washed 5 times in distilled  
819 water at RT and contrasted with Reynold's lead citrate (Reynolds, 1963) for 30 min at 60°C to be

820 subsequently washed once again in distilled water, dehydrated in increasing ethanol concentrations  
821 (30%, 50%, 70%, 95% and 100%), infiltrated and finally embedded in Durcupan (25%, 50%, 75%  
822 Durcupan in Acetone for 1 h each and 100% Durcupan overnight at RT and for another 2 h with fresh  
823 100% Durcupan on the following day; 44610, Sigma-Aldrich, Germany) to get polymerized for at least 48  
824 h at 60°C. The cured blocks were then trimmed with a 90° diamond trimming knife (Diatome AG, Biel,  
825 Switzerland), attached to SEM stubs (Science Services GmbH, Pin 12.7 mm x 3.1 mm) using a silver filled  
826 epoxy (Epoxy Conductive Adhesive, EPO-TEK EE 129-4; EMS) and polymerized at 60° overnight.  
827 Afterwards, samples on SEM stubs were coated with a 10 or 15 nm platinum or gold layer using the  
828 sputter coating machine EM ACE600 (Leica Microsystems) at 30 mA current to be finally placed into the  
829 Crossbeam 540 FIB-SEM (Carl Zeiss Microscopy GmbH) and positioned at 54°. A 400 or 500 nm carbon or  
830 platinum layer was deposited on top of the regions of interest and the Atlas 3D (Atlas 5.1, Fibics,  
831 Canada) software was used to collect the acquired image dataset. Specimens were exposed to the ion  
832 beam driven with a 30 nA current while a 7 or 15 nA current was applied to polish the surface. Images  
833 were acquired at 1.5 kV (1000 pA) using the ESB detector (450 V ESB grid, pixel size x/y 3 or 5 nm) in a  
834 continuous mill and acquire mode using 700 pA or 1.5 nA for the milling aperture (z-step 5 or 10 nm).  
835 For subsequent post processing, data were aligned using the Plugin “Linear Stack Alignment with SIFT”,  
836 inverted and cropped in Fiji. Depending on the dataset properties, a Gaussian blur, local contrast  
837 enhancement using a CLAHE plugin in Fiji, and a binning by 2 in x/y was applied (Schindelin et al., 2012).

838

### 839 [High-pressure freezing \(HPF\) and Freeze-substitution \(FS\)](#)

840 High-pressure freezing was essentially performed as described previously (Chapochnikov et al., 2014;  
841 Jung et al., 2015a). In brief, the apical turn cochlear organs from 1-2 months old *Pclo<sup>wt/wt</sup>* and *Pclo<sup>gt/gt</sup>*  
842 rats were dissected in ice-cold HEPES Hank’s solution and mounted onto type A specimen carriers (Leica  
843 Microsystems, Wetzlar, Germany; 3 mm in diameter and 0.2 mm in depth). The 1-hexadecene (Sigma-

844 Aldrich, Germany) coated flat side of the type B carriers (Leica Microsystems, Wetzlar, Germany; 3 mm  
845 in diameter and 0.1 mm in depth) was then placed onto the sample containing type A carrier. The  
846 assembled carriers were loaded into the middle plates of the high-pressure freezing sample holder and  
847 excess liquid was removed with filter paper. Afterwards, the sample holder was assembled and loaded  
848 into the HPM100 (Leica Microsystems, Wetzlar, Germany) to cryofix the tissues and store them in liquid  
849 nitrogen until further processing. Subsequently, the high-pressure frozen samples were freeze-  
850 substituted using the EM AFS2 (Leica Microsystems, Wetzlar, Germany) machine. In brief, organs were  
851 incubated in 0.1% (w/v) tannic acid in acetone at -90°C for 4 days followed by 3 washing steps in  
852 acetone at -90°C for 1 h, respectively. Next, 2% (w/v) osmium tetroxide in acetone was applied and  
853 incubated at -90°C for 7 h. During the following 33.4 h the temperature gradually rose up to 4°C and  
854 osmium tetroxide in acetone was removed, samples were washed in acetone 3 times (1 h each) and  
855 brought to RT. Finally, samples were infiltrated and embedded in epoxy resin (Agar-100 kit, Plano,  
856 Germany; epoxy/acetone 1:1 3-6 h; 100% epoxy resin overnight and 3-6 h on the next day) to get  
857 polymerized for at least 48 h at 70°C.

858

### 859 [Conventional embedding](#)

860 Cochlea organs from 3 months old *Pclo<sup>wt/wt</sup>* and *Pclo<sup>gt/gt</sup>* rats (one animal each) were dissected as  
861 described above. Subsequently, organs were fixed immediately after dissection with 4%  
862 paraformaldehyde (0335.1, Carl Roth, Germany) and 0.5% glutaraldehyde (G7651, Sigma, Germany) in  
863 PBS (P4417, Sigma, Germany; pH 7.4) for 1 h on ice followed by a second fixation step overnight with 2%  
864 glutaraldehyde in 0.1 M sodium cacodylate buffer (v/v, pH 7.2) at 4°C. Next, specimens were washed in  
865 0.1 M sodium cacodylate buffer and treated with 1% osmium tetroxide (75632.5ml, Sigma, Germany;  
866 v/v in 0.1 M sodium cacodylate buffer) for 1 h on ice followed by further sodium cacodylate buffer and  
867 distilled water washing steps. After the *en bloc* staining with 1% uranyl acetate (8473, Merck, Germany;

868 v/v in distilled water) for 1 h on ice, samples were briefly washed in distilled water, dehydrated in an  
869 ascending concentration series of ethanol (30%, 50%, 70%, 95% and 100%), infiltrated and embedded in  
870 epoxy resin (R1140, AGAR-100, Plano, Germany) to get finally polymerized for at least 48 h at 70°C.

871

#### 872 [Immunogold pre-embedding](#)

873 The Triton X immunogold pre-embedding protocol was applied according to our previous study  
874 (Michanski et al., 2019). In brief, cochlea organs from 10-11 months old *Pclo<sup>wt/wt</sup>* and *Pclo<sup>wt/gt</sup>* rats  
875 ( $N_{\text{animals}} = 2$  for each genotype) were dissected as mentioned above and fixed with 2% paraformaldehyde  
876 and 0.06% glutaraldehyde in PEM (0.1 M PIPES: P1851-500g, Sigma, Germany; 2 mM EGTA: E3889,  
877 Sigma, Germany; 1 mM  $\text{MgSO}_4 \times 7 \text{H}_2\text{O}$ , v/v) for 90 min on ice. Afterwards, samples were washed in PEM  
878 and blocked for 1 h in 2% bovine serum albumin (BSA; 900099, Aurion)/ 3% normal horse serum (NHS;  
879 VEC-S-200, Biozol, Germany) in 0.02% PBST (0.02% Triton X-100 (X100-500ml, Sigma, Germany) diluted  
880 in PBS, v/v). Next, samples were incubated with the anti-rabbit piccolo primary antibody (polyclonal,  
881 Synaptic Systems: 142113; 1:200 diluted in 0.02% PBST), detecting the long and the short (piccolino)  
882 isoform of piccolo for 1 h at RT and overnight at 4°C. Subsequently, specimens were washed with 0.02%  
883 PBST and incubated for 2 h with the 1.4 nm gold-coupled anti-rabbit secondary antibody (Nanogold-  
884 anti-rabbit, Nanoprobes; 1:30 diluted in 0.02% PBST) followed by another washing step in 0.02% PBST  
885 for 30 min and overnight at 4°C. Next day, after further washing steps in 0.02% PBST, samples were  
886 post-fixed with 2% glutaraldehyde in PBS (v/v) for 30 min and briefly washed in distilled water. For silver  
887 enhancement, the HQ Silver-enhancement kit (Nanoprobes) was used for 3 min in the dark and  
888 specimens were briefly washed four times. Further fixation was obtained by the treatment with 2%  
889 osmium tetroxide (v/v in 0.1 M cacodylate buffer) for 30 min followed by one washing step in distilled  
890 water for 1 h and two washing steps in distilled water for 30 min, respectively. Finally, samples were  
891 dehydrated in an ascending concentration series of ethanol (30%, 50%, 70%, 95% and 100%), infiltrated

892 and embedded in epoxy resin (R1140, AGAR-100, Plano, Germany) and polymerized for at least 48 h at  
893 70°C.

#### 894 Ultrathin-sectioning and post-staining

895 The polymerized blocks were trimmed into a pyramidal shape to remove excess resin and 70 nm  
896 ultrathin sections were cut with a 35° diamond knife (Diatome AG, Biel, Switzerland) using an EM UC7  
897 (Leica Microsystems, Wetzlar, Germany) ultramicrotome in order to check for the correct region as well  
898 as the structural preservation. Ultrathin sections were collected on 1% formvar-coated copper slot  
899 grids (Athene, 3.05 mm diameter, 1 x 2 mm; G2500C, Plano). For electron tomography, 250 nm semi-  
900 thin sections were obtained and collected on 1% formvar-coated mesh grids (100 mesh; Athene, 3.05  
901 mm diameter; G2410C, Plano). For both sectioning techniques, post-staining was performed using  
902 UranylLess (22409, EMS, Hatfield, PA) for 20 min followed by several brief washing steps with distilled  
903 water.

904

#### 905 Transmission electron microscopy and electron tomography

906 For conventional embedded samples, immunogold pre-embedded samples and to first check for the  
907 quality of the cryo-fixed tissues and the region of interest, 2D electron micrographs were taken from  
908 70 nm ultrathin sections at 80 kV using a JEM1011 transmission electron microscope (JEOL, Freising,  
909 Germany) equipped with a Gatan Orius 1200A camera (Gatan, Munich, Germany).

910 After prescreening the 250 nm semi-thin sections from HPF samples for ribbon synapses, electron  
911 tomography was performed as described previously (Strenzke et al., 2016). First, 10 nm gold beads  
912 (British Bio Cell) were applied to both sides of the post-stained grids functioning as fiducial markers.  
913 With the Serial-EM software (Mastronarde, 2005), single axis tilt series were acquired mainly from -60°  
914 to +60° with 1° increments at 12,000-x magnification and a pixel size of 1.19 nm using a JEM2100 (JEOL)

915 transmission electron microscope at 200 kV. For final tomogram generation, the IMOD software package  
916 etomo was used and tomographic reconstructions were generated using 3dmod (Kremer et al., 1996).

917

#### 918 Patch-clamp

919 Apical turns of the organs of Corti from 2-4 weeks old rats were isolated in ice-cold HEPES Hank's  
920 solution containing (in mM): 5.26 KCl, 141.7 NaCl, 0.5 MgSO<sub>4</sub>·7H<sub>2</sub>O, 10 HEPES, 1 MgCl<sub>2</sub>, 11.1 D-glucose  
921 and 3.42 L-glutamine, pH adjusted to around 7.2, osmolality ~300 mOsm/kg. The recording chamber was  
922 perfused with modified Ringer's solution containing (in mM): 2.8 KCl, 111 NaCl, 35 TEA-Cl, 10 HEPES, 1  
923 CsCl, 1 MgCl<sub>2</sub>, 11.1 D-glucose, 5mM CaCl<sub>2</sub>, pH adjusted to around 7.2 with NaOH and osmolality ~300  
924 mOsm/kg. Cleaning of the tissue was performed to make the inner hair cells accessible for patch clamp  
925 by removing the tectorial membrane and surrounding cells. The clean exposed basolateral surface of  
926 IHCs was patch-clamped using EPC-10 amplifier (HEKA Electronics, Germany) controlled by *Patchmaster*  
927 software at RT, as also described previously (Moser and Beutner, 2000). Pipettes solutions contained (in  
928 mM): 137 Cs-gluconate, 10 TEA-Cl, 10 4- aminopyridine, 10 HEPES, 1 MgCl<sub>2</sub>, and 300µg/ml of  
929 amphotericin B, pH adjusted to 7.2 using HCl and CsOH and osmolality ~290 mOsm/kg.

930 Cells were kept at a holding potential of -87 mV. All voltages were corrected for liquid junction potential  
931 offline (17 mV). Currents were leak corrected using a p/10 protocol. Recordings were discarded when  
932 the leak current exceeded -50 pA, R<sub>s</sub> exceeded 30 MΩ or Ca<sup>2+</sup> current rundown exceeded 25%. Current-  
933 voltage relationships (IVs) were recorded once the access resistance dropped below 30 MΩ, by applying  
934 increasing 10 ms long step-depolarization pulses of voltage ranging from -87 mV to 65 mV, in steps of 5  
935 mV. Exocytosis measurements were performed by measuring increments in membrane capacitance  
936 using the Lindau-Neher technique (Lindau and Neher, 1988). Membrane capacitance changes ( $\Delta C_m$ )  
937 were recorded by stimulating the cells at the potential for maximal Ca<sup>2+</sup> influx (-17 mV) for variable

938 durations. An interval of 10-90 s was given before the successive stimuli were used. Each protocol was  
939 sequentially applied two- three times and only IHCs with reproducible measurements were included. For  
940 analysis, traces were averaged 400 ms before and after the depolarisation (skipping the first 60 ms; or  
941 first 5, 10, 25 ms in the case of dual pulse experiments with inter-pulse intervals of 25, 50, 100 ms  
942 respectively). The traces were subjected to 5 or 10 pass binomial smoothing using Igor Pro 6  
943 (WaveMetrics Inc.) for display.

944

945 [Data analysis and statistics](#)

946 Quantitative analysis of FIB-SEM and tomogram datasets

947 Data were segmented semi-automatically using 3dmod of the IMOD software (Kremer et al., 1996).  
948 IHCs, nuclei, afferent nerve fibers, ribbon synapses, mitochondria, pre- and postsynaptic densities were  
949 assigned as “closed” objects using the *sculpt* drawing tool. For SVs, first the total amount of vesicles  $\leq$   
950 80 nm from the ribbon surface were quantified in number and size using the spherical “scattered”  
951 object at the maximum projection of the vesicle for spherical SVs. Non-spherical SVs were segmented  
952 manually as “closed” objects. The number of SVs was presented as total number per ribbon as well as  
953 normalized to the size of the ribbon area. Further, two distinct morphological vesicle pools were  
954 additionally quantified in size and number (as previously characterized in (Strenzke et al., 2016)): (i)  
955 membrane-proximal synaptic vesicles (MP-SVs,  $\leq$  50 nm distance between SV membrane and AZ  
956 membrane and  $\leq$  100 nm from the presynaptic density); and (ii) ribbon-associated synaptic vesicles (RA-  
957 SVs, first layer of vesicles around the ribbon with a maximum distance of 80 nm from the ribbon surface  
958 to the vesicle membrane and not falling into the MP-SV pool). Using the *imodinfo* function of 3dmod,  
959 information about the ribbon, mitochondria, pre- and postsynaptic density sizes was given as well as the  
960 radii for all vesicle pools were determined with this function in order to calculate the average diameter  
961 per tomogram. Distance measurements were performed with the measurement drawing tool along the



962 x, y and z-axis. Movies were generated with 3dmod, Fiji (Schindelin et al., 2012) and iMovie (Apple Inc.,  
963 version 10.3.1).

964

965

#### 966 Quantitative analysis of confocal and STED images

967 The size of the synaptic ribbon, PSD and Ca<sup>2+</sup> channel clusters (lines and spots) were estimated by fitting  
968 a 2D-Gaussian function to individual structures in 2D-STED or confocal images. This yielded values of full  
969 width of half maximum (FWHM) along the long and short axes. The areas of the structures have been  
970 reported as areas of ellipsoids, calculated as: Area =  $\pi \times (\text{Long Axis}/2) \times (\text{Short Axis}/2)$ . For estimation of  
971 centers of mass of the immunofluorescent spots, the following formula was used:

$$CM_r = \sum_{i=1}^n \frac{m_i r_i}{M}$$

972 Where  $CM_r$  represents the xy coordinates of the center of mass,  $m_i$  is the intensity of individual pixel,  $r_i$  is  
973 the xy coordinate of the pixel and  $M$  is the sum of all intensities.

974 All images were analyzed and z-projected using NIH ImageJ software, and further analysis was  
975 performed using Igor Pro 6 (WaveMetrics Inc.). For analysis of nearest neighbor distance of synaptic  
976 ribbons from immunolabelled confocal sections, we used *Imaris 9.6* (Oxford Instruments).  
977 Immunofluorescent ribbon spots were detected per IHC using the inbuilt spot-detection algorithm in a  
978 region of interest marked within a z-stack. Spot parameters provided for ellipsoid detection were 0.44  
979  $\mu\text{m}$  and 1.13 $\mu\text{m}$  for estimated XY and Z diameters respectively. Thresholding was performed based on  
980 quality of immunofluorescence to eliminate artefactual spots. A manual check was performed to include  
981 undetected spots and to exclude falsely detected spots and spots not localizing within the cell of

982 interest. The nearest neighbor distance was computed as the minimum distance between the centers of  
983 homogenous mass of the detected spots.

984

#### 985 Statistical analysis

986 Data are mainly presented as box plots with the mean values highlighted as a cross and with individual  
987 data points overlaid and were analysed using Excel, Igor Pro 6 and 7 (WaveMetrics Inc.) and R. In order  
988 to characterize the subgroups of *Pclo<sup>gt/gt</sup>* ribbon synapses, acquired with electron tomography, in  
989 addition to our manual grouping, we performed an unsupervised K-means clustering with R by  
990 considering the following variables: ribbon, presynaptic density as well as SV pool counts and sizes. An  
991 optimal number of k=2 clusters was selected based on the decrease of the total within-cluster sum of  
992 squares observed.

993

994 Using Igor Pro, normality of data was assessed with the Jarque-Bera test or the Wald-Wolfowitz runs  
995 test and equality of variances in normally distributed data was assessed with the F-test. Differences  
996 between two groups were evaluated for significant differences using the two-tailed unpaired Student's  
997 t-test, or, when not normally distributed and/or variance was unequal, the unpaired two-tailed Mann-  
998 Whitney Wilcoxon test. For multiple comparisons, the one-way ANOVA with post-hoc Tukey's test or the  
999 Kruskal-Wallis (KW) test with multiple comparison correction (NPMC: Non-parametric multiple  
1000 comparison test) was utilized. For Fig 1B, C, we performed two-way repeated measures ANOVA with  
1001 post-hoc Holm-Šidák correction for multiple comparisons using *GraphPad Prism 9* (GraphPad Software).  
1002 Non-significant differences between samples are indicated as *n.s.*, significant differences are indicated  
1003 as *\*P* < 0.05, *\*\*P* < 0.01, *\*\*\*P* < 0.001, *\*\*\*\*P* < 0.0001.

## 1004 Acknowledgements

1005 We thank S. Gerke, C. Senger-Freitag, A.J. Goldak, S. Langer, S. Thom for expert technical assistance.  
1006 Further, we would like to thank N. Karagulyan for help with analysis scripts.

## 1007 Funding

1008 This work was funded by grants of the Deutsche Forschungsgemeinschaft (DFG) through the  
1009 collaborative research center 889 (projects A02 to TM, A06 to NS, A07 to CW), the Leibniz program (to  
1010 TM), Niedersächsisches Vorab (TM) and EXC 2067/1- 390729940 (MBExC to TM, CW, WM). Part of this  
1011 work (AMS) was funded through the Cluster of Excellence and DFG Research Center Nanoscale  
1012 Microscopy and Molecular Physiology of the Brain. This work was also supported by the Deutsche  
1013 Forschungsgemeinschaft (DFG) (FOR2848, MO 1082/1-2, project 08 to WM). RK was supported by  
1014 funding from the Studienstiftung des Deutschen Volkes. FA, CCG and NS were funded by the Deutsche  
1015 Forschungsgemeinschaft (DFG); SFB958 to CCG, EXC-2049-390688087 for the Center of Excellence  
1016 NeuroCure to FA, Heisenberg program STR 1027/4-1 to NS. In addition, this research was supported by  
1017 Fondation Pour l’Audition (FPA RD-2020-10) to TM.

1018

## 1019 Authors contributions

1020 S.M., R.K., T.M. and C.W. designed the study. S.M. performed electron microscopic work (conventional  
1021 embeddings, HPF/FS, enhanced en bloc stainings, TEM of random sections, electron tomography, FIB-  
1022 SEM data acquisition and post-processing) with contribution from C.W., data analysis and supervised I.F.  
1023 together with C.W. for pre-embedding immunogold labeling data acquisition. R.K. performed  
1024 immunohistochemistry, confocal and STED microscopy, systems physiology, physiological cell data  
1025 acquisition as well as data analysis with contribution from J.N.. A.M.S. performed and W.M. supervised  
1026 FIB-SEM data acquisition and post-processing. J.N. supervised electrophysiology. F.A., F.K.H and C.C.G  
1027 provided unpublished material and contributed to pilot experiment. N.S. supervised systems physiology  
1028 data acquisition and analysis. M.G. contributed to statistical analysis. S.M., R.K., T.M. and C.W. prepared  
1029 the manuscript with contributions from all other authors.

1030

## 1031 Conflict of interest

1032

1033 The authors declare no conflict of interest.

1034

## 1035 References

- 1036 **Ackermann, F., Schink, K. O., Bruns, C., Izsvák, Z., Hamra, F. K., Rosenmund, C. and Garner, C. C.** (2019).  
1037 Critical role for Piccolo in synaptic vesicle retrieval. *eLife* **8**, e46629.
- 1038 **Altrock, W. D., tom Dieck, S., Sokolov, M., Meyer, A. C., Sigler, A., Brakebusch, C., Fässler, R., Richter,**  
1039 **K., Boeckers, T. M., Potschka, H., et al.** (2003). Functional Inactivation of a Fraction of Excitatory  
1040 Synapses in Mice Deficient for the Active Zone Protein Bassoon. *Neuron* **37**, 787–800.

- 1041 **Becker, L., Schnee, M. E., Niwa, M., Sun, W., Maxeiner, S., Talaei, S., Kachar, B., Rutherford, M. A. and**  
1042 **Ricci, A. J.** (2018). The presynaptic ribbon maintains vesicle populations at the hair cell afferent  
1043 fiber synapse. *eLife* **7**, e30241.
- 1044 **Buran, B. N., Strenzke, N., Neef, A., Gundelfinger, E. D., Moser, T. and Liberman, M. C.** (2010). Onset  
1045 coding is degraded in auditory nerve fibers from mutant mice lacking synaptic ribbons. *J.*  
1046 *Neurosci. Off. J. Soc. Neurosci.* **30**, 7587–7597.
- 1047 **Butola, T., Wichmann, C. and Moser, T.** (2017). Piccolo Promotes Vesicle Replenishment at a Fast  
1048 Central Auditory Synapse. *Front. Synaptic Neurosci.* **9**, 14.
- 1049 **Cases-Langhoff, C., Voss, B., Garner, A. M., Appeltauer, U., Takei, K., Kindler, S., Veh, R. W., De Camilli,**  
1050 **P., Gundelfinger, E. D. and Garner, C. C.** (1996). Piccolo, a novel 420 kDa protein associated with  
1051 the presynaptic cytomatrix. *Eur. J. Cell Biol.* **69**, 214–223.
- 1052 **Chakrabarti, R. and Wichmann, C.** (2019). Nanomachinery Organizing Release at Neuronal and Ribbon  
1053 Synapses. *Int. J. Mol. Sci.* **20**, 2147.
- 1054 **Chakrabarti, R., Michanski, S. and Wichmann, C.** (2018). Vesicle sub-pool organization at inner hair cell  
1055 ribbon synapses. *EMBO Rep.* e44937.
- 1056 **Chapochnikov, N. M., Takago, H., Huang, C.-H., Pangršič, T., Khimich, D., Neef, J., Auge, E., Göttfert, F.,**  
1057 **Hell, S. W., Wichmann, C., et al.** (2014). Uniquantal Release through a Dynamic Fusion Pore Is a  
1058 Candidate Mechanism of Hair Cell Exocytosis. *Neuron* **17**, 1389–1403.
- 1059 **Deerinck, T. J., Shone, T. M., Bushong, E. A., Ramachandra, R., Peltier, S. T. and Ellisman, M. H.** (2018).  
1060 High-performance serial block-face SEM of nonconductive biological samples enabled by focal  
1061 gas injection-based charge compensation. *J. Microsc.* **270**, 142–149.
- 1062 **Dick, O., Hack, I., Altmann, W. D., Garner, C. C., Gundelfinger, E. D. and Brandstätter, J. H.** (2001).  
1063 Localization of the presynaptic cytomatrix protein Piccolo at ribbon and conventional synapses  
1064 in the rat retina: Comparison with Bassoon. *J. Comp. Neurol.* **439**, 224–234.
- 1065 **Dick, O., tom Dieck, S., Altmann, W. D., Ammermüller, J., Weiler, R., Garner, C. C., Gundelfinger, E. D.**  
1066 **and Brandstätter, J. H.** (2003). The Presynaptic Active Zone Protein Bassoon Is Essential for  
1067 Photoreceptor Ribbon Synapse Formation in the Retina. *Neuron* **37**, 775–786.
- 1068 **Fenster, S. D., Kessels, M. M., Qualmann, B., Chung, W. J., Nash, J., Gundelfinger, E. D. and Garner, C.**  
1069 **C.** (2003). Interactions between Piccolo and the Actin/Dynamamin-binding Protein Abp1 Link  
1070 Vesicle Endocytosis to Presynaptic Active Zones. *J. Biol. Chem.* **278**, 20268–20277.
- 1071 **Frank, T., Khimich, D., Neef, A. and Moser, T.** (2009). Mechanisms contributing to synaptic Ca<sup>2+</sup> signals  
1072 and their heterogeneity in hair cells. *Proc. Natl. Acad. Sci.* **106**, 4483–4488.
- 1073 **Frank, T., Rutherford, M. A., Strenzke, N., Neef, A., Pangršič, T., Khimich, D., Fejtova, A., Gundelfinger,**  
1074 **E. D., Liberman, M. C., Harke, B., et al.** (2010). Bassoon and the synaptic ribbon organize Ca<sup>2+</sup>  
1075 channels and vesicles to add release sites and promote refilling. *Neuron* **68**, 724–738.

- 1076 **Goutman, J. D. and Glowatzki, E.** (2007). Time course and calcium dependence of transmitter release at  
1077 a single ribbon synapse. *Proc. Natl. Acad. Sci.* **104**, 16341–16346.
- 1078 **Grabner, C. P. and Moser, T.** (2021). The mammalian rod synaptic ribbon is essential for Cav channel  
1079 facilitation and ultrafast synaptic vesicle fusion. *eLife* **10**, e63844.
- 1080 **Grabner, C. P., Gandini, M. A., Rehak, R., Le, Y., Zamponi, G. W. and Schmitz, F.** (2015). RIM1/2-  
1081 Mediated Facilitation of Cav1.4 Channel Opening Is Required for Ca<sup>2+</sup>-Stimulated Release in  
1082 Mouse Rod Photoreceptors. *J. Neurosci.* **35**, 13133–13147.
- 1083 **Gundelfinger, E. D., Reissner, C. and Garner, C. C.** (2015). Role of Bassoon and Piccolo in Assembly and  
1084 Molecular Organization of the Active Zone. *Front. Synaptic Neurosci.* **7**, 19.
- 1085 **Hua, Y., Ding, X., Wang, H., Wang, F., Lu, Y., Neef, J., Gao, Y., Moser, T. and Wu, H.** (2021). Electron  
1086 Microscopic Reconstruction of Neural Circuitry in the Cochlea. *Cell Rep.* **34**,.
- 1087 **Hull, C., Studholme, K., Yazulla, S. and von Gersdorff, H.** (2006). Diurnal changes in exocytosis and the  
1088 number of synaptic ribbons at active zones of an ON-type bipolar cell terminal. *J. Neurophysiol.*  
1089 **96**, 2025–2033.
- 1090 **Jean, P., Morena, D. L. de la, Michanski, S., Tobón, L. M. J., Chakrabarti, R., Picher, M. M., Neef, J.,  
1091 Jung, S., Gültas, M., Maxeiner, S., et al.** (2018). The synaptic ribbon is critical for sound  
1092 encoding at high rates and with temporal precision. *eLife* **7**, e29275.
- 1093 **Jean, P., Anttonen, T., Michanski, S., Diego, A. M. G. de, Steyer, A. M., Neef, A., Oestreicher, D., Kroll,  
1094 J., Nardis, C., Pangršič, T., et al.** (2020). Macromolecular and electrical coupling between inner  
1095 hair cells in the rodent cochlea. *Nat. Commun.* **11**, 1–14.
- 1096 **Jing, Z., Rutherford, M. A., Takago, H., Frank, T., Fejtova, A., Khimich, D., Moser, T. and Strenzke, N.**  
1097 (2013). Disruption of the presynaptic cytomatrix protein bassoon degrades ribbon anchorage,  
1098 multiquantal release, and sound encoding at the hair cell afferent synapse. *J. Neurosci.* **33**,  
1099 4456–4467.
- 1100 **Jung, S., Oshima-Takago, T., Chakrabarti, R., Wong, A. B., Jing, Z., Yamanbaeva, G., Picher, M. M.,  
1101 Wojcik, S. M., Göttfert, F., Predoehl, F., et al.** (2015a). Rab3-interacting molecules 2 $\alpha$  and 2 $\beta$   
1102 promote the abundance of voltage-gated CaV1.3 Ca<sup>2+</sup> channels at hair cell active zones. *Proc.*  
1103 *Natl. Acad. Sci.* **112**, E3141–E3149.
- 1104 **Jung, S., Maritzen, T., Wichmann, C., Jing, Z., Neef, A., Revelo, N. H., Al-Moyed, H., Meese, S., Wojcik,  
1105 S. M., Panou, I., et al.** (2015b). Disruption of adaptor protein 2 $\mu$  (AP-2 $\mu$ ) in cochlear hair cells  
1106 impairs vesicle reloading of synaptic release sites and hearing. *EMBO J.* **34**, 2686–2702.
- 1107 **Kantardzhieva, A. V., Liberman, M. C. and Sewell, W. F.** (2013). Quantitative analysis of ribbons,  
1108 vesicles, and cisterns at the cat inner hair cell synapse: correlations with spontaneous rate. *J.*  
1109 *Comp. Neurol.* **521**, 3260–3271.
- 1110 **Khimich, D., Nouvian, R., Pujol, R., tom Dieck, S., Egner, A., Gundelfinger, E. D. and Moser, T.** (2005).  
1111 Hair cell synaptic ribbons are essential for synchronous auditory signalling. *Nature* **434**, 889–  
1112 894.

- 1113 **Kiang, N. Y., Pfeiffer, R. R., Warr, W. B. and Backus, A. S.** (1965). Stimulus coding in the cochlear  
1114 nucleus. *Trans. Am. Otol. Soc.* **53**, 35–58.
- 1115 **Kremer, J. R., Mastronarde, D. N. and McIntosh, J. R.** (1996). Computer visualization of three-  
1116 dimensional image data using IMOD. *J. Struct. Biol.* **116**, 71–76.
- 1117 **Krinner, S., Butola, T., Jung, S., Wichmann, C. and Moser, T.** (2017). RIM-Binding Protein 2 Promotes a  
1118 Large Number of CaV1.3 Ca<sup>2+</sup>-Channels and Contributes to Fast Synaptic Vesicle Replenishment  
1119 at Hair Cell Active Zones. *Front. Cell. Neurosci.* **11**, 334.
- 1120 **Kroll, J., Jaime Tobón, L. M., Vogl, C., Neef, J., Kondratiuk, I., König, M., Strenzke, N., Wichmann, C.,**  
1121 **Milosevic, I. and Moser, T.** (2019). Endophilin-A regulates presynaptic Ca<sup>2+</sup> influx and synaptic  
1122 vesicle recycling in auditory hair cells. *EMBO J.* **38**,.
- 1123 **Leal-Ortiz, S., Waites, C. L., Terry-Lorenzo, R., Zamorano, P., Gundelfinger, E. D. and Garner, C. C.**  
1124 (2008). Piccolo modulation of Synapsin1a dynamics regulates synaptic vesicle exocytosis. *J. Cell*  
1125 *Biol.* **181**, 831–846.
- 1126 **Li, C., Li, X., Bi, Z., Sugino, K., Wang, G., Zhu, T. and Liu, Z.** (2020). Comprehensive transcriptome  
1127 analysis of cochlear spiral ganglion neurons at multiple ages. *eLife* **9**,.
- 1128 **Li, P., Lin, Z., An, Y., Lin, J., Zhang, A., Wang, S., Tu, H., Ran, J., Wang, J., Liang, Y., et al.** (2021). Piccolo  
1129 is essential for the maintenance of mouse retina but not cochlear hair cell function. *Aging* **13**,  
1130 11678–11695.
- 1131 **Lieberman, M. C.** (1978). Auditory-nerve response from cats raised in a low-noise chamber. *J. Acoust.*  
1132 *Soc. Am.* **63**, 442–455.
- 1133 **Lieberman, M. C.** (1980). Morphological differences among radial afferent fibers in the cat cochlea: an  
1134 electron-microscopic study of serial sections. *Hear. Res.* **3**, 45–63.
- 1135 **Lieberman, M. C., Dodds, L. W. and Pierce, S.** (1990). Afferent and efferent innervation of the cat  
1136 cochlea: quantitative analysis with light and electron microscopy. *J. Comp. Neurol.* **301**, 443–  
1137 460.
- 1138 **Lieberman, L. D., Wang, H. and Liberman, M. C.** (2011). Opposing Gradients of Ribbon Size and AMPA  
1139 Receptor Expression Underlie Sensitivity Differences among Cochlear-Nerve/Hair-Cell Synapses.  
1140 *J. Neurosci.* **31**, 801–808.
- 1141 **Limbach, C., Laue, M. M., Wang, X., Hu, B., Thiede, N., Hultqvist, G. and Kilimann, M. W.** (2011).  
1142 Molecular in situ topology of Aczonin/Piccolo and associated proteins at the mammalian  
1143 neurotransmitter release site. *Proc. Natl. Acad. Sci.* **108**, E392–E401.
- 1144 **Lindau, M. and Neher, E.** (1988). Patch-clamp techniques for time-resolved capacitance measurements  
1145 in single cells. *Pflüg. Arch. Eur. J. Physiol.* **411**, 137–146.
- 1146 **Mastronarde, D. N.** (2005). Automated electron microscope tomography using robust prediction of  
1147 specimen movements. *J. Struct. Biol.* **152**, 36–51.

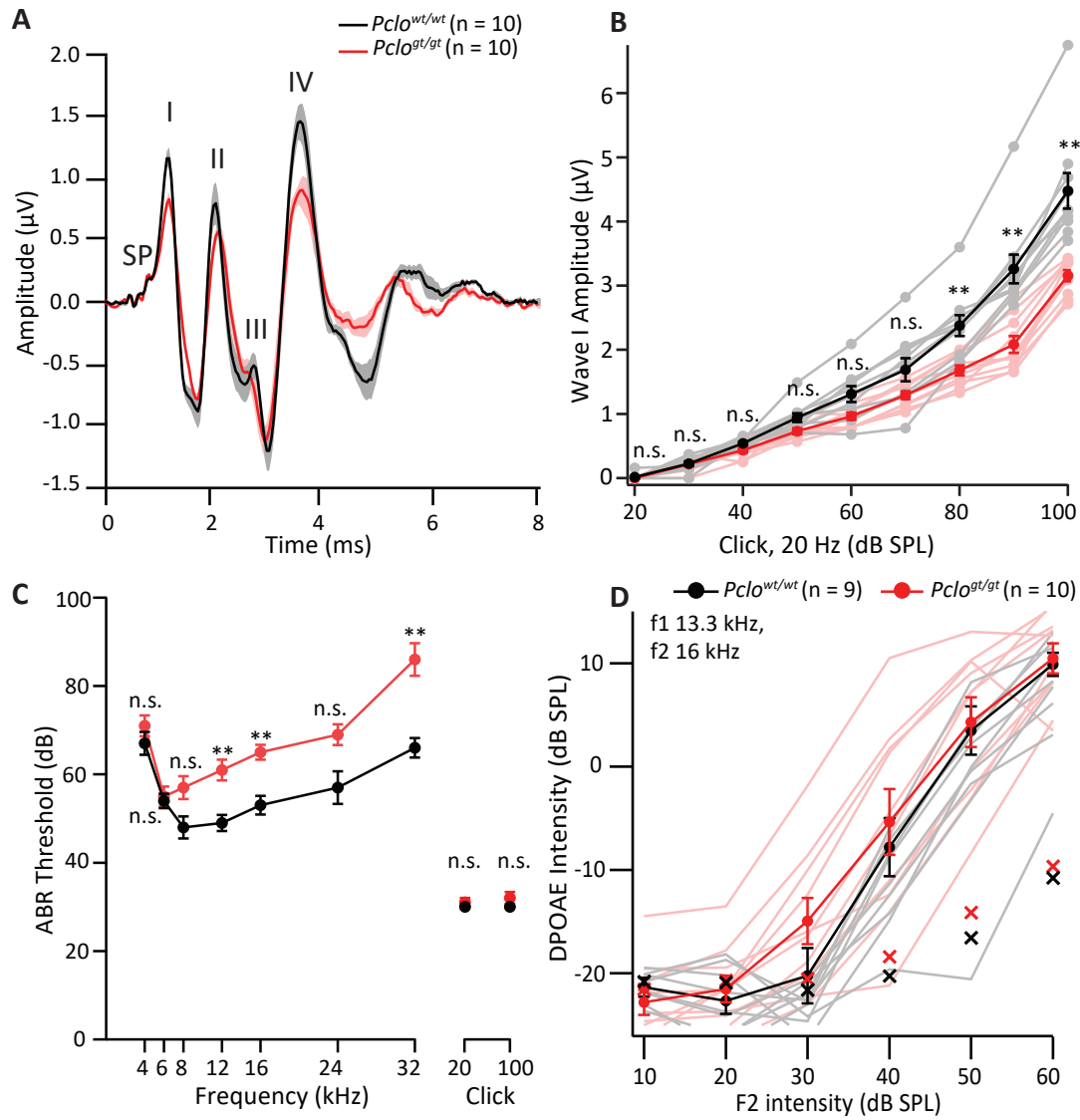
- 1148 **Matthews, G. and Fuchs, P.** (2010). The diverse roles of ribbon synapses in sensory neurotransmission.  
1149 *Nat. Rev. Neurosci.* **11**, 812–822.
- 1150 **Maxeiner, S., Luo, F., Tan, A., Schmitz, F. and Südhof, T. C.** (2016). How to make a synaptic ribbon:  
1151 RIBEYE deletion abolishes ribbons in retinal synapses and disrupts neurotransmitter release.  
1152 *EMBO J.* **35**, 1098–1114.
- 1153 **Medrano, G. A., Singh, M., Plautz, E. J., Good, L. B., Chapman, K. M., Chaudhary, J., Jaichander, P.,  
1154 Powell, H. M., Pudasaini, A., Shelton, J. M., et al.** (2020). Mutant screen for reproduction  
1155 unveils depression-associated Piccolo's control over reproductive behavior. 405985.
- 1156 **Meyer, A. C., Frank, T., Khimich, D., Hoch, G., Riedel, D., Chapochnikov, N. M., Yarin, Y. M., Harke, B.,  
1157 Hell, S. W., Egner, A., et al.** (2009). Tuning of synapse number, structure and function in the  
1158 cochlea. *Nat. Neurosci.* **12**, 444–453.
- 1159 **Michanski, S., Smaluch, K., Steyer, A. M., Chakrabarti, R., Setz, C., Oestreicher, D., Fischer, C., Möbius,  
1160 W., Moser, T., Vogl, C., et al.** (2019). Mapping developmental maturation of inner hair cell  
1161 ribbon synapses in the apical mouse cochlea. *Proc. Natl. Acad. Sci.* **116**, 6415–6424.
- 1162 **Moser, T. and Beutner, D.** (2000). Kinetics of exocytosis and endocytosis at the cochlear inner hair cell  
1163 afferent synapse of the mouse. *Proc. Natl. Acad. Sci.* **97**, 883–888.
- 1164 **Moser, T., Grabner, C. P. and Schmitz, F.** (2019). Sensory processing at ribbon synapses in the retina and  
1165 the cochlea. *Physiol. Rev.* **100**, 103–144.
- 1166 **Mukherjee, K., Yang, X., Gerber, S. H., Kwon, H.-B., Ho, A., Castillo, P. E., Liu, X. and Südhof, T. C.**  
1167 (2010). Piccolo and bassoon maintain synaptic vesicle clustering without directly participating in  
1168 vesicle exocytosis. *Proc. Natl. Acad. Sci. U. S. A.* **107**, 6504–6509.
- 1169 **Müller, T. M., Gierke, K., Joachimsthaler, A., Sticht, H., Izsvák, Z., Hamra, F. K., Fejtová, A., Ackermann,  
1170 F., Garner, C. C., Kremers, J., et al.** (2019). A multiple Piccolino-RIBEYE interaction supports  
1171 plate-shaped synaptic ribbons in retinal neurons. *J. Neurosci.* **39**, 2038–18.
- 1172 **Neef, J., Urban, N. T., Ohn, T.-L., Frank, T., Jean, P., Hell, S. W., Willig, K. I. and Moser, T.** (2018).  
1173 Quantitative optical nanophysiology of Ca<sup>2+</sup> signaling at inner hair cell active zones. *Nat.*  
1174 *Commun.* **9**, 290.
- 1175 **Ohn, T.-L., Rutherford, M. A., Jing, Z., Jung, S., Duque-Afonso, C. J., Hoch, G., Picher, M. M., Scharinger,  
1176 A., Strenzke, N. and Moser, T.** (2016). Hair cells use active zones with different voltage  
1177 dependence of Ca<sup>2+</sup> influx to decompose sounds into complementary neural codes. *Proc. Natl.*  
1178 *Acad. Sci.* **113**, E4716–E4725.
- 1179 **Özçete, Ö. D. and Moser, T.** (2021). A sensory cell diversifies its output by varying Ca<sup>2+</sup> influx-release  
1180 coupling among active zones. *EMBO J.* **40**, e106010.
- 1181 **Pangrsic, T., Singer, J. H. and Koschak, A.** (2018). Voltage-Gated Calcium Channels: Key Players in  
1182 Sensory Coding in the Retina and the Inner Ear. *Physiol. Rev.* **98**, 2063–2096.

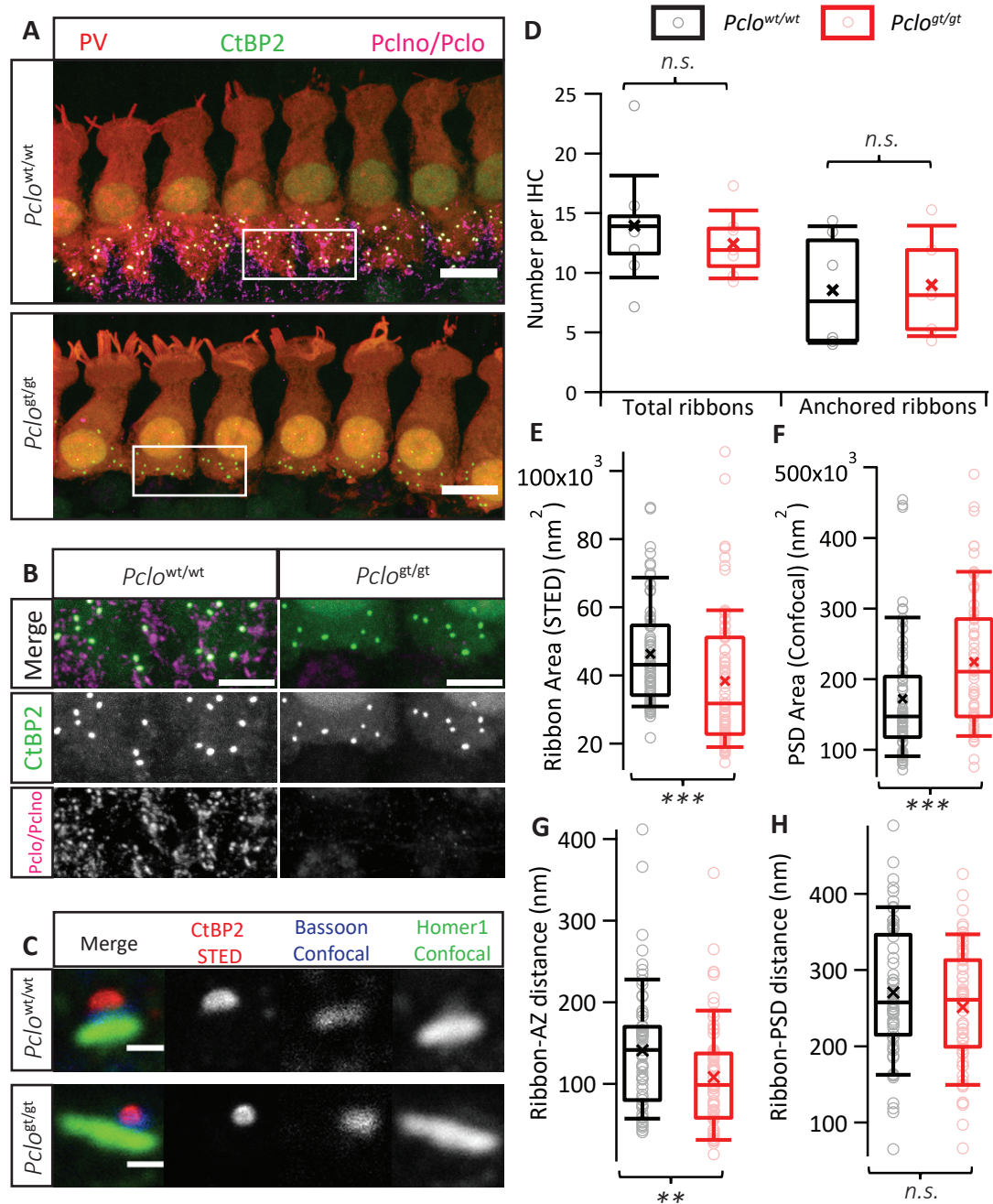
- 1183 **Parthier, D., Kuner, T. and Körber, C.** (2018). The presynaptic scaffolding protein Piccolo organizes the  
1184 readily releasable pool at the calyx of Held. *J. Physiol.* **596**, 1485–1499.
- 1185 **Payne, S. A., Joens, M. S., Chung, H., Skigen, N., Frank, A., Gattani, S., Vaughn, K., Schwed, A., Nester,**  
1186 **M., Bhattacharyya, A., et al.** (2021). Maturation of Heterogeneity in Afferent Synapse  
1187 Ultrastructure in the Mouse Cochlea. *Front. Synaptic Neurosci.* **0**,
- 1188 **Petitpré, C., Wu, H., Sharma, A., Tokarska, A., Fontanet, P., Wang, Y., Helmbacher, F., Yackle, K.,**  
1189 **Silberberg, G., Hadjab, S., et al.** (2018). Neuronal heterogeneity and stereotyped connectivity in  
1190 the auditory afferent system. *Nat. Commun.* **9**, 3691.
- 1191 **Regus-Leidig, H., Ott, C., Löhner, M., Atorf, J., Fuchs, M., Sedmak, T., Kremers, J., Fejtová, A.,**  
1192 **Gundelfinger, E. D. and Brandstätter, J. H.** (2013). Identification and Immunocytochemical  
1193 Characterization of Piccolino, a Novel Piccolo Splice Variant Selectively Expressed at Sensory  
1194 Ribbon Synapses of the Eye and Ear. *PLoS ONE* **8**, e70373.
- 1195 **Regus-Leidig, H., Fuchs, M., Löhner, M., Leist, S. R., Leal-Ortiz, S., Chiodo, V. A., Hauswirth, W. W.,**  
1196 **Garner, C. C. and Brandstätter, J. H.** (2014). In vivo knockdown of Piccolino disrupts presynaptic  
1197 ribbon morphology in mouse photoreceptor synapses. *Front. Cell. Neurosci.* **8**, 259.
- 1198 **Reynolds, E. S.** (1963). THE USE OF LEAD CITRATE AT HIGH pH AS AN ELECTRON-OPAQUE STAIN IN  
1199 ELECTRON MICROSCOPY. *J. Cell Biol.* **17**, 208–212.
- 1200 **Ruel, J., Nouvian, R., D’Aldin, C. G., Pujol, R., Eybalin, M. and Puel, J.-L.** (2001). Dopamine inhibition of  
1201 auditory nerve activity in the adult mammalian cochlea. *Eur. J. Neurosci.* **14**, 977–986.
- 1202 **Rutherford, M. A. and Moser, T.** (2016). The Ribbon Synapse Between Type I Spiral Ganglion Neurons  
1203 and Inner Hair Cells. In *The Primary Auditory Neurons of the Mammalian Cochlea* (ed. Dabdoub,  
1204 A.), Fritzsche, B.), Popper, A. N.), and Fay, R. R.), pp. 117–156. New York, NY: Springer New York.
- 1205 **Sachs, M. B. and Abbas, P. J.** (1974). Rate versus level functions for auditory-nerve fibers in cats: tone-  
1206 burst stimuli. *J. Acoust. Soc. Am.* **56**, 1835–1847.
- 1207 **Schindelin, J., Arganda-Carreras, I., Frise, E., Kaynig, V., Longair, M., Pietzsch, T., Preibisch, S., Rueden,**  
1208 **C., Saalfeld, S., Schmid, B., et al.** (2012). Fiji: an open-source platform for biological-image  
1209 analysis. *Nat. Methods* **9**, 676–682.
- 1210 **Schmitz, F., Königstorfer, A. and Südhof, T. C.** (2000). RIBEYE, a component of synaptic ribbons: a  
1211 protein’s journey through evolution provides insight into synaptic ribbon function. *Neuron* **28**,  
1212 857–872.
- 1213 **Sherrill, H. E., Jean, P., Driver, E. C., Sanders, T. R., Fitzgerald, T. S., Moser, T. and Kelley, M. W.** (2019).  
1214 Pou4f1 Defines a Subgroup of Type I Spiral Ganglion Neurons and Is Necessary for Normal Inner  
1215 Hair Cell Presynaptic Ca<sup>2+</sup> Signaling. *J. Neurosci.* **39**, 5284–5298.
- 1216 **Shrestha, B. R., Chia, C., Wu, L., Kujawa, S. G., Liberman, M. C. and Goodrich, L. V.** (2018). Sensory  
1217 Neuron Diversity in the Inner Ear Is Shaped by Activity. *Cell* **174**, 1229-1246.e17.

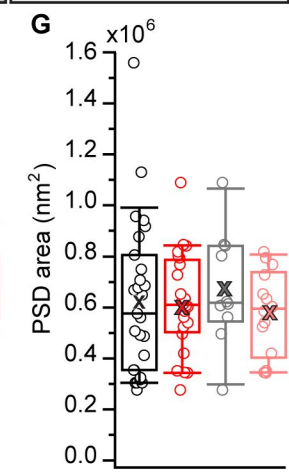
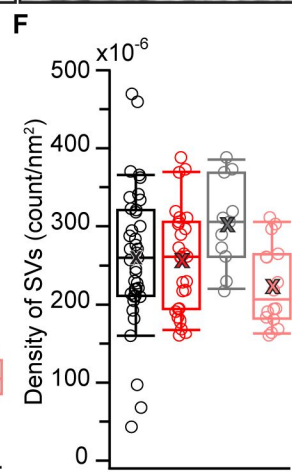
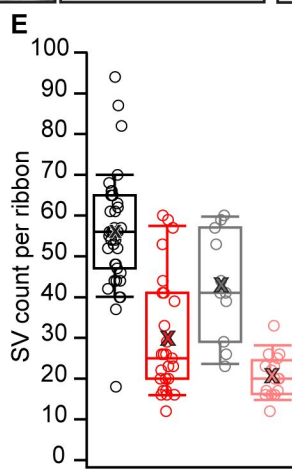
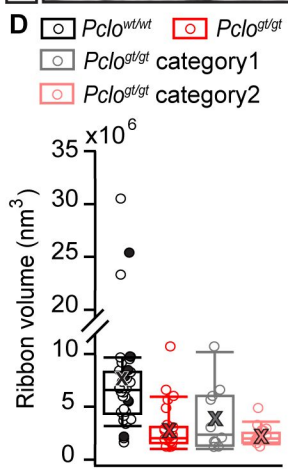
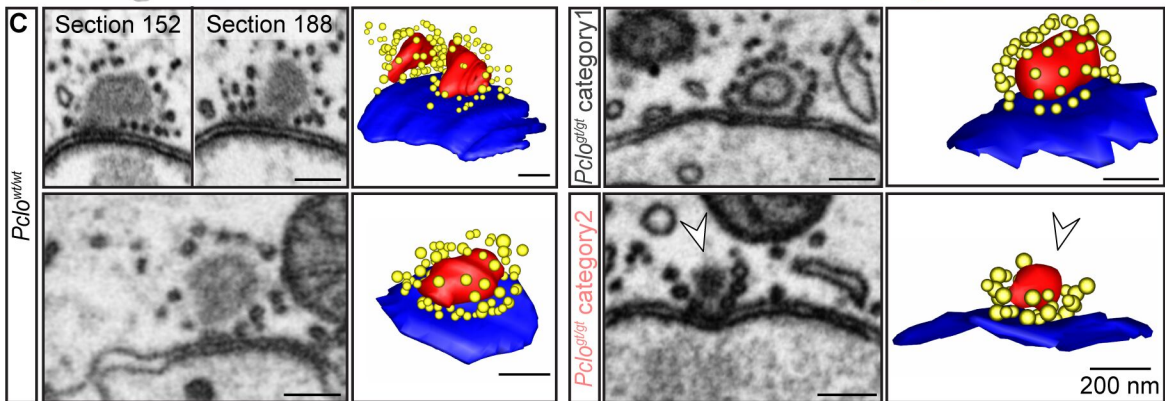
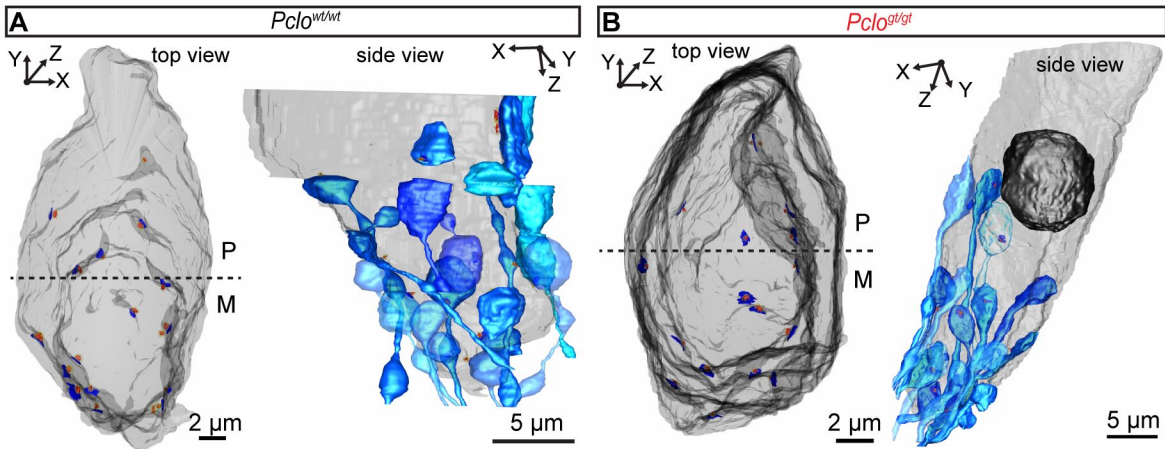


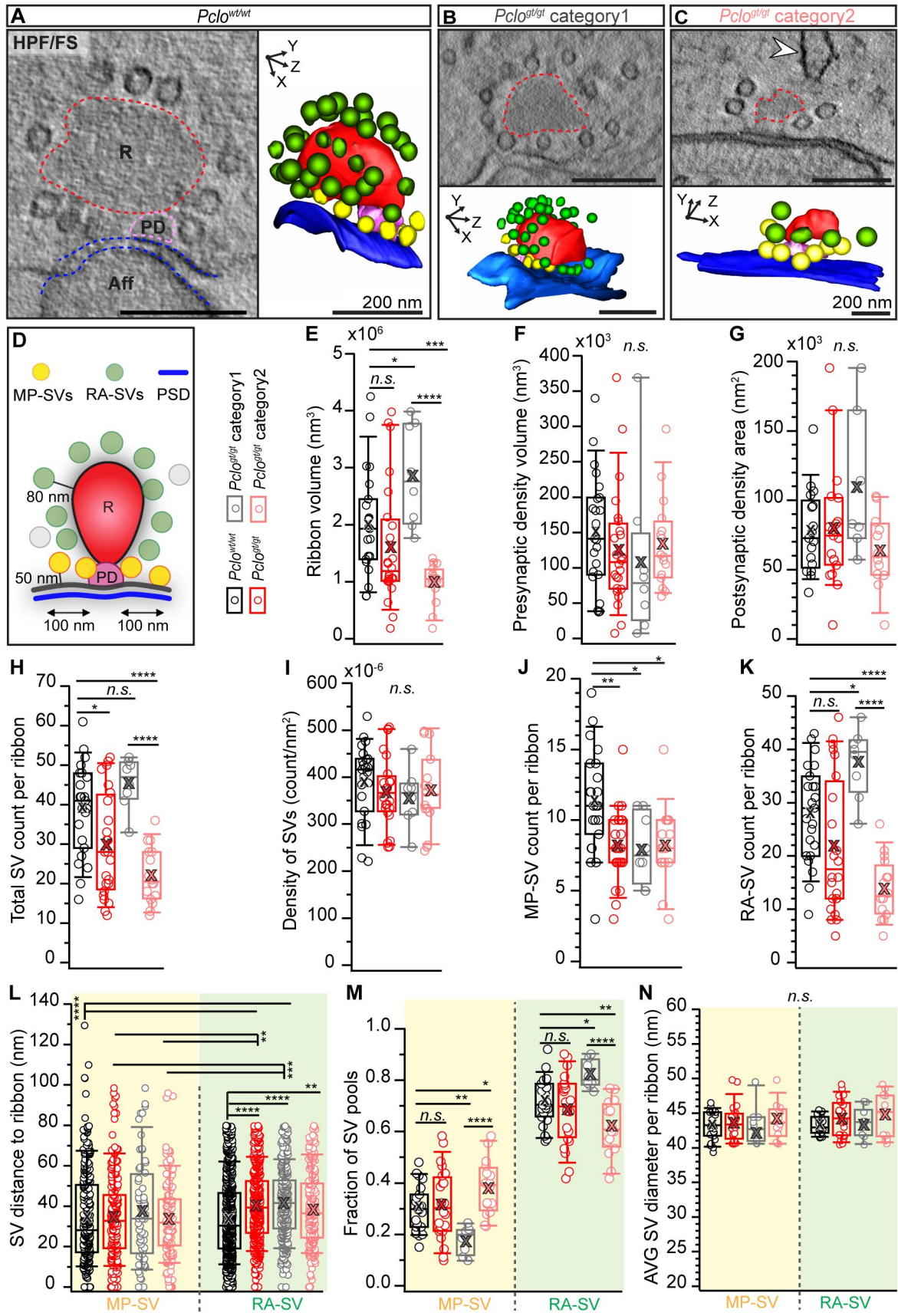
- 1218 **Snellman, J., Mehta, B., Babai, N., Bartoletti, T. M., Akmentin, W., Francis, A., Matthews, G., Thoreson,**  
1219 **W. and Zenisek, D.** (2011). Acute destruction of the synaptic ribbon reveals a role for the ribbon  
1220 in vesicle priming. *Nat. Neurosci.* **14**, 1135–1141.
- 1221 **Sobkowicz, H. M., Rose, J. E., Scott, G. E. and Slapnick, S. M.** (1982). Ribbon synapses in the developing  
1222 intact and cultured organ of Corti in the mouse. *J. Neurosci.* **2**, 942–957.
- 1223 **Sobkowicz, H. M., Rose, J. E., Scott, G. L. and Levenick, C. V.** (1986). Distribution of synaptic ribbons in  
1224 the developing organ of Corti. *J. Neurocytol.* **15**, 693–714.
- 1225 **Stamatakis, S., Francis, H. W., Lehar, M., May, B. J. and Ryugo, D. K.** (2006). Synaptic alterations at inner  
1226 hair cells precede spiral ganglion cell loss in aging C57BL/6J mice. *Hear. Res.* **221**, 104–118.
- 1227 **Strenzke, N., Chakrabarti, R., Al-Moyed, H., Müller, A., Hoch, G., Pangrsic, T., Yamanbaeva, G., Lenz, C.,**  
1228 **Pan, K.-T., Auge, E., et al.** (2016). Hair cell synaptic dysfunction, auditory fatigue and thermal  
1229 sensitivity in otoferlin Ile515Thr mutants. *EMBO J.* **35**, e201694564.
- 1230 **Sun, S., Babola, T., Pregernig, G., So, K. S., Nguyen, M., Su, S.-S. M., Palermo, A. T., Bergles, D. E.,**  
1231 **Burns, J. C. and Müller, U.** (2018). Hair Cell Mechanotransduction Regulates Spontaneous  
1232 Activity and Spiral Ganglion Subtype Specification in the Auditory System. *Cell* **174**, 1247-  
1233 1263.e15.
- 1234 **Taberner, A. M. and Liberman, M. C.** (2005). Response Properties of Single Auditory Nerve Fibers in the  
1235 Mouse. *J. Neurophysiol.* **93**, 557–569.
- 1236 **tom Dieck, S., Sanmartí-Vila, L., Langnaese, K., Richter, K., Kindler, S., Soyke, A., Wex, H., Smalla, K. H.,**  
1237 **Kämpf, U., Fränzer, J. T., et al.** (1998). Bassoon, a novel zinc-finger CAG/glutamine-repeat  
1238 protein selectively localized at the active zone of presynaptic nerve terminals. *J. Cell Biol.* **142**,  
1239 499–509.
- 1240 **Waites, C. L., Leal-Ortiz, S. A., Okerlund, N., Dalke, H., Fejtova, A., Altroch, W. D., Gundelfinger, E. D.**  
1241 **and Garner, C. C.** (2013). Bassoon and Piccolo maintain synapse integrity by regulating protein  
1242 ubiquitination and degradation. *EMBO J.* **32**, 954–969.
- 1243 **Wichmann, C. and Moser, T.** (2015). Relating structure and function of inner hair cell ribbon synapses.  
1244 *Cell Tissue Res.* **361**, 95-114.
- 1245 **Winter, I. M., Robertson, D. and Yates, G. K.** (1990). Diversity of characteristic frequency rate-intensity  
1246 functions in guinea pig auditory nerve fibres. *Hear. Res.* **45**, 191–202.
- 1247 **Wong, A. B., Rutherford, M. A., Gabrielaitis, M., Pangršič, T., Göttfert, F., Frank, T., Michanski, S., Hell,**  
1248 **S., Wolf, F., Wichmann, C., et al.** (2014). Developmental refinement of hair cell synapses  
1249 tightens the coupling of Ca<sup>2+</sup> influx to exocytosis. *EMBO J.* **33**, 247–264.
- 1250 **Yin, Y., Liberman, L. D., Maison, S. F. and Liberman, M. C.** (2014). Olivocochlear innervation maintains  
1251 the normal modiolar-pillar and habenular-cuticular gradients in cochlear synaptic morphology. *J.*  
1252 *Assoc. Res. Otolaryngol. JARO* **15**, 571–583.

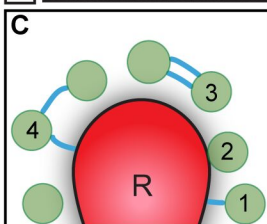
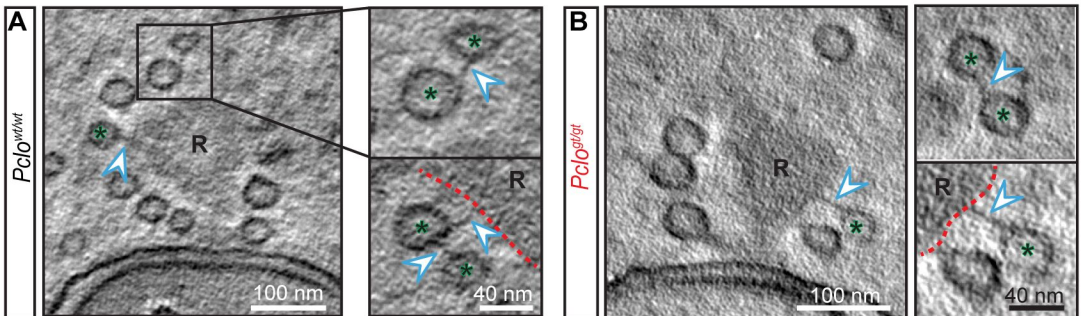
1253



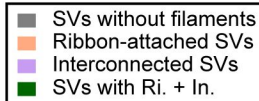
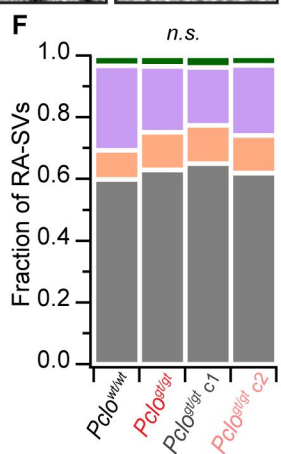
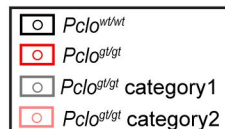
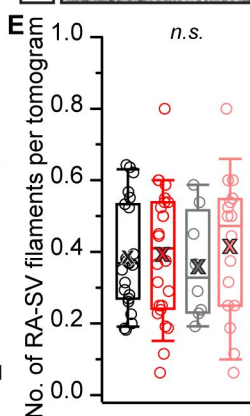
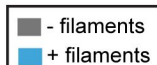
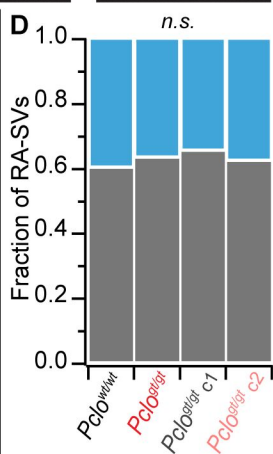


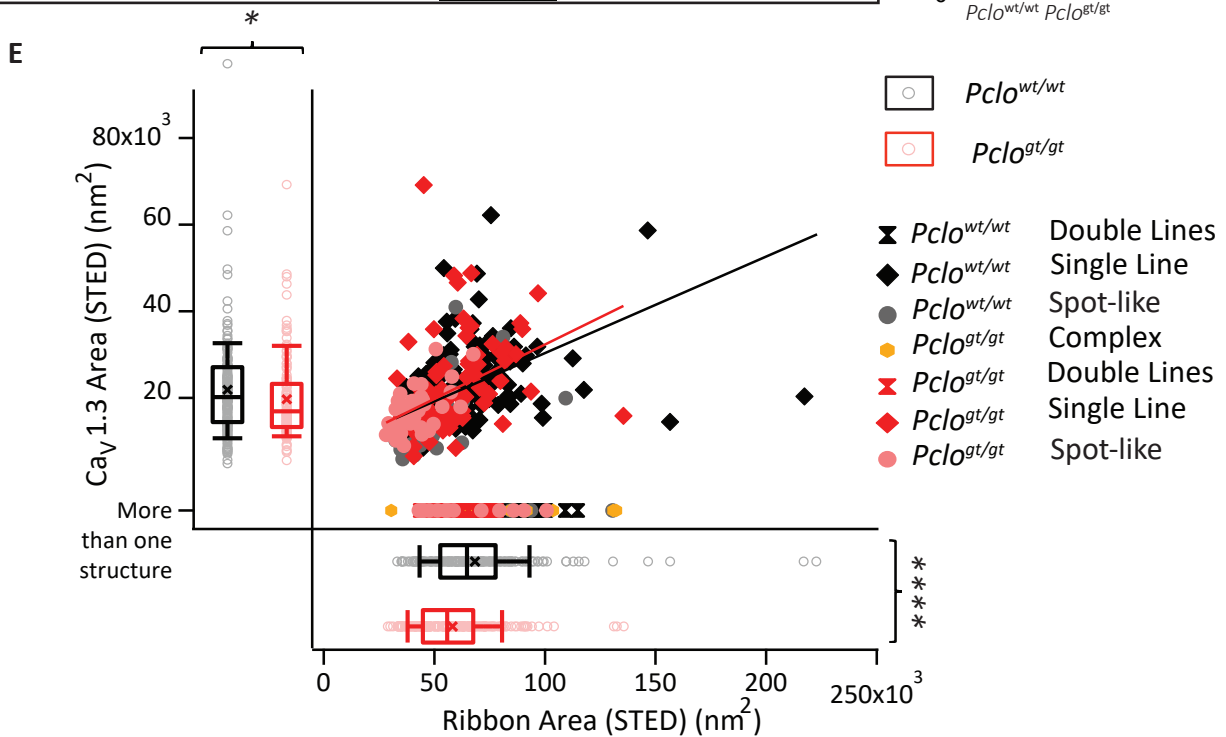
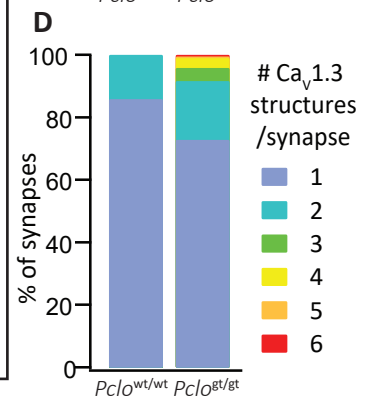
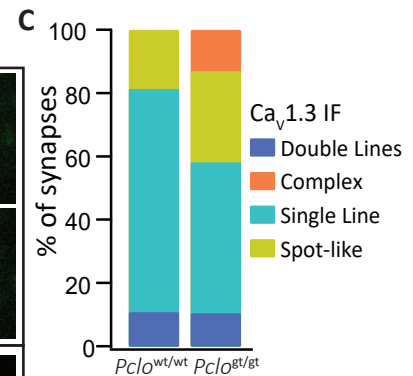
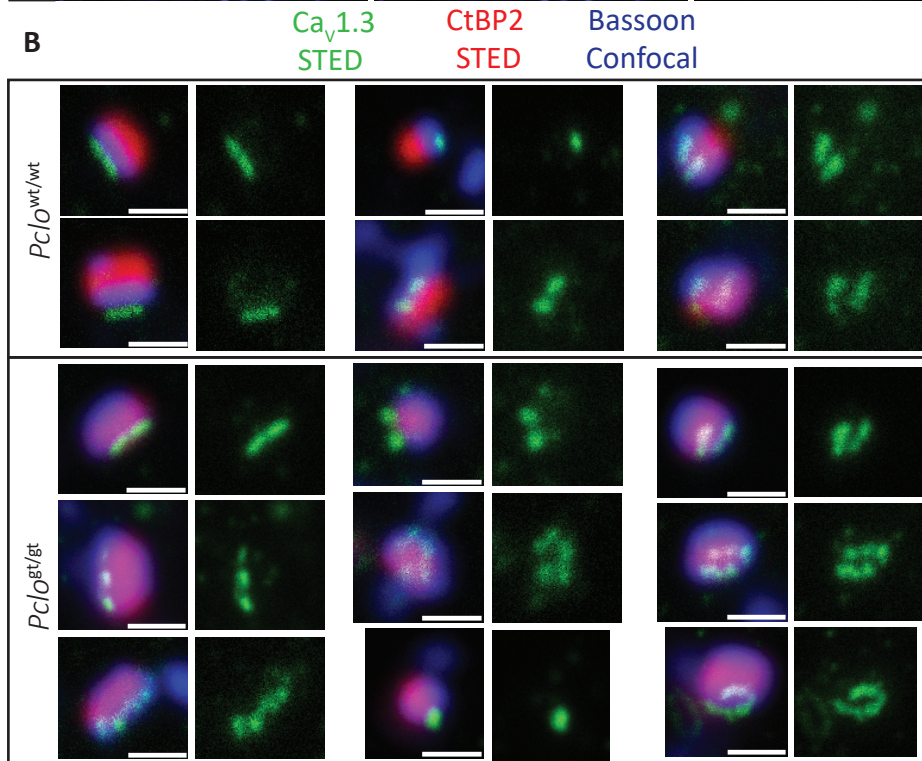
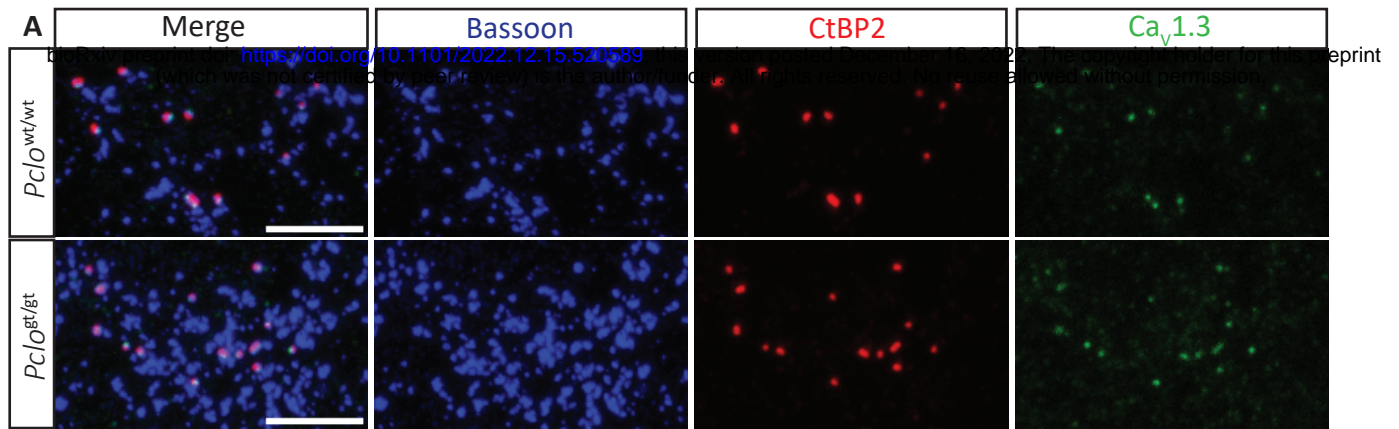


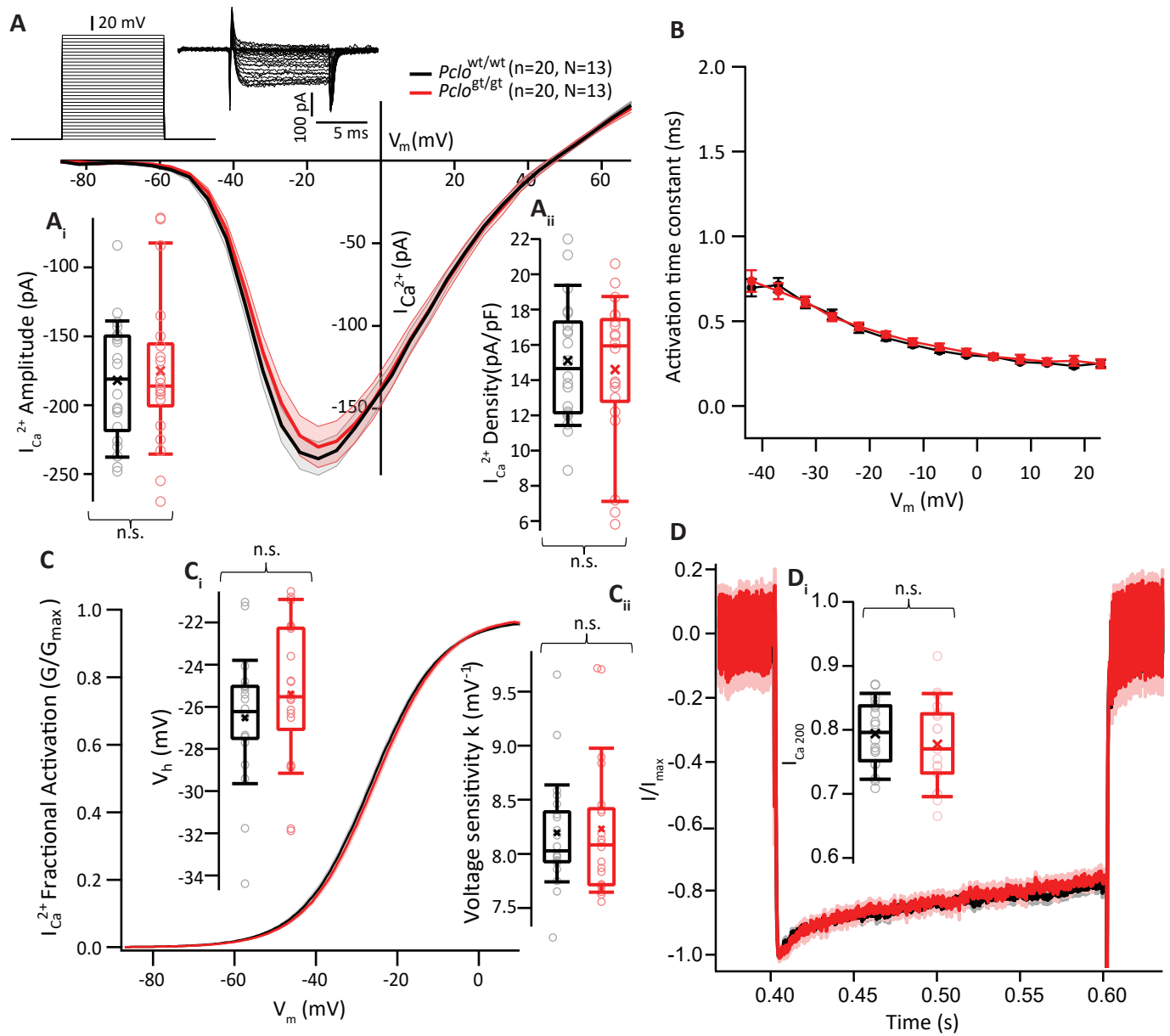




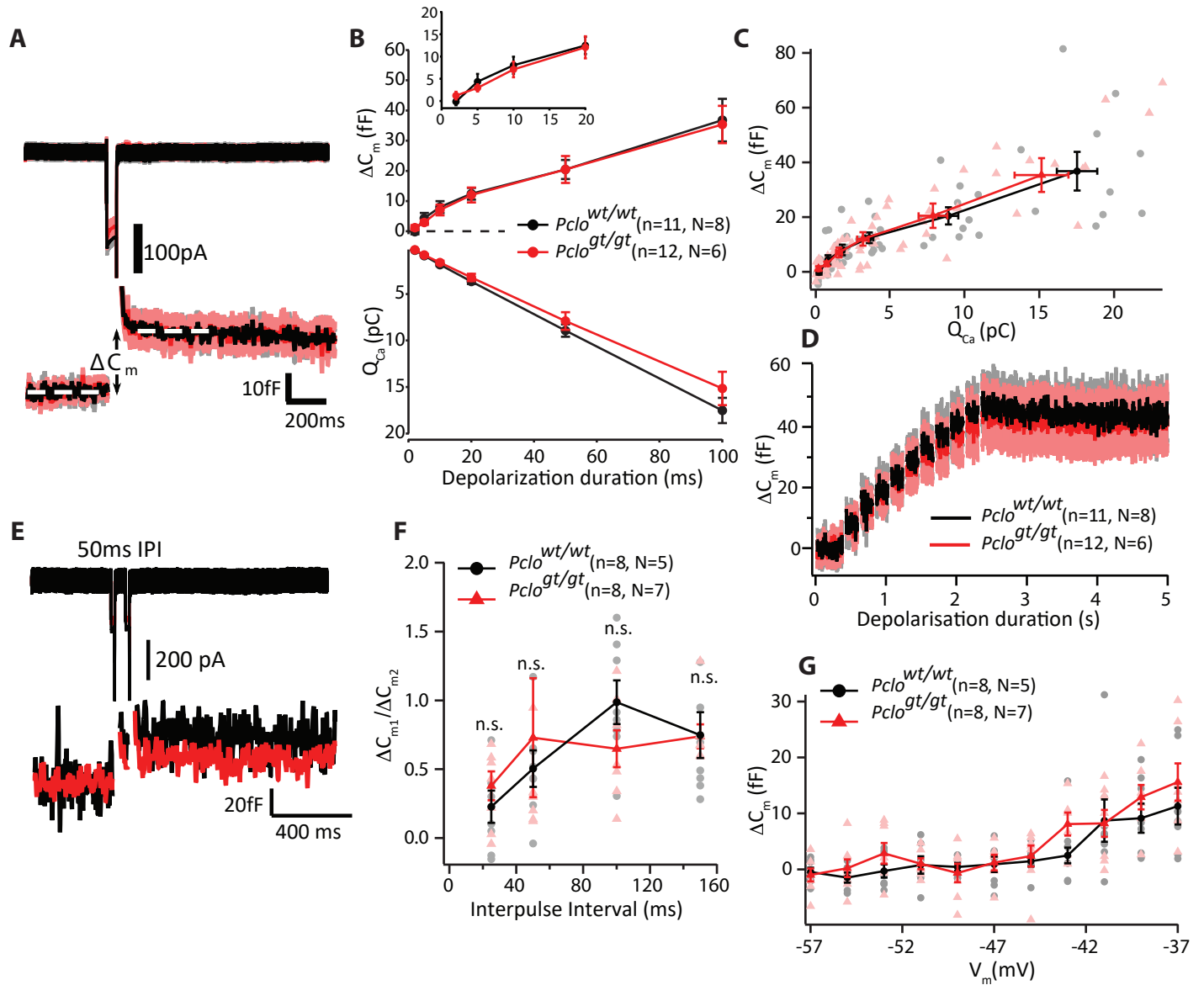
- 1 Ribbon-attached SV
- 2 SV without filament
- 3 Interconnected SVs
- 4 Ribbon-attached (Ri.) + Interconnected (In.) SV











**(A)****(B)****(C)****(D)**

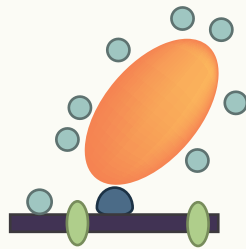
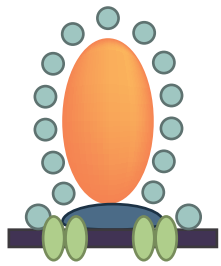
Wild-type

Bassoon mutants

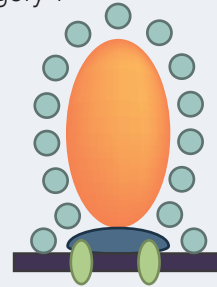
Piccolino mutants

RIBEYE KO

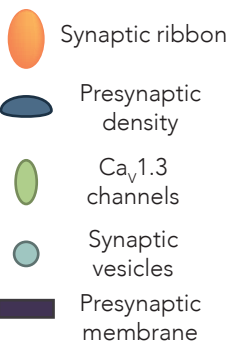
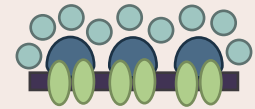
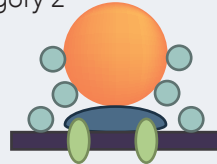
bioRxiv preprint doi: <https://doi.org/10.1101/2022.05.05.490589>; this version posted October 16, 2022. The copyright holder for this preprint (which was not certified by peer review) is the author/funder. All rights reserved. No reuse allowed without permission.



Category 1



Category 2



1. Massive reduction in wave I amplitude, ABR thresholds elevated for clicks and tone bursts
2. Whole-cell  $\text{Ca}^{2+}$  currents reduced due to less channel numbers. Slow activation and slightly enhanced inactivation in  $\Delta\text{Ex4/5}$  mutant
3. Reduced fast and sustained exocytosis, slow vesicle replenishment

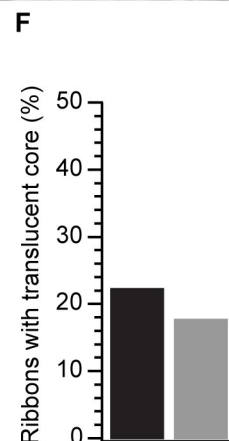
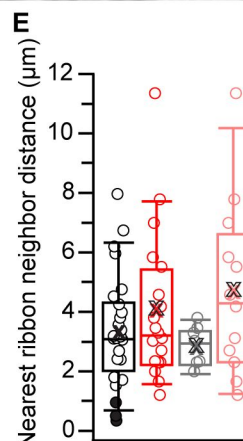
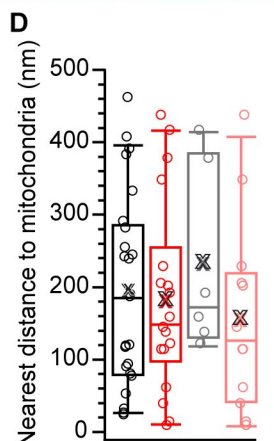
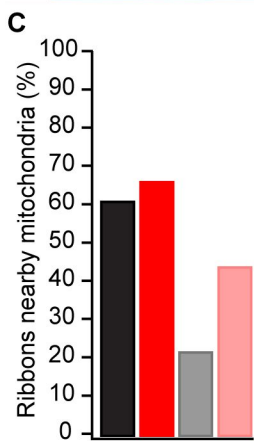
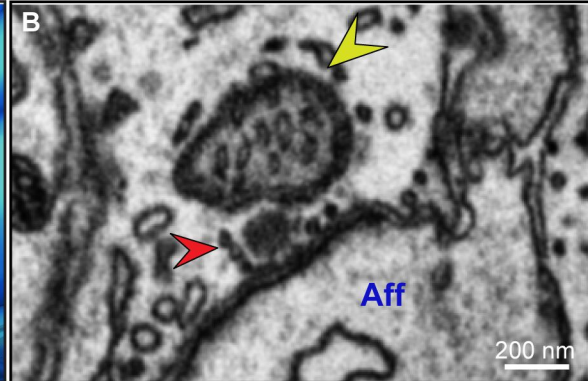
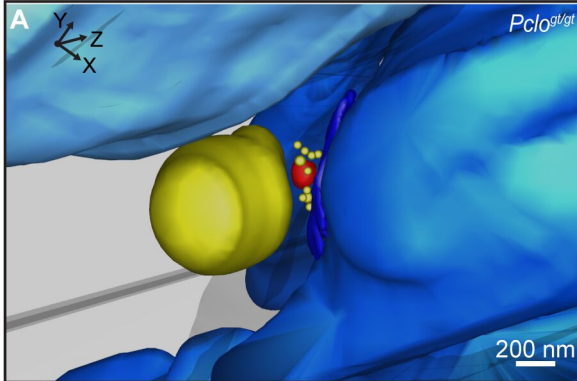
(Khimich et al., Nature 2005;  
Frank et al., Neuron 2010;  
Jing et al., JNeurosci 2013)

1. Wave I amplitude reduced, ABR thresholds elevated for middle and high frequency tone bursts (statistically significant)
2. No change in whole-cell  $\text{Ca}^{2+}$  current amplitude and kinetics
3. Normal exocytosis and replenishment of SVs

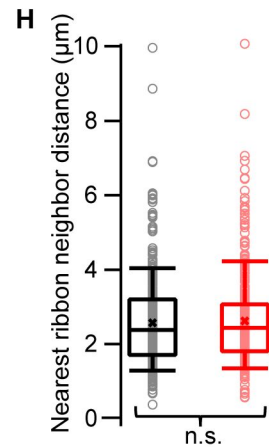
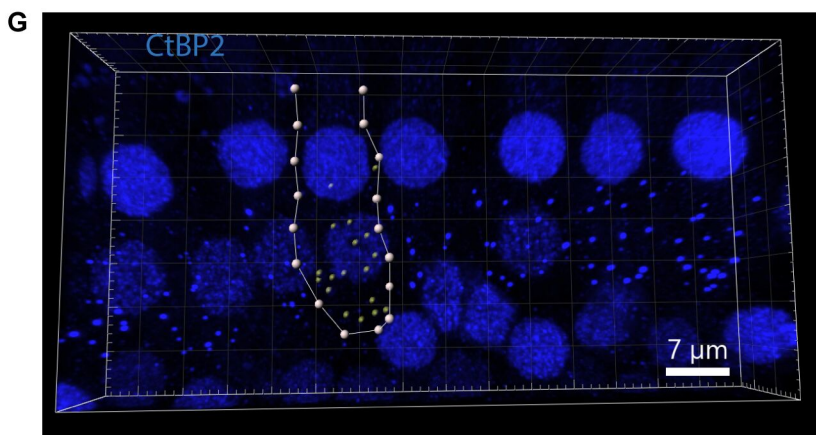
(This Study)

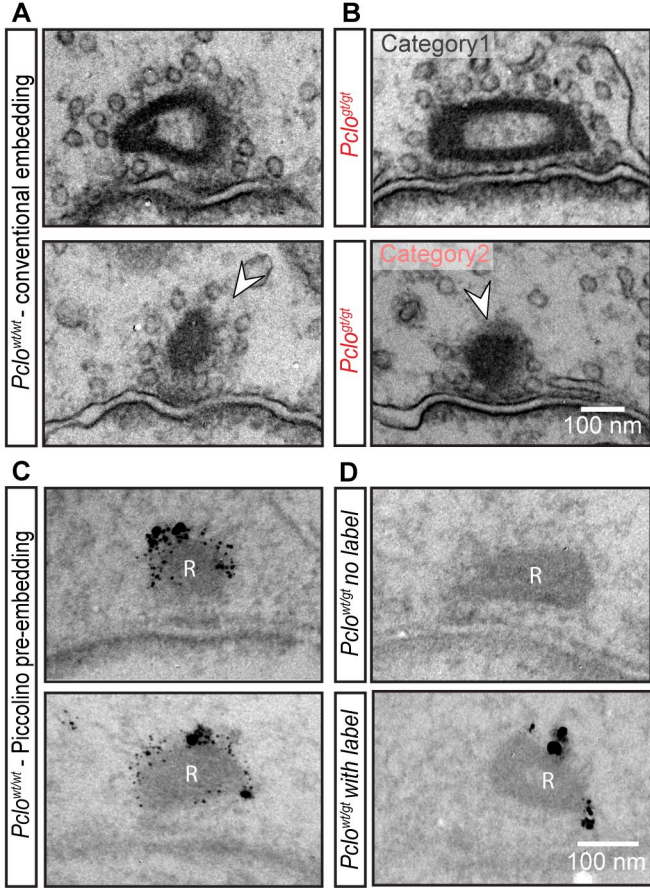
1. Wave I amplitude reduced, ABR thresholds mildly elevated (not significant)
2. No change in  $\text{Ca}^{2+}$  current amplitude at whole-cell or single AZ level.  $\text{Ca}^{2+}$  channels activate at mildly depolarized potentials; slightly enhanced inactivation
3. Normal exocytosis for strong depolarizations, slightly reduced for weak ones, normal SV replenishment

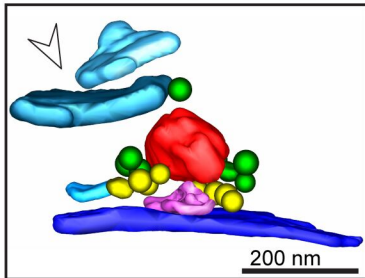
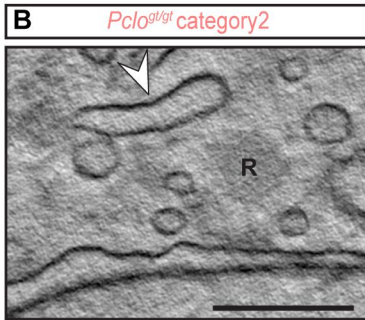
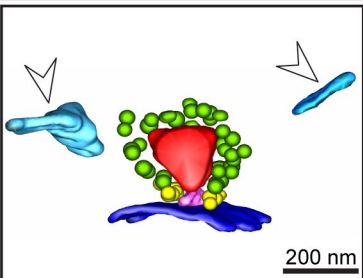
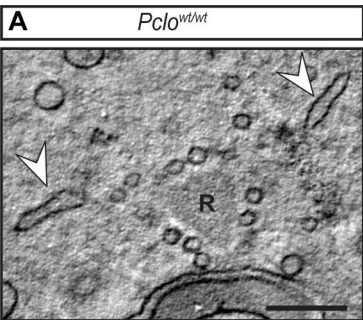
(Jean et al., eLife 2018;  
Becker et al. eLife 2018)



○ *Pclo<sup>wt/wt</sup>*    □ *Pclo<sup>gt/gt</sup>*    ○ *Pclo<sup>gt/gt</sup> category 1*    □ *Pclo<sup>gt/gt</sup> category 2*







**C**

-  *Pclo<sup>wt/wt</sup>*: 47.82 %
-  *Pclo<sup>gt/gt</sup>*: 62.5 %
-  *Pclo<sup>gt/gt</sup> category1*: 62.5 %
-  *Pclo<sup>gt/gt</sup> category2*: 62.5 %

